ENGINEERING BIOCERAMIC MICROSTRUCTURE FOR CUSTOMIZED DRUG DELIVERY

by

Hernando José Pacheco Gómez

A dissertation submitted to the faculty of
The University of North Carolina at Charlotte
in partial fulfillment of the requirements
for the degree of Doctor of Philosophy in
Mechanical Engineering

Charlotte

2013

Approved by:

Dr. Ahmed El-Ghannam

Dr. Irina Nesmelova

Dr. Qiuming Wei

Dr. Didier Dreau

ABSTRACT

HERNANDO JOSÉ PACHECO GÓMEZ. Engineering bioceramic microstructure for customized drug delivery. (Under the direction of DR. AHMED EL-GHANNAM)

One of the most efficient approaches to treat cancer and infection is to use biomaterials as a drug delivery system (DDS). The goal is for the material to provide a sustained release of therapeutic drug dose locally to target the ill tissue without affecting other organs. Silica Calcium Phosphate nano composite (SCPC) is a drug delivery platform that successfully demonstrated the ability to bind and release several therapeutics including antibiotics, anticancer drugs, and growth factors. The aim of the present work is to analyze the role of SCPC microstructure on drug binding and release kinetics. The main crystalline phases of SCPC are α-cristobalite (SiO_2, Cris) and β-rhenanite ($NaCaPO_4$, Rhe); therefore, these two phases were prepared and characterized separately. Structural and compositional features of Cris, Rhe and SCPC bioceramics demonstrated a significant influence on the loading capacity and the release kinetics profile of Vancomycin (Vanc) and Cisplatin (Cis). Fourier Transform Infrared (FTIR) spectroscopy analyses demonstrated the high affinity between the P-O functional groups, in Rhe and SCPC, and the (C=O and N-H) of Vanc and (N-H and O-H) of Cis. By contrast, a weak chemical interaction between the Si-O functional group in Cris and SCPC and the two drugs was observed. Vanc loading per unit surface area increased in the order 8.00 μg Vanc/m^2 for Rhe > 4.49 μg Vanc /m^2 for SCPC>3.01 μg Vanc /m^2 for Cris ($p<0.05$). Cis loading capacity increased in the order 8.59 μg Vanc /m^2 for Cris, 17.8 μg Vanc/m^2 for Rhe and 6.03 μg Vanc /m^2 for SCPC ($p<0.05$). The drug release kinetics was dependent on the carrier as well as on the kind of drug. Different burst

release and sustained release rates were measured for Vanc and Cis from the same carrier. The percentages of the amount of drug amount released from Cris, Rhe and SCPC during the burst stage (the first 2h) were: 50%, 50%, and 46% of Vanc; and 53.4%, 36.6%, and 30.6 % of Cis, respectively. Burst release correlated with the pore size distribution and surface area. Furthermore, the average rates of sustained release in the period 8-216h from Cris, Rhe and SCPC were: 9.8, 7.2 and 3.5 μg/h of Vanc and 4.5, 5.3 and 3.5 μg/h of Cis, respectively. Nearly inert Cris ceramic showed release kinetics controlled by its hierarchical nanoporous structure. On the other hand, the phase composition and surface chemistry of bioactive Rhe or SCPC ceramics overruled the effect of surface area. The relatively low rate of drug release from SCPC was due to the dissolution-back precipitation reaction taking place on the material surface as confirmed by FTIR bands of surface hydroxyapatite layer at 576.5, 596.7 and 620.7 cm^{-1}. Moreover, the solid solution of crystalline phases of SCPC enhanced the bioactivity of the composite. Nuclear Magnetic Resonance (NMR) and cell culture analyses demonstrated that the interactions between the SCPC dissolution products and the released drug did not cause measurable negative effects on the bioactivity of the tested drugs.

The therapeutic effects of the SCPC-Cis hybrid were evaluated using a rat model of hepatocellular carcinoma (HCC). Animals were treated by either systemic cisplatin injection (sCis), or with SCPC-Cis hybrid placed adjacent (ADJ) to, or within (IT), the tumor. Five days after implantation 50-55% of the total cisplatin loaded was released from the SCPC-Cis hybrids resulting in an approximately 50% decrease in tumor volume compared to sCis treatment. Severe side effects were observed in animals treated with

sCis including rapid weight loss and decreased liver and kidney function; such effects were not observed in SCPC-Cis treated animals. Analysis of cisplatin distribution demonstrated drug concentrations in the tumor were 21 and 1.5-times higher in IT and ADJ groups, respectively, as compared to sCis treated animals. These data demonstrate the SCPC drug delivery system can provide an effective localized treatment for HCC with significantly reduced toxicity compared to systemic drug administration. Moreover, it is possible to tailor drug release kinetics from SCPC hybrids by controlling the crystalline structure of the material and the ratios of Cris and Rhe in the composite.

DEDICATION

I dedicate my dissertation to my parents, Hernando and Ana, for their guidance and endless support in all my endeavors. I also lovingly dedicate this thesis to my wife, Melina, who have never left my side and supported me each step of the way.

ACKNOWLEDGEMENTS

I acknowledge with deepest gratitude and sincere thanks to my advisor, Dr. Ahmed El-Ghannam, for his excellent mentorship, patience, and guidance. He introduced me to the field of biomaterials, and helps me to transform into an independent researcher. Dr. El-Ghannam's knowledge, wisdom, and unsurpassed commitment to the highest quality scientific work have immensely inspired and motivated me. I would also like to thank Dr. Irina Nesmelova, Dr. Didier Dréau, and Dr. Qiuming Wei for being a part of my advisory committee and for their valuable inputs in the preparation of this dissertation. I special deeply thanks to Dr. Irina Nesmelova, Dr. Didier Dréau, Dr Ian Marriott, and Dr. Iain Mckillop for their significant collaboration in the execution of various crucial experiments. I would also like to thank Dr. Iain Mckillop for allowing me to us his lab facilities to undertake molecular biology assays. I would also like to thank MSc. Jacob Swet for his patience and training on the cell experiments. Special thanks to the staff of the Mechanical Engineering department, whose help and support have been indispensable. I would like to thank UNC Charlotte for the financial support offered by the Graduate Assistant Support Plan (GASP) award. Finally, I would like to thank my family and friends for their unending support and encouragement throughout my career.

This work was supported in part by a grant from the NC Biotechnology Center, (grant # 540065).

TABLE OF CONTENTS

LIST OF TABLES

LIST OF FIGURES

CHAPTER 1: DRUG DELIVERY SYSTEMS

1.1. Overview

Daily, many laboratories worldwide develop new potent pharmaceutics to combat complicated diseases like infections, inflammations and cancer. However, acute side effects associated with the administration of such drugs, and/or degradation of some of the drug physical and chemical properties (stability or solubility) when in contact with physiological tissues, make their use unsuitable in clinical applications. To provide better medical treatments not only the medicine but also the administration method can be critical. In this sense, delivery systems have received great interest as an alternative for more successful treatments. Ideally, a drug delivery system should be able to provide effective controlled doses of therapeutics during enough time to treat diseases without modifications in the biological activity of the drug molecule [1]. In addition, the therapeutic effects of the drug delivery systems should be associated with minimal acute and chronic side effects when compared to traditional systemic administrations.

The science and technology of controlled release of active agents from delivery systems has more than 50 years of development. These studies have allowed remarkable advances, evolving from macroscopic devices with constant drug release rates to nanoparticles with targeted or site controlled delivery of various therapeutics [2, 3]. Nevertheless, the ideal drug delivery system is far to be achieved. Many problems that

are not evident in the lab came out when the new technology is applied in a real clinical situation [4-8].

A better understanding of the physiological processes related to the interactions of drugs and drug delivery systems is required. Several parameters such as the quantification of the physical and chemical properties of the host material, its interaction with the therapeutic agent, the biology of drug metabolism, and distribution of the drug agent in tissues deserves a deeper understanding. Therefore, the research in drug delivery systems is a complicated task that requires the contribution of people from diverse scientific disciplines. Engineers are more related with the development of new materials and the creation of mathematical models to predict the fate of the eluted drug in the drug delivery systems. There is no doubt that the convergence of different areas of the biomedical sciences and engineering has significantly improved the development of new DDS. Besides, new biomaterials have been the fuel for the innovations in the DDS field, including polymers [9-13], glasses [14-18], ceramics [19-23], and composites [15, 24-29].

Different strategies have been used for the design of drug delivery methods. One of them engages the use of biomaterials able to release therapeutic doses of drug for extended durations [30-34]. This release approach helps when drugs are rapidly metabolized and eliminated from the body after its administration. Diffusion controlled matrix or reservoir systems, and biodegradable carriers can be classified into this group. Another approach involves external or internal energy sources to stimulate the release of drug from the delivery system when needed. Among the various energy sources that have been tested as stimulatory trigger with promising results in vitro: magnetic field [35-38],

redox responsive [39-42], pH [43-45], temperature [46, 47], and others [48-52]. A third strategy implies the conduction of therapeutics inside the body to the precise location where is needed using targeting systems. The targeting DDS can be either passive or active. Passive targeting (PT) occurs when the carrier is transported to the ill tissue by convection or passive diffusion [53]. Particle size, hydrophobic nature, and electrical charge of the carrier, and tissue properties of the disease pathology are very important for PT [54]. Active targeting consists in the attachment of targeting ligands at the surface of the carrier for binding specific receptors at the target site [55].

DDSs are already a commercially available alternative to help in the treatment of diseases from cancer to fungal infections. In the USA, various materials have been already approved by the US Food and Drug Administration (FDA) since 1990; including liposomes, PEG, PLGA and proteins [56, 57]. Together to the pharmaceutical impact, the research and development of new and advanced drug delivery systems has a strong economic force, with a global market of $132 billion in 2010 and a projected growing rate of 5% during the next decade [58]. In addition, the reformulation of therapeutics in control release packages can extent the patent life and reduce the normal costs and time involved in the development of a new drug, in about 10-fold and 3-fold respectively [59]. Biomaterials are natural candidates to serve as drug delivery systems because of their biocompatibility. Biomaterials are thought to have the ability to perform with living tissue or living systems without producing a toxic, injurious, or immunological response. Two main groups of biomaterials can be highlighted for their applications for DDS: Biopolymers and Bioceramics.

1.1.1. Biopolymers

Biopolymers are relatively easy to process and can offer tunable biocompatibility and biodegradability [112, 113]. The size of the carrier has a significant and varied effect in the mechanism of action of the drug delivery. For that reason, a sub-classification based on the carrier size has been proposed in this work: nano and molecular size; and micro and macro size polymeric carriers.

1.1.1.1. Injectable Molecular and Nano Size Biopolymers DDS

These delivery systems are designed to improve the physical properties that influence drug distribution (solubility and stability) by altering the chemical structure of the drug molecules. This group includes block copolymers, antibodies, synthetic polymers, and natural polymers.

Amphiphilic molecules, such as phospholipids and block copolymers, have become very attractive for researchers because of their chemical flexibility [3]. They can be assembled as micelles, lipid bilayers, and liposomes. The versatility to form stable nanoparticles colloidal ensures prolonged circulation in the bloodstream and adequate drug release kinetics upon accumulation at the delivery site. This feature is appealing to passive targeting via the enhanced permeation and retention effect [60]. Polymer-drug conjugates have become a fast-growing field, with nearly a dozen polymeric conjugates advancing to the clinical trial stage [61]. Among the polymers that have capture the attention of researchers for drug conjugation are: Polyethylene glycol (PEG) [62-65], N-(2-hydroxypropil) methacrylamide copolymer (HPMA) [66-68], Dextran [69-71], polylysine [72-74], poly(divinyl ether-co-maleic anhydride)[75, 76], and other polysaccharides [77-79]. The polymer-drug conjugates are commonly formed by the

polymer, a linker, the therapeutic agent, and sometimes by cell-specific targeting agents [61]. PEG is a particularly attractive polymer for conjugation. PEGylation is a popular technique design to increase drugs solubility and stability, and retard its elimination from the body [80]. Conjugates of PEG with proteins to treat different diseases including genetic abnormalities [81], cancer [82, 83], hepatitis C [80, 84], and HIV/AIDS [85, 86] are either in clinical trials or already in the market. Moreover, PEGylation used for steric stabilization of colloidal liposomes particles reduces the uptake of the particles by liver and spleen macrophages and extends the particles circulation times in the blood [87-89]. This facilitates the accumulation of particles at target site [53].

One active area that has captivated a significant number of research works is the use of conjugates for cancer therapies. Conjugates of HPMA coupled with doxorubicin are already in Phase I/II of clinical trials [90]. In vivo experiments in mice by Etrych et al., showed that the treatment of EL4 T cell lymphoma using HPMA copolymer conjugated containing doxorubicin significantly inhibited the tumor growth and prolonged the mean survival time longer than 80 days compared with the 55 days for animals treated with free anticancer drug [91]. Nishiyama et al., reported 20-fold higher circulation time and enhanced therapeutic efficacy of cisplatin conjugated to PEG-*b*-PGlu block copolymer micelles than that of the free drug administered to treat solid tumors in mice [92].

Recently natural polymers derived from biological systems including proteins, oligonucleotides, and polysaccharides or antibodies to bind selectively to a receptor agent [93, 94], emerged as promising drug carriers. They possess low toxicity and potentially favorable pharmacokinetics in the circulation. Several investigators have used nucleic

acid ligands or aptamers for therapeutic and diagnostic targeted-delivery applications [95-97]. In a work by Huang et al., DNA aptamer SGC8C conjugated with doxorubicin (Dox) show excellent specificity for killing T-cell acute lymphoblastic leukemia [98]. SGC8C-Dox conjugates show a 6.7-fold increase in toxicity to their target CCRFCEM cells when compared to that of NB-4 cells. Moreover, the possibility of assembly 2D and 3D DNA/RNA base pair for the control release of small chemicals is under exploration [99, 100]. DNA architectures have been tested for several drugs including doxorubicin[101], CpG [102], and siRNA [103].

1.1.1.2. Effect of Nano Particles Shape and Size of Drug Delivery

For nanoparticles, the size selection is critical for the success of particulate drug delivery system. Particles <20–30 nm are easily cleared through renal excretion [112, 113]. Particles larger than 200nm can be uptake by phagocytosis and endocytosis in the liver, the spleen, and to a lesser extent, in the bone marrow [114-116]. Nanoparticles in the size range <150 nm can escape from the circulation through openings in the tissue walls called fenestrations. Therefore, most of the data in the literature report particle size between 60 and 250 nm for intravenous applications [117]. Alternatively, modifications in the surface chemistry of nanoparticles can help to avoid obstacles, lead to target-specific accumulation, and delay immune clearance [118, 119].

The particle shape also plays an important role in the effectiveness of the delivery of nanoparticles. Variations in the particles shapes may cause significant differences in the hydrodynamic forces while flowing in the blood stream. These differences can lead for instance to the accumulation of particles at the vessel walls avoiding or favoring the drug delivery depending on their final objective [104]. Muro et al., studied the effect of

polystyrene particle size and shape on the delivery of intercellular adhesion molecule 1 (I-CAM1) in mice. I-CAM1 is a transmembrane glycoprotein that is upregulated in many types of pathologies and used as a target for intra-endothelial drug delivery. Authors found that endocytosis was mainly ruled by carrier shape. Elongated shape particles showed a prolonged half-life in the circulation and demonstrated more specific endothelial targeting than spherical carriers. Furthermore, the particle size control the intracellular trafficking making endothelial targeting more readily as the diameter of the spherical particles is reduced [105].

1.1.1.3. Limitations of Molecular and Nano Size Biopolymers DDS

When an in situ sustained release of therapeutic agents for long periods of time is required, DDS using drug modifiers are not the best choice [56, 90, 105, 106]. A major drawback for the use of block copolymers is their instability in the reticuloendothelial system (RES) [56, 106]. Therefore, correlations between in vitro and in vivo studies constitute a significant challenge to researchers in the field. Some innovative approaches have been done in order to increase the stability of the micelle drug carriers or block copolymers. For example, functionalization of block copolymers with cross-linkable groups [107, 108] and the substitution of block copolymer micelles with specific ligands to allow targeted drug delivery [109, 110]. Though, for many polymeric micelle systems, promising in vitro stability and efficacy, do not translate into long-circulating vectors when investigated in animal models. Moreover, in the case of natural biopolymers, their premature uncontrollable degradation limits their application as DDS in humans [111-113].

In addition, despite the notable development in the design of nanoparticle-DDS for about 30 years, only a few of nano-delivery carriers have reached the market [114-117]. Poor drug loading, usually less than 5% (w/w), and rapid release became the main obstacles to overcome [118]. PEG coating of the liposomes nanoparticles demonstrated to improve drug stability and circulation for a longer time; however, it also enhanced drug retention, and diminished cellular uptake of the drug from PEGylated carriers resulting in reduced therapeutic outcomes compared to unmodified nanoparticles [119-121].

1.1.1.4. Implantable Micro and Macro Size Biopolymers DDS

Implantable scaffolds or microparticles have higher drug loading capacity, higher stability in biological tissues and offer prolonged drug release than nano particles delivery systems including liposomes and micelles [122]. Common techniques for drug loading include drug dispersion or dissolution within the solid polymeric phase or by encapsulation in a polymeric shell [123, 124]. The drug release kinetics for biopolymers can be controlled by their composition and molecular weight which are directly related to the polymer degradation rate [125]. Manufacturing techniques allow the fabrication of polymeric scaffolds with different forms, porosities, degradation rates, and mechanical properties [126, 127]. Mechanical, thermal and biological properties of polymers can be modified by altering their stereochemistry [122].

Biodegradable synthetic polymers, like PLA, PGA, PLGA and poly-e-caprolactone (PCL), have the advantage of slowly dissolve following implantation into the body. Degradability of PLGA can be tuned by controlling the proportions of PLA and PGA in the copolymer [128, 129]. Solid films of PLA were first used for the delivery of

contraceptive steroids in rats, inhibiting ovulation for up to six month [130, 131]. PLGA have been tested for delivering pharmaceutical agents of a wide variety of types including, small molecules like antibiotics, and anticancer drugs, and large molecules like proteins in the format of films[132, 133], millirods [134] and implants [135].

Non-degradable synthetic polymers have also been tested for DDS. Their excellent biocompatibility with limited inflammatory response following implantation, make them suitable for drug delivery [136]. These polymers are often hydrophobic in nature, and suitable for long-term delivery and stabilization of hydrophobic drugs [137]. Poly(methyl methacrylate) (PMMA) is a popular non-soluble polymer tested as drug delivery carrier for hydrophobic drugs [147-149].

Natural polymers like collagen [138, 139], hyaluronic acid [140, 141] , and silk fibroin [142, 143] shows high biocompatibility and high biodegradability. Chemical modifications by cross linking natural polymers, or combination with synthetic biopolymers are normally used to improve their mechanical properties, reduce batch variation and control degradation rates. Wenk et al., developed porous Silk fibroin (SF) scaffolds with PLGA microparticles loaded with insulin-like growth factor I (IGF-I) embedded in it. Interestingly, while the degradation rates of free PLGA and PLGA embedded in SF scaffolds were similar, the in vitro IGF-I release kinetics from the SF/PLGA scaffold led to more sustained release rates as compared to the free PLGA for up to 50 days [143].

Hydrogels represent yet another approach to making scaffolds. Hydrogels are water soluble, cross-linked polymers (e.g. natural polymers such as hyaluronic acid, alginic acid, pectin, chitosan, gelatin, dextran, agarose; or synthetic polymers such as

polyesters, PEG-bis-(PLA-acrylate), PEG±CDs, PEG-g-P(AAm-co-Vamine), PAAm, P(NIPAAm-co-AAc),others; or combinations ±cross linkers) that swell by osmotic forces, but not dissolve in water [144]. The swelling extend of hydrogels and the diffusion of therapeutics out of the carrier can be regulated by controlling the chemical nature of the cross-linking [145, 146]. The advantage of using hydrogels is that they are not as rigid as other scaffold systems. Therefore, they can be injected instead of implanted. For example, Jeyanthi and Rao showed in vitro constant release rate of 5-fluorouracil from copolymer hydrogels of collagen and poly(hydroxyethyl methacrylate) [poly(HEMA)] for a period of 10 days [147].

1.1.1.5. Limitations of Micro and Macro Size Biopolymers DDS

Despite the perks that biopolymers micro and macro carriers offer for drug delivery there are some concerns that limits their applications in humans.

The use of hazard solvents like methylene chloride in the manufacturing of PLGA, and the acidity of the in situ degradation products of these polyesters are of concern [148-150]. Several studies using implants or microparticles of polyesters (such as PLGA) for tissue engineering have showed negative cellular interactions, including limited cell proliferation, tissue synthesis and inflammatory host response [151, 152]

Natural polymers show batch to batch variation, low mechanical properties, and limited processability which restrict their use for DDS applications [153]. Moreover, there are serious concerns about cross-linking of natural polymer matrices. The presence of unreacted functional groups during the crosslinking process can result in a cytotoxic reaction upon degradation [154, 155].

PMMA is a biocompatible material that has been widely used as bone cement in orthopedic surgery for the fixation of prosthetic devices and to remodel lost bone [156]. The high risk of introducing bacteria by using PMMA cements motivated the incorporation of antibiotics into the polymer intending to decrease the infections after surgery [157, 158]. High percentage of drug retention and low degradability are the main drawbacks of PMMA DDS. Moojen et. al., studied the release kinetics of antibiotics from three commercial PMMA products, cement spacers and polymer beads loaded with high dose of the antibiotics during 6 weeks. Even when all carriers were able to provide concentrations of antibiotics above MIC, high drug retention (>90% for the cements, and >60%for the beads) were measured for all carriers [159]. In clinical practice, the gentamicin loaded PMMA beads are usually removed after 14 days post implantation, requiring additional surgical intervention. Several studies have shown that permanent antibiotic-PMMA implants can release the residual antibiotic at concentrations below MIC for a long time leading to recovery of antibiotic-resistant bacteria [160, 161].

The low mechanical strength of hydrogels poses significant difficulties in handling. Moreover, it is difficult to load drugs and cells then crosslink the construct in vitro as a prefabricated matrix, and it is difficult to sterilizes [144].

1.1.2. Bioceramics

Bioceramics offers an interesting alternative for DDS because it is feasible to produce ceramic matrices with large specific surfaces and high degrees of porosity. Materials in the families of calcium phosphate [162-164] and silica [165, 166] are very attractive for DDS applications. For particles in the micro scale, biodegradation and porosity are the main variables that control the DDS. Several approaches have been tested

for bioceramics in drug delivery applications including: nanoparticles to encapsulate the drug in a bioceramic shell such as hollow silica [167, 168] or calcium phosphate [169], or mesopores bioceramics with or without metallic-gate keepers [165, 170]. The second category includes the incorporation of the drug in the sol during ceramic preparation by sol-gel method or mixing the drug with ceramic cement [171, 172]. The third design is the incorporation of the drug onto a porous ceramic scaffold matrix by adsorption or using a linker [173, 174].

1.1.2.1. Nano Size Bioceramics as DDS

In many cases nano and micro particles are preferred than scaffolds when non-invasive procedures such as injection or ingestion are desired. The crescent technology in the nano and micro fabrication allows the development of new and sophisticated particles of different materials, size, surface chemistry, shape and biodegradability [3]. Furthermore, particulate DDS can be formed by therapeutics entrapped or mixed with the biomaterial carrier with or without the help of ligand agents. The wide spectra opened for the use of particles for DDS applications has spurred much funding and research aimed toward the use and optimization in the field [111].

Ca-P nano particles have been tested as delivery vehicles for growth factors, antibiotics, anticancer drugs and anti-inflammatory agents [175-177]. Altering Ca-P chemistry, surface area, surface charge, and crystallinity significantly affects drug bonding and release. Hanifi, et al. [178], showed that doping HAp nanoparticles with Mg_2^+ changed the surface charge of the particles and significantly increased the material capacity to adsorb DNA. Dasgupta, et al. [179], incorporated Mg_2^+ and Zn_2^+ in HAp nano particles increasing the amounts of BSA absorbed when compared with undoped HAp.

The enhanced BSA adsorption was attributed to unit cell deformation caused by the dopants. However, no significant difference in the drug release profiles from dope or undope HAp were observed. Sustained drug release of BSA was observed during 6 h. Stigter, et al., coated Ti_6Al_4V alloy with a Ca-P-drug layer employing biomimetic co precipitation in SBF solution saturated with several antibiotics [180]. The release of the antibiotics was related to their chemical nature (acid or basic), molecular size and their ability to diffuse in the releasing media. Authors attributed these changes to chemical binding between carboxylic groups in the antibiotics with calcium on the ceramic coating resulting higher incorporation and slower released kinetics [181]. However, plateau in the cumulative release profiles was observed after 7h of incubation in SBF for all antibiotic tested.

Porous SiO_2 structures with small uniform pore sizes (1.5-10 nm), total porosity in the order of 80%, and large surface areas (>1500 m^2/g) are attractive for DDS [182, 183]. Depending on the porosity characteristics and the surface chemistry (functionalization[184]) , the dissolution rate and the drug release kinetics can be controlled [185]. The pore size can be manipulated [166, 186, 187], given a wide clearance for the type of molecules that can fit into (anti-cancer agents [188-190], steroids [191], analgesics [192], and proteins and peptides [193]). Moreover, encapsulation of drugs inside the mesopores (MSP) has been achieved by using metal ions (e.g. Cd) or molecules (e.g. CdS) as gatekeeper g to cap the pores and to regulate the release of drug molecules. Lai, et al. [194], used CdS^- to cap MSP particles for the delivery of ATP and Vancomycin. Torney, et al. [195], used Au^+ caps on MSP particles for the delivery of β-oestradiol and DNA. These experiments demonstrated the capacity

of the gate keepers to maintain drug molecules entrapped in the nano carriers until reach the desired tissues. Afterwards molecules were liberated using chemical or physical triggering agents. Both authors showed that after uncapping the gaps chemicals were released from the nanoparticles in less than 24h.

1.1.2.2. Limitations of Nano Size Bioceramics as DDS

Similar to biopolymer, nano bioceramics particles show limited drug loading capacity and rapid release kinetics. A major concern in the use of nanoparticles for drug delivery system is the lack of reliable techniques to evaluate the side effect that can be connected to them [196-199]. For instance, there are serious concerns about the use of porous SiO_2 nanoparticles due to its high dissolution rate and the presence of chemical species like silane which are chemically reactive and cytotoxic. This opens a big question mark about the convenience of using Silica nano carriers for DDS. For example, He Q., et al., [200], reported significant cytotoxicity of spherical silica mesoporous nano particles (190–420nm in diameter) at concentrations above 25mg/mL, and microparticles (1220nm in diameter) at concentration range 10–480 mg/mL. However, as a consequence of reducing the concentration of nano particles that can be used as DDS, the amount of drug that could be delivered is also reduced. Lin, et al., [201], and Yu, et al., [202], demonstrated that cytotoxicity of amorphous porous and nonporous silica nanoparticles against red blood cells and HEL-30 cells respectively can be significantly reduced by controlling particle size and porosity. In spite of the attractive properties offered by MSPs, more investigation and in vivo studies need to be performed to determine the viability of using MSPs for drug delivery applications.

1.1.2.3. Cement or Ceramic Sol as DDS

Calcium phosphate cements CPC are formed by mixing the ceramic powder with aqueous solution at room temperature and allow it to set under physiological conditions [171]. After the setting reactions inside the body CPC have only two end products: HAp and brushite (DCPD) [203, 204]. CPC form a moldable/injectable paste which represent a significant advantage with respect drug delivery [205]. The low temperature at which CPC reactions take place together with their intrinsic porosity allows the use of this material as a drug carrier. Numerous therapeutic agents have been tested for drug delivery from CPC including antibiotics, anticancer, anti-inflammatories, proteins and growth factors in vivo and in vitro. Contradictory results can be found in the literature about the efficacy of CPC as drug delivery systems. For instance, some studies have showed high rates of drug release with low retention within the first 24 h [32, 206-208]; while some others have showed just the opposite [209-212]. Moreover, differing reports showing either deterioration of drug activity due to the interactions between the drug and the carrier, or successful drug deliver preserving drug bioactivity have been also reported. Jiang et. al., analyzed the release kinetics of the antibiotic Vancomycin hydrochloride (Vanc) from HAp cement and DCPD cement. Equal amount of drug were loaded by mixing with the cement reagents. Release kinetics studies showed that Vanc was released faster from the brushite cement than from the apatite cement matrix during 5 days. All the measurements for both carriers were above the minimum inhibitory concentration (MIC). Interestingly, only the drug eluted from brushite cement inhibited bacterial growth during the elution period. Authors attributed this effect to the degradation of the drug caused for the alkaline pH of the apatite cement during setting [213]. In a different study by Urabe

et al., release kinetics of Vanc from HAp cement was also measured. Authors found drug concentrations above the MIC for up to 8 weeks. Microbiological assay demonstrated the bactericidal effect of the aliquot with stretch correlation to the concentration measurements [214]. Hence, nonetheless the extent amount of studies, more needs to be done in order to optimize the use of CMC as platforms for DDS.

Similar to CPCs, sol–gel processed porous silica glasses have a considerable potential as carriers for controlled drug release [215-217]. Silica xerogels results from the hydrolysis of tetraethylorthosilicate (TEOS), followed by gelation, aging, and drying. All steps carried out at room temperature. The resulting gels are solid glassy material termed xerogels [172, 218]. The low processing temperature allows the incorporation of drugs dissolved in water or other solvent during the sol stage before the gelation process. This leads to the high drug loading efficiency, and homogeneous distribution of drug in the sol-gel [218, 219]. Several authors have published the drugs retained their activity after their delivery from silica xerogels, including ibuprofen, antibiotics, growth factor and anticancer drugs [6, 216, 218, 220-223].

Degradability of silica xerogels can be adjusted by modifying processing parameters such as the composition of the sol, the type and course of reaction, the drying temperature, the pH of the sol and the type and concentration of the catalyst [215, 224-226]. Currant et. al., significantly affected the porosity of silica xerogels by decreasing pH of the TEOS reactions. Acid-catalyzed hydrolysis has been used as a strategy to increase the surface area and porosity of the former for drug delivery applications [218, 227, 228]. Moreover, additional sintering step after the gelation below 900^{o}C can significantly reduce the degradation of the material and prolong the drug release. In two

different works by the group of Kortesuo et. al., increased the release of toremifene citrate loaded from silica xerogel by adding a sintering step at 700^{o}C after the gelation [221, 229] , but eliminate the possibility of drug incorporation during processing, decreasing the loading efficiency. It has also showed to be biocompatible in vivo as they are degradable inside the body which degradation products ($Si(OH)_4$) can be easily eliminated through the kidneys [222]. It has been shown that alkalyne drugs release in a sustained manner whereas neutral drugs are released very quickly from silica [217].

1.1.2.4. Limitations of Cement or Ceramic Sol as DDS

The use of CPC as drug carriers is not a straight forward task towards the proper design of CPC delivery systems. Parameters such as cement microstructure [230], drug loading strategy [231], drug concentration [232] , chemistry of the drug [233], and others [234, 235], significantly affect the release behavior. Common strategies to incorporate the drug in CPC are either by combination with the cement reagents or by impregnation of the pre-set CPC solid block or granules. Even when the first strategy can improve the drug-carrier homogeneity, it can interfere with mineral precipitation and inhibit mineralization of the cement [32, 236]. Therefore, microstructure and mechanical properties of the CPC carrier are correlated with the presence and concentrations of drug molecules [236-238].

Release kinetics of drugs from promising xerogels DDS tends to is characterized by a very sharp initial burst followed by little release in later stage (for hydrophilic molecules), exhibiting a great disadvantage for long term sustained drug delivery [218, 221, 239]. Alternative methods such as functionalization of the surface walls [240], pore

blocking with nanoparticle caps [170], and composite with biodegradable polymers, the last with higher success [241, 242].

1.1.2.5. Bioceramic Micro and Macro Porous Scaffolds as DDS

Three dimensional micro and macro bioceramic are another very plausible alternative to be used as drug delivery platforms. These carriers where first used to serve as biological tissue substitutes to restore, maintain, or improve tissue function [243, 244]. Positive biological response to micro and macro size bioceramics inside the body makes them useful for DDS. As a major advantage these systems stay in the place of implantation without further travel into the blood stream, liberating therapeutics in situ.

Bioceramics used for DDS includes nearly inert ceramics (e.g., alumina and zirconia), bioactive ceramics (e.g., hydroxyapatite and bioactive glass-ceramics), and resorbables ceramics (e.g., tri-calcium phosphate and bioactive glasses) [245]. Calcium phosphates (CaP) and bioactive glasses (BG) are regarded the most attractive bioceramic for DDS due their biological reactions with cells and live tissues.

Amid calcium phosphates, hydroxyapatite (HAp) is very popular since this has a similar chemical composition to the inorganic component of bone [246]. Porous HAp scaffolds have proven to successfully serve in the bone tissue regeneration in vivo [247, 248]. Therefore, HAp has been mainly used as an effective carrier of growth factors to stimulate bone cells and to accelerate tissue ingrowth [249, 250]. Several works have tried to enhance the functionality of HAp scaffolds by controlling its porosity. Fabrication techniques including the use of polymeric matrices removed by pyrolysis [251], 3D prototyping [252], foaming methods [253], and by forcing gas inclusions [254], have been intended. The combination of macro and micro interconnected porosity created

by these methods resulted convenient for DDS applications. Uchida et al., showed the successful use of porous hydroxyapatite blocks for the delivery of anticancer drug (Cis-platinum) in vitro and in vivo during 12 weeks [255].

Combinations of HAp with more soluble CaP like tri-calcium phosphate (TCP) have been tested to improve the degradability of HAp [256]. Guicheux et. al., tested the commercial Triositet® macroporous biphasic calcium phosphate consisting of a ceramic with a 60/40 HAp/b-TCP for the loading and release of human growth hormone (hGH). In vitro results showed burst release within the first 48h followed by slower sustained release for 8 days with negligible drug retention. In vivo results showed partial resorption of the 60/40 HAp/b-TCP scaffolds [257]. Alternatively, introduction of crystal defects such as ionic substitutions have been also tested. Thermodynamic destabilization and diminution of the crystallinity of HAp by incorporation of CO_3^{-2}, Mg^{2+}, or Sr^{2+} ions can increase the solubility and drug adsorption capability of the apatite [258-260]. Christoffersen et al., found an increase in the dissolution rate of HAp when calcium ions were substituted with strontium ions in molar concentrations from 1 to 10% [261].

Bioactive glasses are a group of glasses able to bond bone chemically [245]. Basic compositions of BG are within the molar ranges: 38-65.5% SiO_2, 15-30% Na_2O, 10-25% CaO, and 0-8% P_2O_5 [262]. BGs have showed higher bioactivity and degradation than HAp under physiological conditions [263, 264]. The dissolution of the glass can be controlled by varying particle size, glass type, and volume fraction of powder in physiological solutions [265, 266]. BG porosity can be tuned by similar methods mentioned for HAp [267-269]. Commercial available 45S5 Bioglass® have been extensively tested for tissue engineering and drug delivery applications [173, 270-272].

Nandi et al., studied the antimicrobial activity in vitro and in vivo of antibiotic cefuroxime axetil (CFA) from porous BG ceramic blocks bioactive glass (BG) prepared by normal glass melting procedures. Concentrations of antibiotic were measured above the MIC during the first 6 days of the in vitro experiment. Furthermore, antibiotic impregnated BG showed to be effective against osteomyelitis induced in the tibia of New Zealand rabbits [272]. Domingues et al., also evaluated the antimicrobial activity in vitro and in vivo of BG particles prepared by sol-gel method and loaded with antibiotic tetracycline. This time in vitro test showed a drug elution burst of 12% antibiotic from the BG within the first 8h, followed by a sustained controlled release for up to 80 days. However, the bactericidal effect of the aliquots from the in vitro test or BG-drug DDS were not evaluated for the same period of time [173]. None of the authors analyzed either the degradation rate of the BG or the drug-BG interactions which can help to explain the significant differences found in the release kinetics of antibiotic from BG.

1.1.2.6. Limitations of Macro and Micro Bioceramics DDS

Each of these materials system has limitations and special considerations. For example, how much drug can be loaded, what types of drug molecules are compatible, and what kind of dosing characteristics are desired.

Biodegradability of Ca-P micro and macro carriers has been a problem because some show an accelerated resorption rate (β-TCP, Rhenanite) whiles others hardly resorbs (HA). [273, 274]. Moreover, a major challenge in the use of scaffolds DDS is that they might be favorable to the growth of bacteria.

BGs limitations are related to high processing temperatures, narrow range of bioactive compositions, low mechanical strength, and limited textural features [275].

Processing and drug loading procedures can significantly affect the release kinetics of therapeutics from BG.

1.1.3. Composite Biopolymer-Bioceramics

Composites scaffolds made of ceramics covered or integrated with polymers have been develop in order to take advantage of the virtues of both materials for DDS. Tunable degradability, alteration of the mechanical properties and drug release kinetics can be achieved by the addition of polymers to bioceramics [276-278]. Biphasic calcium phosphates (BCP), CPC, HAp, and BG have been already combined with natural and synthetic polymers, and tested for the delivery of small and large molecules [24, 279-286]. Soriano et al., achieved to extend by 4-fold the sustained release of gentamycin from blended CaP-PLA scaffolds compared to commercial PMMA beads [287]. In vitro study by Schnieders et. al., incorporated PLGA microparticles in CPC scaffold and achieved to eliminate burst release showed in the PLGA alone yielding to a sustained constant drug release for up to more than three month from the PLGA-CPC composite [288]. Itoh et. al., showed that scaffolds of collagen mixed with HAp nanoparticles and loaded with growth factor rhBMP2 implanted in rats and dogs showed high osteoconductive activity and is induced bone regeneration [289]. However, undesirable properties can also result depending on the materials combinations and the way how they are incorporated in the ceramic-polymer. Habraken et al., showed that combination of CPC with gelatin microparticles can increase the injectability of the cement but at the same time inhibit the degradation of the polymer [290]. Same group of researchers found that incorporation of PLGA into a CPC reduced the injectability, compression strength,

and increased the cement setting time in manageable ranges [291]. Therefore, careful analysis of the composited must be done for their specific applications as DDS.

1.2. SCPC as Drug Delivery System

1.2.1. What is SCPC

Silica calcium phosphate composite (SCPC), US patent No 7,223,414 B1 2007, is a bioactive resorbable nano composite ceramic [292]. SCPC ceramic is prepared by mixing and sintering an organic or inorganic silica salt (0.3-0.6 molar ratio) with a calcium phosphate. The initial molar composition, and the sintering parameters selected to process the ceramic composite have a crucial effect in its final microstructure [18, 293-295]. This fact allows engineering custom made SCPC composites for specific tasks. The two main crystalline phases of SCPC are solids solutions of β-rhenanite (β-$NaCaPO_4$) and α-cristobalite (SiO_2) [18, 293]. In previous works by El-Ghannam et al., SCPC has showed superior bone regenerative capacity, resorbability and mechanical properties compared with commercial bioactive glass and hydroxyapatite [293, 296]. The superior biological response has been associated with the stimulatory effect on osteocytes of the dissolutions products of SCPC in physiological conditions [293, 297]. The elemental solid solutions, measured in the main crystalline phases of SCPC, and the large surface area of the material seems to rule these dissolutions. In addition, the superior mechanical properties are attributed to its particular microstructure with high density of grain boundaries due to the nanometric size of its crystalline phases, and its homogeneous hierarchical pore size distribution, including nano pores in the range 50-100nm and micro pores in the range 10-300 μm[293, 294].

1.2.2. DDS Applications of SCPC

SCPC has demonstrated its ability as a potential platform to deliver several therapeutics including antibiotics, anticancer drugs, and growth factors.

El-Ghannam, showed up to doubled adsorption of serum protein loaded on SCPC ceramic particles with different chemical compositions and heat treatments than that measured on commercial bioactive glass [293]. Moreover, the chemical composition and phase distribution of SCPC regulated its capacity to adsorb serum protein. Higher amounts of silica-rich phase significantly increased the serum protein adsorption. In addition maturation in crystallization of β-rhenanite and α-cristobalite by adjusting heat treatment parameters have resulted in enhanced protein adsorption. The effects of porosity and surface area were not addressed in this study. El-Ghannam et. al., showed superior sustained release of rhBMP-2 protein from SCPC when compared with porous HAp loaded under similar conditions [287]. In this study, bone marrow cells incubated with medium released from SCPC-rhBMP-2 expressed 10 times more alkaline phosphatase activity and doubled the production of mineralized extracellular matrix than those incubated with HA-rhBMP-2 medium in the same time period. Comparable total porosity and surface area were measured for both SCPC and HAp. But, SCPC showed a wider pore size distribution including pores in the nano and micro range while HA only exhibited pores in the micro range. Prolonged release kinetics of SCPC was associated to the presence of nano pores that served as pockets for the storages of the protein, and to dissolution-precipitation reactions taking place on the surface of the SCPC, controlled by its surface chemistry and crystalline structure.

In similar studies SCPC has been tested as carrier for the release of antibiotics. EL-Ghannam et al., tested different particulate SCPCs ceramic for the delivery of antibiotic gentamicin for up to 28 days [298]. It was reported that differences in the chemical composition of SCPC significantly altered the porosity, pore size distribution, and surface area of SCPC carriers. Authors attributed the major changes with the SiO_2 content in the SCPC, and found that increasing the silica content in the composite, surface area and average pore diameter was also increased. Interestingly, it was observed that SCPC with the largest surface area loaded fewer amount of drug, but at the same time, showed prolonged release of gentamicin above MIC with respect to the other two compounds. El-Ghannam et. al., demonstrated that SCPC carrier have superior effectiveness for Vancomycin (Vanc) loading and release than low resorbable polymethylmethacrylate (PMMA) widely used in the treatment of bone infection over the last three decades [299]. The amount of Vanc adsorbed on the surface of SCPC was more than 100% superior to that adsorbed on the PMMA particles surface per mass unit under the same experimental conditions. Moreover, at all-time points, the concentrations of antibiotic released from the SCPC carrier were always superior to those measured from the biopolymer. Moreover, drug concentrations eluted from SCPC-Vanc hybrids showed to be above the MIC keeping its bactericidal effect for up to 44 days against *Staphylococcus aurous*, while only 14 days for PMMA. In addition, SCPC showed only a 4.5% of drug retention compared to 68% of the PMMA, and superior degradability with 40-44 % mass in comparison of 0.5-1.5% measured for PMMA. The effect of the porosity and surface area were not addressed in this study.

Different compositions of SCPC have been also tested for the release kinetics of anticancer drugs showing promising results. The loading and release kinetics of anticancer drug 5-Fluorouracil (5-FU) from two different formulations of SCPC (19.5% SiO_2 and 32.9% SiO_2) were analyzed [300]. The two samples showed comparable loading capacity per unit mass of ceramic, and also showed similar cytotoxicity against 4T1 mammary tumor cells. Release kinetic of anticancer drug from discs made of Si-rich SCPC-5FU hybrid was tested in vivo and in vitro. In vitro results showed sustained release of therapeutic dose of 5-FU for up to 32 days. Moreover, in vivo study, using a breast tumor model in mice, demonstrated that the tumor growth was stopped in those animals treated with SCPC-5FU hybrids which did not happened with control animals treated with SCPC alone or without any treatment. In fact, 75% tumor reduction indicated the bioactivity of the drug eluted from the SCPC carrier. Surface area, porosity and pore size distributions were not evaluated this time. Vedantham et al., compared the capacity for loading and release Cisplatin (Cis) from the same two formulations of SCPC [301]. This time porosity, surface area, and pore size distribution, were reported; and significant differences with respect to chemical composition were detected. Silica-rich SCPC showed a 20-fold higher surface area and wider pore size distribution (in the nano-range) than that measured on the other sample. As expected drug loading capacity of Silica-rich SCPC was superior to the other sample, but only by 1.6-fold, which does not correlate with the major difference in surface area. Release kinetics profiles were also very different between the two samples. Whereas silica rich SCPC showed burst release of 37% of the initial Cisplatin loaded, followed by a sustained release for up to 1 moth with only 15% of drug retention, the other SCPC sample showed 27% of burst release,

followed by a sustained release for only 12 days with 50% of drug retention. The enhanced drug delivery capacity of the silica-rich SCPC was corroborated by measuring the cytotoxicity of solution incubated with the ceramic drug hybrids against rat H4IIE hepatocellular carcinoma cells. Table 1.1 is a summary of various materials for the delivery tested for drug delivery of different kinds of therapeutics, including SCPCs.

Table 1.1: Low molecular weight drugs incorporated in biopolymers and bioceramics. Examples of main in vitro drug release results.

Carrier	Carrier format	Drug	Amount of drug laded or loading efficiency	Porosity parameters	Surface area	In vitro release experiment	Burst release	Sustained release	% drug retention	Ref
HAp cement & HAp cement +65µm Vanc loaded PLGA particles		Vancomycin	17.8 mg drug/g HAp cement loaded with PLGA microspheres or 50 mg Vanc/g HAp cement	HAP cement + PLGA particles 40.2<x<54.4 % or HAp cement 43.5<x<55.8 %	6.35<x< 13.33 m^2/g	500-700mg of carrier in 5 mL PBS with full replacement of PBS at each time point	46.3% for high porous & 16.8% for low porous HAp cement in 2h; or 23% for high porous & 19% for low porous HAp cement with PLGA microspheres	20d for HAp cement, or 40d for HAp cement with PLGA microspheres	10% for HAP cement or 20-40% for HAP cement with particles	[302]
Porous HAP	blocks 10x10x10 mm^3	Gentamycin	a cavity in the middle of the block was made and 75 mg of drug was inserted and holes sealed with TCP	30-40%		5mL PBS full replacement daily	15% of drug was released in 6d	70% in 120d	30%	[174]
Si xerogel discs	disks 11mm diameter & 5.5 mm thickness	Vancomycin	1.1 mg/g gel; 2.2 mg/g gel; 11.1 mg/g gel	pore volume 0.35-0.48 cm^3/g, average pore diameter 1nm	841.8-790.2 m^2/g	SBF 2-10 mg loaded xerogels in 2 mL SBF full replacement	burst stage 7-26.5 µg/h up to day 14	0.64-3.2 µg/h up to day 21	10% after 42 days	[172]
Si xerogel discs	discs 4.7 mm diameter and 0.9 mm height	Toremifene citrate	33 mg/g			250 mL PBS with 2 mL replacement at each time point	no burst release	90 h	10%	[221]

Table 1.1: (Continued).

Mesoporous bioactive glass doped with boron 0-10%	blocks 5x5x4 mm^3	Dexamethasone	275-350 µg/g	pore volume 0.392-0.207 cm3/g and pore size 5.086<x<5.285 nm and total porosity from 78-90%	265-194 m^2/g	immersion of blocks in 4mL PBS total replacement	40% after 6h	350h	10%	[303]
HAp ceramic blocks	1.3 cm^3	Cisplatin	10 mg incorporated in a cavity drilled in the center of the scaffold	58.48-82.63%		immersion in 100mL of isotonic phosphate buffered solution	0-30% in 8h	168h	58.15-78.4% after 168h	[304]
Bioactive glass with or without chitosan coating	cylinders 12mm height	Gatifloxacin		68.72%, unimodal pore distribution 10-70 um		5 mL of PBS total aliquot change	% in 3h, Ofloxacin	% in 24h, tetracyclin burst	3% no chitosan, and 45-75% depending chitosan layer thickness	[305]
27%TCP, 52% brushite and 21% monanite covered and uncovered with PLGA	cylindrical samples 10mm diameter x 5mm height	Vancomycin		26% porosity with average pore size 12.3um		24 h while HAP burst	% in 48% the release from loading by immersion and vacuum from brushite: Vanc burst	% 3h sustained		[206]
Porous silica HAP composite with or without PLGA layer	particles	Gentamycin	250-400 mg/g	average pore size 3.3nm	332 m2/g	100mg particles immersed in 20mL PBS total media replacement	60% in 1h	100% in 12h		[316]

Table 1.1: (Continued).

Brushite, Monenite and HAP	cylindrical samples 3D printed 10mm diameter x5mm height	Vancomycin, Ofloxacin and Tetracycline		Loading Vanc by immersion brushite 3.546, monenite 9.22 mg/g and HAP 20.16 mg/g by vacuum brushite+Va n 1.29mg/g, Brushite + Ofloxacin 1.36 mg/g and brushite + Brushite 2.38m^2/g, Monenite 5.24 m^2/g and HAP m^2/gtetracycl ine 16.9 mg/g		Immersion of blocks in 10mL PBS total replacement	Release of Vanc from Brushite and monenite burst 80% in 1h, HAp burst 60% in 3h; release of vacuum loaded drugs from brushite Vanc burst 80% in 3h, ofloxacin 65% in 3h, tetracyclin 20% in 3h; release of Vanc from brushite covered with plga 10% burst 60% 2h, 30% burst 40% 2h and 50% 10% 2h.	Release of Vanc from Brushite and monenite sustained 100% in 1d, HAp sustained 100% in 1d; release of vacuum loaded drugs from brushite Vanc and ofloxacin 100% in 1d, tetracyclin 25% in 1d; release of Vanc from brushite covered with plga 10% burst 100% 2d, 30% burst 65% 2d and 50% 40% 2d.	Retention Vanc from Brushite and monenite sustained 0% in 1d, HAp sustained 0% in 1d; of vacuum loaded drugs from brushite Vanc and ofloxacin 0% in 1d, tetracyclin 25% in 1d; release of Vanc from brushite covered with plga 10% burst 100% 2d, 30% burst 65% 2d and 50% 40% 2d.	[306]
Gelatin hydrogels with different water content	Sheets 1.2x1.2cm^2x 1mm think MW 100000	Cisplatin and Adriamycin	40µg Cisplatin, 120µg Adriamycin loaded by impregnation in the middle of the sheet			immersion in 10 ml PBS, 5mL replaced at each time point	Cisplatin 8-20%, Adriamycin 60-80% in 6h	no further release after burst	80-92% Cisplatin and 20-40% Adriamycin	[307]
SCPC50 and SCPC75	discs 5mm diameter - 3 mm height	Cisplatin	SCPC50 18.62 mg/g and SCPC75 29.25 mg/g	total porosity SCPC50 54% and SCPC75 70%	SCPC50 3.120 m^2/g and SCPC75 18.3 m^2/g	immersion in 5mL PBS, 1mL refreshed at each time point	SCPC50 26%, SCPC75 37% in 24h	SCPC50 50% in 6d, SCPC75 85% in 33d	SCPC50 50%, SCPC75 75%	[319]

Table 1.1: (Continued).

3 commercial PMMA; palacos, simplex and septopal		Gentamycin and Tobramycin	palacos 40g/0.5g gentamycin, simplex 40g/1g tobramycin and septopal 120 beads/4.5mg gentamycin/bead			samples immersed in 1L PBS with 25% replacement at each time point	from palacos 50% in 1d, from simplex 50% 1d and from septopal 12% 1d	from palacos 62.5%/6d, from simplex 60% 6d and from septopal 37% 42d	from palacos 37.5%/6d, from simplex 40% 6d and from septopal 63% 42d	[308]
CPC-b-TCP with 2 different Sr doping	cylinders 10mm diameter x 5m high	Doxycycline hyclate	20-28 mg doxycycline/g ceramic	Average pore diameter 146-239 nm and porosity 31-36%	5.1-8.9 m^2/g	immersion in 8ml PBS total replacement	burst 60-95% in 6h	100% from 8-24h		[32]
SiO_2 glass doped with 0.0, 2.5, 5.0 and 10.0% Sr	45µm particles	Dexamethasone	0.0%: 1.38 mg drug/g ceramic; 2.5%: 0.93 mg drug/g ceramic; 5.0%: 0.60 mg drug/g ceramic; 10.0%: 1.95 mg drug/g ceramic	Average pore size 0%Sr: 2.8 nm; 2.5%Sr: 4.0nm; 5%Sr: 4.8nm; 10%Sr: 5.4nm.	surface area 0%Sr:0.8m^2/g; 2.5%Sr: 7.0m^2/g; 5%Sr: 6.0m^2/g; 10%Sr: 209m^2/g.	40 mg of loaded particles immersed in 4mL of PBs 50% refreshed at each time point	Burst in 10h:	Sustained release in 28d	Retention	[309]
							0%Sr: 15%;	0%Sr: 27%;	0%Sr: 73%;	
							2.5%Sr: 17%;	2.5%Sr: 35%;	2.5%Sr: 5%;	
							5%Sr: 26%;	5%Sr: 52%;	5%Sr: 48%;	
							10%Sr: 12%	10%Sr: 20%	10%Sr: 80%.	
SiO_2 glass doped with 0.0, and 10.0% Sr	scaffolds 7x7x7mm3	Dexamethasone		including large pores 400um, total porosity 90%		scaffolds immersed in 4mL of PBs 50% refreshed at each time point	Burst in 1d	Sustained release in 336h.	Retention	[309]
							0%Sr; 65% and 10%Sr:30%	0%Sr: 90% 10%Sr: 40%	0%Sr: 10% and 10%Sr:60%	
0%, 5% and 10% Fe mesoporous bioglass	particles	Dexamethasone		mesoporus average size 5nm, with total porosity 82-83%	from 350-268 m^2/g	samples immersed in 4mL of SBF	70% burst 1d	80% 10d	20%	[310]

Table 1.1: (Continued).

mesoporous bioactive glass and bioactive glass	blocks 0.5g	Gentamycin	12.33% in MBG and 5.03% in BG	pore volume MBG .348cm^3/g, BG 0.099cm^3/g	MBG 334.4 m^2/g, BG 86.7m^2/g	in 20mL of SBF	MGB 50% 16h, BG 70% 16h	MBG 60% 170h, BG 90%/16h	MBG 40%, BG 10%	[311]
BCP loaded with drug and compacted at different pressures	particles 200-500 um	Vancomycin	47.6 mg Vanc/g ceramic	% porosity from 40-10%		250 mg Vanc loaded particles in 13 mL in DI water total replacement	60% in 8-16h	depending on the pressure from 60-100% from 24-144h	40-0%	[312]
Porous HAP and porous TCP	cylinders 10mm diameter x 10mm height coated and uncoated with chitosan	Ceftriaxone sodium and Sulbactum sodium 2:1 w/w	2.85 mg in HAP and 2.7 mg in TCP per cylinder	total porosity HAP 67.32% and TCP 55.74%, pore size distribution 3.5-300µm and 2.9-300 µm	HAP 0.5m^2/g and TCP 0.64m^2/g	immersed in 50 mL of PBS aliquots of 2mL volume were removed at each time point	100% in 2h, covered with chitosan 47% in 6h	50% in 20h	50%	[313]
Bioglass 58S and mesoporous BG M58S and M77S	particles	Gentamycin	58S: 10.3 w/w%, M58S: 36.4w/w% and M77S 48.6w/w%	pore volume 0.17 cm^3/g, 0.54 cm^3/g and 0.73 cm^3/g	58S 58.98 m^2/g, 277.62 m^2/g and 400.05 m^2/g	50mg of loaded powder in 10 mL SBF	50-65% in 1d	60-85% in 20d	40-15%	[314]
Chitosan and CaPglass+b-TCP+chitosan, 10/090, 5/5/90 and 0/10/90 molar ratio	blocks 7x7x5 mm3	Gentamycin				scaffold immersed in 10mL of PBs, 2mL refresh	just chitosan 77%/12h, after glass and TCP adding 40%/12h	just chitosan 100%/20d and chitosan + glass+ TCP 98%/20d		[315]

Table 1.1: (Continued).

Porous silica HAP scaffold with or without PLGA layer	sintered microspheres scaffolds	Gentamycin	240-125 mg/scaffold	30-40% with pore size 110-130 µm		150 mg scaffold immersed in 20mL PBS total media replacement	60-65%/1h	100% in 30h		[316]
Bis(p-carboxyphenoxy) propane sebacic acid	rods 8x0.9 mm	5-Fluorouracil	15% w/w			in PBS	70%/40h	100%/172h		[317]
SCPC75 compared to PMMA	SCPC75 particles and PMMA beads	Vancomycin	0.5% w/w on SCPC75 and 0.2% w/w on PMMA beads			immersion of 0.2g carriers in 12 mL of PBS, 2 mL refresh at each time point	90% in 48h for SCPC75 and 50% in 6h	100% from SCPC75 in 480h, 60% in 144h	0% for SCPC75 and 40% for PMMA	[318]
Silicon-calcium phosphate with different chemical composition C3S1, C1S1 and C1S3	particles 300-425 µm	Gentamycin		from 23.5-32.3% and average pore size 44.8-70.9 nm	42.9-155.8 m^2/g	immersion of particles in 12 mL of SBF, 2 mL refresh at initial time points and 50% replacement after 48h	17-33%	100% from 480-672h	0%	[298]
SCPC75 and SCPC50	particles 150-250µm	5-Fluorouracil	37.9-40.2 mg/g			immersion particles in 25 mL of PBS with 2 mL refreshing	18% in 1h	100% in 33d	0%	[300]

1.3. Motivation and Hypothesis

SCPC has been shown to be a promising material for drug delivery system. Although numerous studies were published on the use of silica-calcium-phosphates materials, the role of ceramic microstructure on drug binding and release is not fully understood. We hypothesize that engineering the microstructure of SCPC bioactive ceramic can be used to control drug binding and release kinetics of several drugs. For instance, understanding the interactions between the drug functional groups and the active sites exposed at the surface of the biomaterial will facilitate the possibility to engineer a more effective drug delivery system, and predict in vivo behavior, saving time and money involved in the research-development process. In particular, the effect of Phosphate/Silicate ratio, crystal defects and porosity on material properties related to drug delivery such as surface charge and dissolution kinetics will be analyzed. Once the relationship is clear, material properties can be modified by changing microstructure of the ceramic composite through modification of the ceramic processing parameters. Search in the literature indicated that none of the previous studies have addressed the effect of carrier microstructure to establish correlations and predict behavior for drug loading and release. This will be the first attempt trying to use systematic approach combining microstructure–properties relationship (following the philosophy of materials science tetrahedron) to predict release kinetics in vitro and the therapeutic effect in vivo.

1.4. Objectives

The goal of the present research program was to determine from the materials science perspective the effects of SCPC bioactive ceramic microstructure on the binding and controlled release of several drugs.

1.4.1. The Specific Objectives:

1. Synthesis and characterization of SCPC, β-Rhenanite (Rhe) and α-Cristobalite (Cris).
2. Analyze drug binding to and release from these ceramics for Cisplatin (Cis) and Vancomycin (Vanc).
3. Correlate between the physic-chemical characteristics of each ceramic and drug binding and release kinetics.
4. Demonstration of the therapeutic effect of the SCPC-drug hybrid in vivo.

CHAPTER 2: SYNTHESIS OF BIOCERAMICS FOR DRUG DELIVERY AND CHARACTERIZATION TECHNIQUES

2.1. Introduction

Crystalline phases β-Rhenanite (Rhe) and α-Cristobalite (Cris) have been reported as the primary constituents of resorbable silica calcium phosphate bioceramic (SCPC) [18, 292, 293]. It has been also demonstrated that variations in the ratio Cris/Rhe have a significant effect on the behavior of SCPC for bioactivity, resorbability, and drug delivery properties [293, 298, 301, 320]. Moreover, microstructural properties such as porosity and surface area, and mechanical properties such as compressive strength, have shown to be affected by the phases distribution as well [18, 294]. Therefore is of our major interest to investigate the properties of each phase separately, and the role that they represent when combined in SCPC.

β-Rhenanite (β-$NaCaPO_4$), is an alkali calcium orthophosphate, with similar bioactivity than HAp, but with the advantage of higher dissolution rate in physiological conditions [321]. Ramselaar et al., reported in vivo resorption rates β-TCP<Rhe<HAp, and found that Rhe transform into apatite containing carbonate, sodium and magnesium, when inserted in tooth sockets of beagle dogs for 6 month [322, 323]. The ionic dissolution of Rhe might result in a stimulatory effect for cellular response. Knabe et al., reported higher proliferation and expression from human bone-derived cells incubated with Rhe than those incubated with β-TCP, suggesting Rhe superior potency to enhance osteogenesis [324, 325].

Various researchers have showed the enhancement effect of silica on the biological activity of calcium phosphates in vivo and in vitro [326, 327]. α-Cristobalite (SiO_2), is a crystalline polymorph of silica, formed by tetrahedrons of four oxygen around one silicon atom piled up in layers rotated 45^{o}about [100]and [010] axes [328]. As all crystalline forms of SiO_2, Cris reactivity is very limited. However, several studies testing silica-calcium phosphate biocomposites, have showed Cris as one of the phases present in the composites, without reporting negative effects due to the presence of the ceramic [329-331]. In fact, previous results suggest that increasing the amount of silica phase in SCPC higher cells response and degradability can be achieved [293, 298].

This section describes the procedures used to synthesize Cris, Rhe, and SCPC50, the characterization techniques utilized to analyze the microstructure, and the in vitro bioactivity of the ceramics under physiological conditions.

2.2. Materials and Methods

2.2.1. Ceramics Preparation:

Resorbable silica-calcium phosphate (SCPC50) containing a molar composition 36.8% CaO, 18.4% P_2O_5, 22.3% Na_2O, and 22.4% SiO_2 was prepared by mixing and sintering homogeneous stoichiometric mixtures of sodium silicate and dicalcium phosphate (Sigma-Aldrich, St Louis, MO) at 850^{o}C for 2h in air. β-Rhenanite, $NaCaPO_4$, was prepared by heat treating the mixture Na_2CO_3/$CaHPO_4$ (reagents from Sigma-Aldrich, St Louis, MO), with molar ratio fixed at 0.5, at 1100 ^{o}C for 32h in air [332]. In order to prepare α-Cristobalite, SiO_2, α-quartz powder (Gelest INC, Mooresville, PA) was mixed with deionized water to prepare a paste, molded in 50 mL cylindrical molds

and dehydrated at 120 ^{o}C overnight. Cylindrical bricks of silica quartz were then treated at 1500 ^{o}C for 5h in air. All samples were left to cool down inside the furnace.

Ceramics were manually ground using agate mortar, and then sifted through stack of ASTM of sieves, with decreasing mesh size. The efficiency of the method was evaluated by calculating the weight percentage obtained on each size interval. Particle sizes in the range 250-425 μm were selected for further drug delivery tests because they provide a suitable 3D interconnected porous structure, and high surface. After sifting, small particles, weakly attached to the granules, were cleaned by ultrasonication bath in deionized (DI) water. SEM analysis of the particles before and after the washing was performed.

2.2.2. Structure Analyses

The crystalline phases of each bioceramic were identified by X-ray diffraction analysis using X'pert PRO diffractometer (PANalytical, Westborough, MA) with CuKα (λ=1.54059 Å) radiation at room temperature, 45KV and 40mA. Continuous data were collected over the 2-theta range of 15-55^{o}, with a step size of 0.02^{o} and 1s time per step. The diffraction patterns were compared with standards JCPDs PDF cards. Crystalline phase quantification and lattice parameters were calculated by Rietveld refinement analysis, using the program X'Pert HighScore Plus. Pseudo-Voigt function was used to fit the diffraction peaks. Crystallite size was calculated using the half width of the diffraction peaks as a function of 2θ evaluated by the formulation of the Cagliotti model. Good quality of the Rietveld refinement was obtained when statistical R factors were lower than 10 units [333]. The indices of crystallinity (χ_c) for each ceramic were calculated as the ratio between the crystalline diffraction area (A_c) over the total area (A_t)

of the respective diffraction pattern profile ($\chi_c = A_c/A_t$). The morphology of the samples was analyzed by Scanning Electron Microscopy (SEM Model JEOL JSM-6480) equipped with an Energy Disperse X-ray (EDX) probe, to evaluate micro and macro structure. Samples were dehydrated and coated with a fine layer of gold (10nm) for SEM observations. The coating was performed in a sputter coater (Denton Desk IV Sputter) which uses argon gas and a small electric field. The sample was placed in a small chamber under vacuum. Argon gas was then introduced and an electric field was used to cause an electron to be removed from the argon atoms making the atoms ions positively charged.

2.2.3. Surface Chemistry

Ceramics particles were analyzed using Fourier transformed infra-red spectroscopy (FTIR) in the smart diffuse reflectance mode, employing Nicolet 6700 spectrometer (ThermoNicolet, Madison, WI) equipped with triglysine sulfate (DTGS) detector. Different samples were diluted at 95% in KBr matrix (Sigma-Aldrich, St Louis, MO) previously dehydrated at 100^{o}C. Background spectrum was recorded with pure KBr. All KBr spectra were acquired in the wavenumber range 400-4000 cm^{-1} at a resolution of 2 cm^{-1} after 200 scans.

2.2.4. Materials Dissolution Analysis:

Three replicates (200.0 mg) of each ceramic (n=3) were immersed separately in 10 ml of PBS (nominal pH 7.4) on an orbital shaker at 120 rpm and 37 °C. At sequential time, 4, 12, 24, and 96 h, aliquot (1 mL) of the sample was withdrawn from the immersing solution. At every sampling time, an equal volume of fresh PBS was added to maintain a constant (10 mL) total volume of release media. The Na, Ca, P, and Si ionic

concentrations of the 10X diluted solutions collected for the measurement of released drug were analyzed using ICP-OES at wavelengths of 315.887 nm, 213.62 nm and 251.611 nm respectively using radial plasma view. A pH meter, model UB10 W/ Deluxe Kit Denver Instrument, was used to determine the pH values of solutions at each time point. The pH meter electrode was calibrated at each required time point using buffer solutions. The buffer solutions were supplied by VWR International with a precision of ±0.01for pH 4.00 and 7.00 and ±0.02 for pH 10.00.

2.2.5. Surface Transformation:

The ability of apatite to form on ceramics surface when immersed in a simulated body fluid (SBF), with ion concentrations nearly equal to those of human blood plasma, was tested [334, 335]. Ceramic particles were soaked in SBF, at a ceramic to solution volume ratio of 33mg/ml for 1 month, at 37°C. Material surface was observed using SEM and subjected to FTIR analysis to confirm the presence of apatite layer.

2.2.6. Porosity and Surface Area

Pore size distribution and porosity percentage of the particles were determined using the mercury intrusion porosimetry technique with an AutoPore IV 9500 V1.07 scanning mercury porosimeter (Micromiretics, GA). The specific surface area was determined by BET single point using a high-speed N_2 gas sorption analyzer (TriStar II 3020 V1.03, Micromiretics, GA).

2.2.7. Statistical Analyses

The data were expressed as the mean ± SD. Statistical analyses were performed using the software OriginPro 8 SR1 v8.0773 (OriginLab Corporation, Northampton, USA). One-way ANOVAwas used to test for variance among more than one independent

groups of data. Two-way ANOVA with replication was used when more than two factors affected the measurement (e.g., material and sampling time). Differences among treatment groups were evaluated using Tukey post-hoc testing. Results were considered to have statistical significance difference at the 0.05 level.

2.3. Results

Particle size distribution (% w/w) caused by grinding and sifting resulted in different distributions for each ceramic. Comparable mass (~30%) were found in the particle size ranges from 250-425, 150-250 and 90-150 µm for Cris, with just about 5.65% of the total mass with size finer than 90 µm. Particle size distribution for Rhe resulted in~8.6% of the particles in the size range from 250-425µm, 10.2% in the range 150-250µm, 21.6 % in the size range 90-150 µm, and about 59.6% < 90 µm. SCPC50 showed a high fraction of particles in the size range 250-425 µm (38.2 %), comparable fractions for the ranges 150-250 and 90-150 µm (~22%), and 16.4% for particles <90 µm. Therefore, grounding and sifting efficiency varies from ceramics to ceramic, as well as to the desired particle size. The processing efficiency to produce particles in the size range 250-425µm was measured to be from larger to lower SCPC50> Cris >Rhe (Figure 2.1).

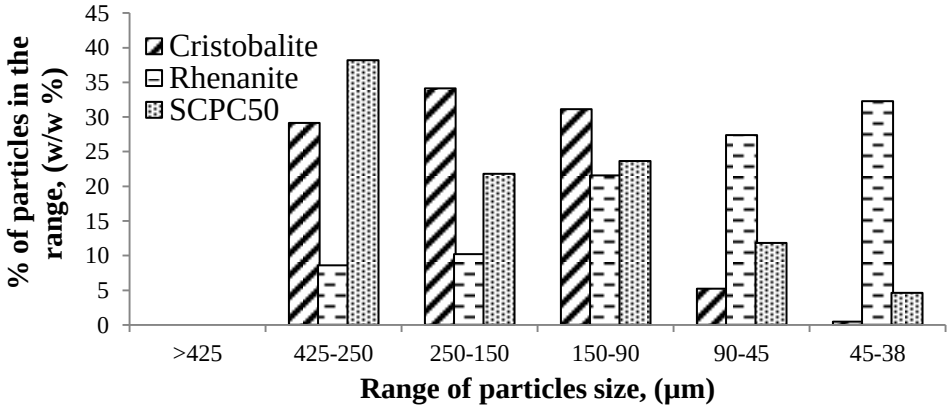

Figure 2.1: shows the particle size distribution obtained for the four ceramics. Bar chart showed that manual grounding of ceramic particles allowed recovering 24-39% of the total mass in the particle size 250-425 µm.

SEM analysis showed porous microstructure of the three ceramics with nanoparticles attached on their surface. After ultrasonication bath in DI water weakly attached nanoparticles were removed from Rhe and SCPC50, exposing the true porosity and surface area of the ceramic granules (Figure 2.2). This resulted significant since the nanoparticles weakly attached to the ceramics can significantly affect the porosity and surface area measurements. Cris samples before and after the washing step did not show noticeable differences between them.

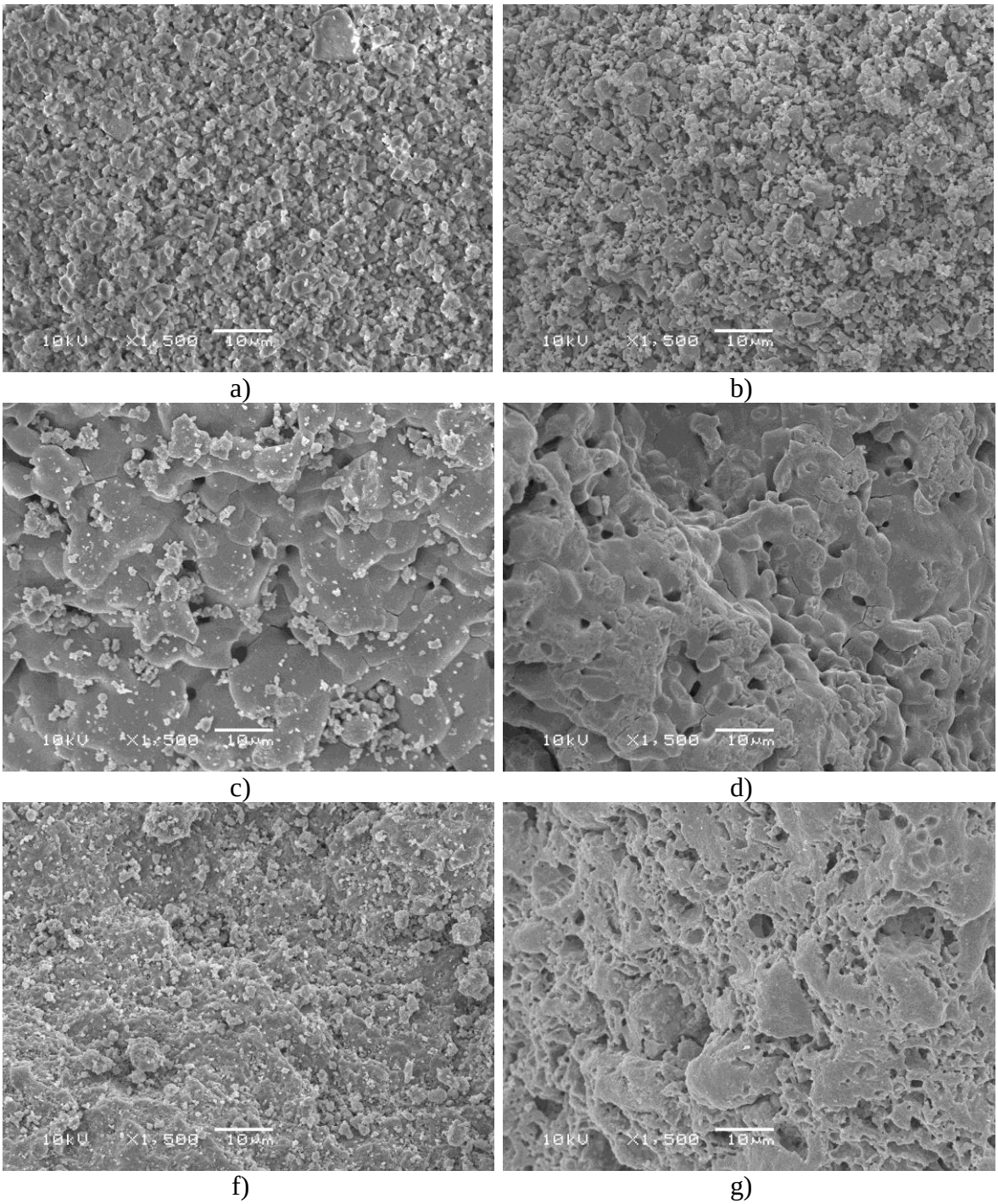

Figure 2.2: SEM micrographs for the different ceramics before and after the washing step by ultrasonication bath in DI water. The micrographs corresponds to a) Cris-before, b) Cris-after; c) Rhe-before, d) Rhe-after; e) SCPC50-before and f) SCPC50-after. Rhe and SCPC50 samples showed a much cleaner surface after sonication while no major changes were observed for Cris sample.

Mercury intrusion porosimetry demonstrated total porosity of 64.32% for Cris, 61.05% for Rhe and 52.40% for SCPC50. Cumulative porosity and pore size distribution analysis (Figure 2.3) reveal clear differences in the porous structure for all the samples. Cris sample showed 0.98% of pores below 2µm, about 23.6% of their pores in the size range between 5.0-0.2 µm, and 75.33 % between 60.0-350.0 µm.

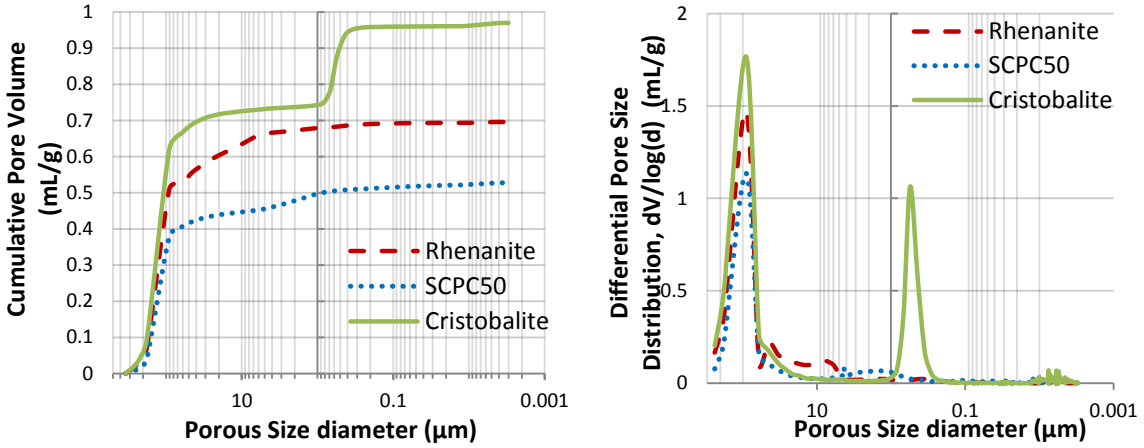

a) b)

Figure 2.3: a) Cumulative intrusion volume curve and d) differential porous size distribution for Rhe, Cris and SCPC50.

Table 2.1: The pore size distribution as a percentage of total porosity for Rhe, Cris and SCPC50.

Pore Radii range(µm)	Rhe		Cris		SCPC50	
	Absolute porosity (mL/g)	% of total porosity	Absolute porosity (mL/g)	% of total porosity	Absolute porosity (mL/g)	% of total porosity
below 0.2	0.00	0.34	0.01	0.98	0.01	1.31
0.2-1	0.02	2.16	0.22	22.51	0.02	4.70
1-5	0.03	2.24	0.23	1.13	0.07	7.78
5-60	0.13	19.3	0.06	6.59	0.05	9.09
60-350	0.53	75.98	0.67	68.74	0.41	77.06

Porosity percentages in the same size range for SCPC50 sample were 1.32%, 12.48% and 86.15% and for Rhe 0.34%, 4.4% and 95.28%, respectively. A more detailed pore size distribution is summarized in Table 2.1. Measurements of BET specific surface areas agree with the pore size distributions where Cris with higher amount of porous in

the nanosize showed the largest surface area (1.2608 m^2/g), followed by SCPC50 (0.8926 m^2/g) and then Rhe (0.4000 m^2/g).

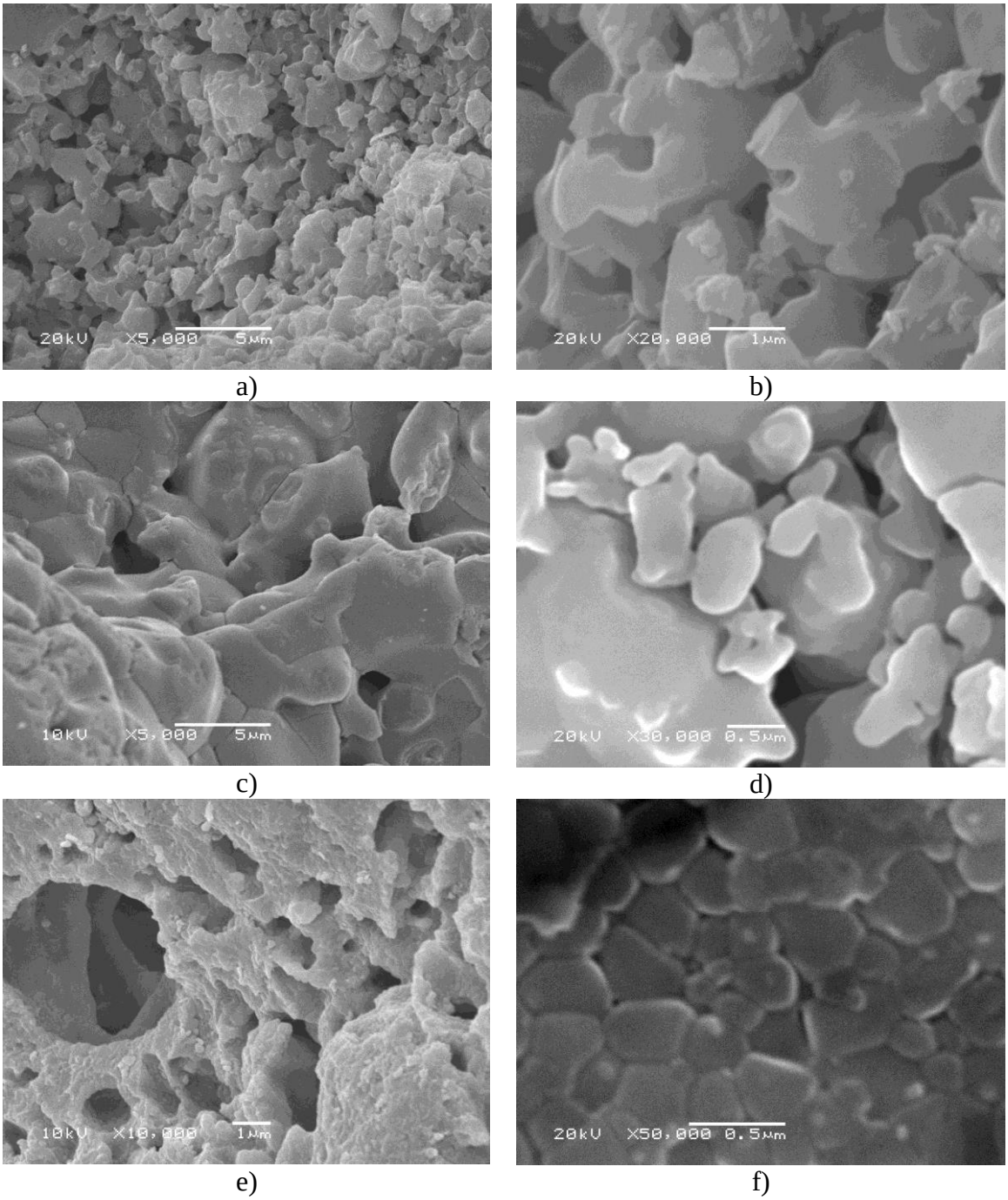

Figure 2.4: Typical SEM images of Cris [a) low and b) high magnification], Rhe [c) low and b) high magnification], and SCPC50 [e) low and f) high magnification]. Dense fused particles can be seen for all ceramics, entrapping 3D hierarchical micro-nano porous structure.

SEM images (Figure 2.4) revealed well fused particles entrapping through and blind pores in a wide range of porous size for all the samples. Pore with size <500nm were seen for all the samples. Polycrystalline grains, as confirmed by XRD, were observed in the size range 200-1000nm, 100-2000nm and 50-500 nm for Cris, Rhe and SCPC50 respectively. Nanopores and nano cracks were observed in the inter-granular and triple junctions of the polycrystalline grains for the different ceramic matrices. Similar equiaxial growth of the polycrystalline grains was observed in all ceramics.

Figure 2.5 displays the XRD spectra with the main crystalline phases of the different ceramics. The refined XRD patterns for is represented by the blue lines in the spectra. The difference between experimental and calculated spectra is depicted below each X-ray diffraction pattern. Cris was composed of α-Cristobalite (PDF card #39-1425) and α-quartz (PDF card #01-0649). Rhe sample showed 100% of β-Rhenanite (PDF card #29-1193). SCPC50 revealed to be composed of β-Rhenanite, α-Cristobalite and α-quartz. Figure 2.5: (Continued).

Table 2.2 reports the calculated wt% of the phase compositions for all the powders after refinement. Furthermore, differences in the calculated lattice parameters of α-Cristobalite, α-quartz and β-Rhenanite in SCPC50 with respect to the α-Cristobalite, α-quartz and β-Rhenanite in the Cris and Rhe samples were observed, indicating deformations in the unitary cell of the crystals most probably due to atomic substitutions in the SCPC50 phases. Statistical R factors obtained by Rietveld refinement were calculated < 10. This indicates good fitting between the experimental and the calculated patterns (Table 2.3).

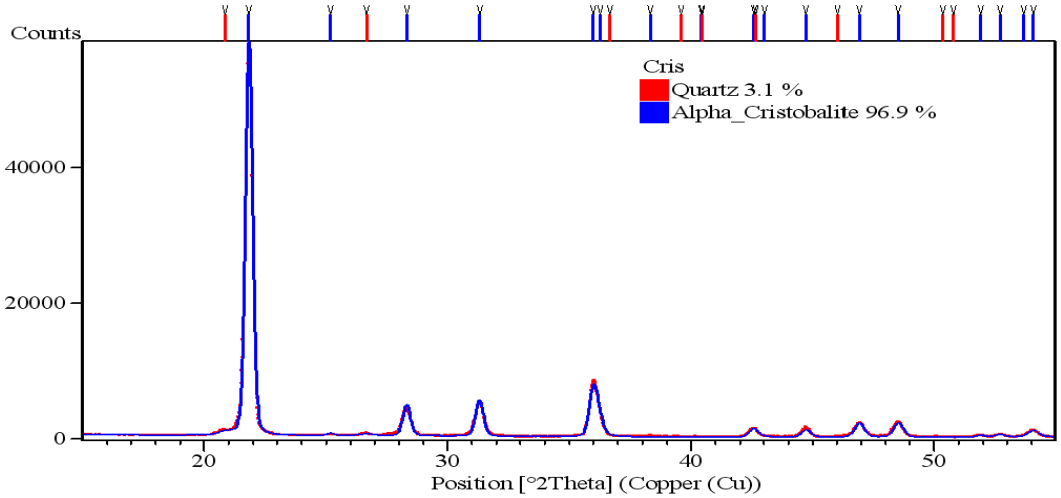

a)

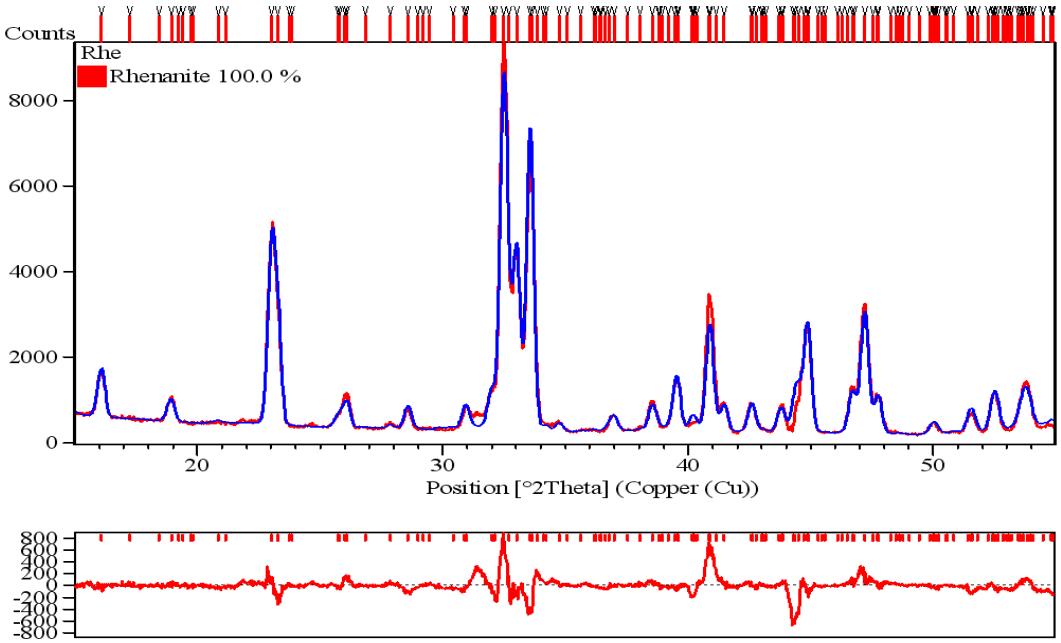

b)

Figure 2.5: XRD patterns taken from a) Cris, b) Rhe and c) SCPC50

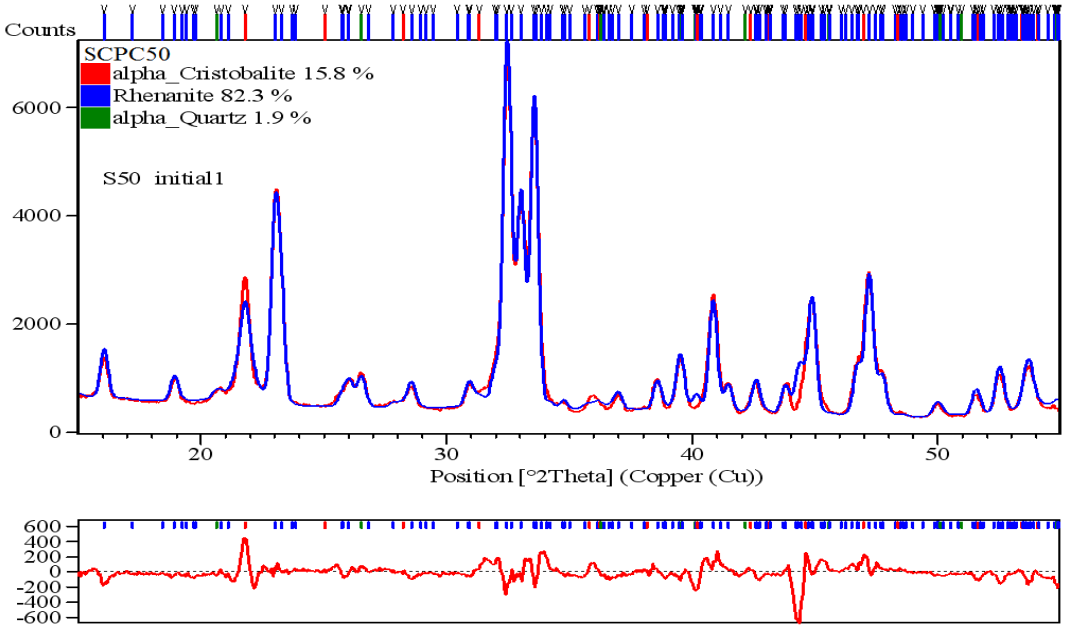

c)

Figure 2.5: (Continued).

Table 2.2: Phase composition and structural parameters of Cris, Rhe and SCPC50 obtained by Rietveld refinement on the corresponding XRD diffraction patterns.

Sample	Crystallinity (%)	Crystalline Phases Content (%)	Crystallite Size (Å)	Space Group(ICSD)	Lattice parameters (Å)			Volume ($Å^3$)
					a	b	c	
Cris	100.00	96.6% α-Cristobalite	275.6	P41212	4.9644	4.9644	6.9234	170.632
		3.1% α-Quartz	211.6	P3121	4.8748	4.8748	5.3727	110.570
Rhe	100.00	100% β-Rhenanite	239.7	Pna21	20.3674	9.1515	5.3981	1006.17
SCPC50	88.63	15.8% α-Cristobalite	150.7	P41212	4.9903	4.9903	6.8975	171.767
		1.9% α-Quartz	295	P3121	4.9286	4.9286	5.3536	112.622
		82.3% β-Rhenanite	253.6	Pna21	20.3898	9.147	5.3919	1005.63

Table 2.3: Refinement results from Rietveld modeling with a Voigt line profile for the diffraction data from Cris, Rhe and SCPC50 samples.

Sample	Rietveld statistical R factors			
	$\%R_{weighed\ profile}$	$\%R_{profile}$	$\%R_{expected}$	$R_{goodness\ of\ fit}$
Cris	8.64	5.93	2.79	9.51
Rhe	9.56	7.65	3.48	8.49
SCPC50	9.01	6.62	3.31	7.41

ICP measurements of the elemental dissolution of Cris, Rhe and SCPC50 showed significant differences in the elution of: Ca from Rhe and SCPC50 during all time points, Na from Rhe and SCPC50 at time points 24h and 96h, P from Rhe at time points 4h and 96h, and SCPC50 at time points 12h and 96h, and Si from SCPC50 for all time points. Elemental concentration of P and Na at time point 96h where comparable and between 1.4-1.6 fold that found in PBS control. On the other hand Si concentration showed a continuous increase from SCPC50 sample in comparison with all other groups and control. These elements are most probably released in their ionic forms: Na^{+}, PO_4^{-3} and SiO_4^{-4}. Negative ions are able to interact with protons in the aqueous solution increasing the total alkalinity of the solution. This explain the observed in Figure 2.6, where the pH of the PBS incubated with SCPC50 increases progressively and significantly higher in comparison with the control PBS, PBS incubated with Cris, and PBS incubated with Rhe.

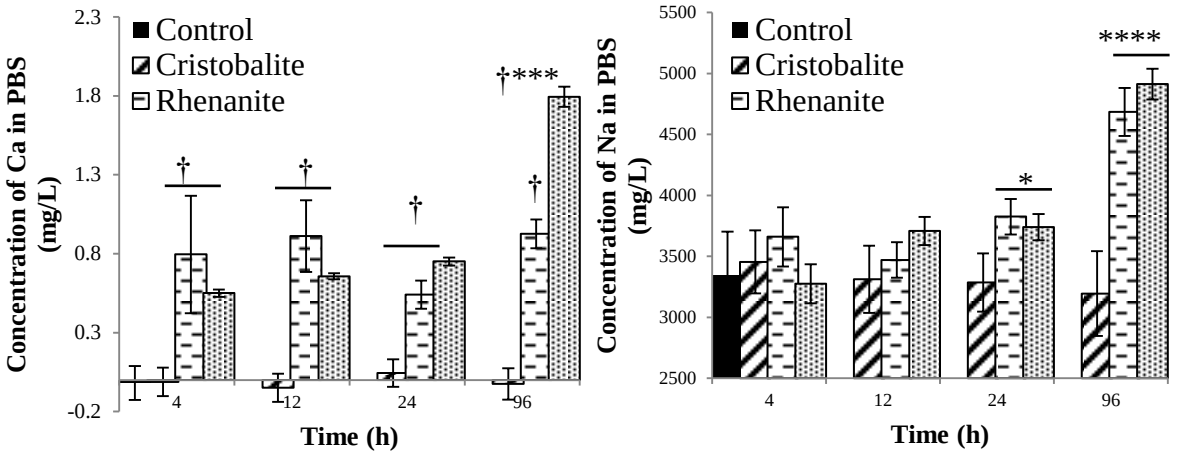

a) b)

Figure 2.6: dissolution kinetics of a) Ca, b) Na, c) P and d) Si; and pH change of PBS incubated separately with Cris, Rhe and SCPC50. Symbols † and * indicates that the means different is significant with respect to control PBS (*$p<0.05$, **$p<0.01$, ***$p<10^{-3}$, ****$p<10^{-4}$, †$p<10^{-5}$, †*$<10^{-6}$, and so forth). Control sample corresponds to the concentrations of Ca, Na, P or Si measured in the stock PBS.

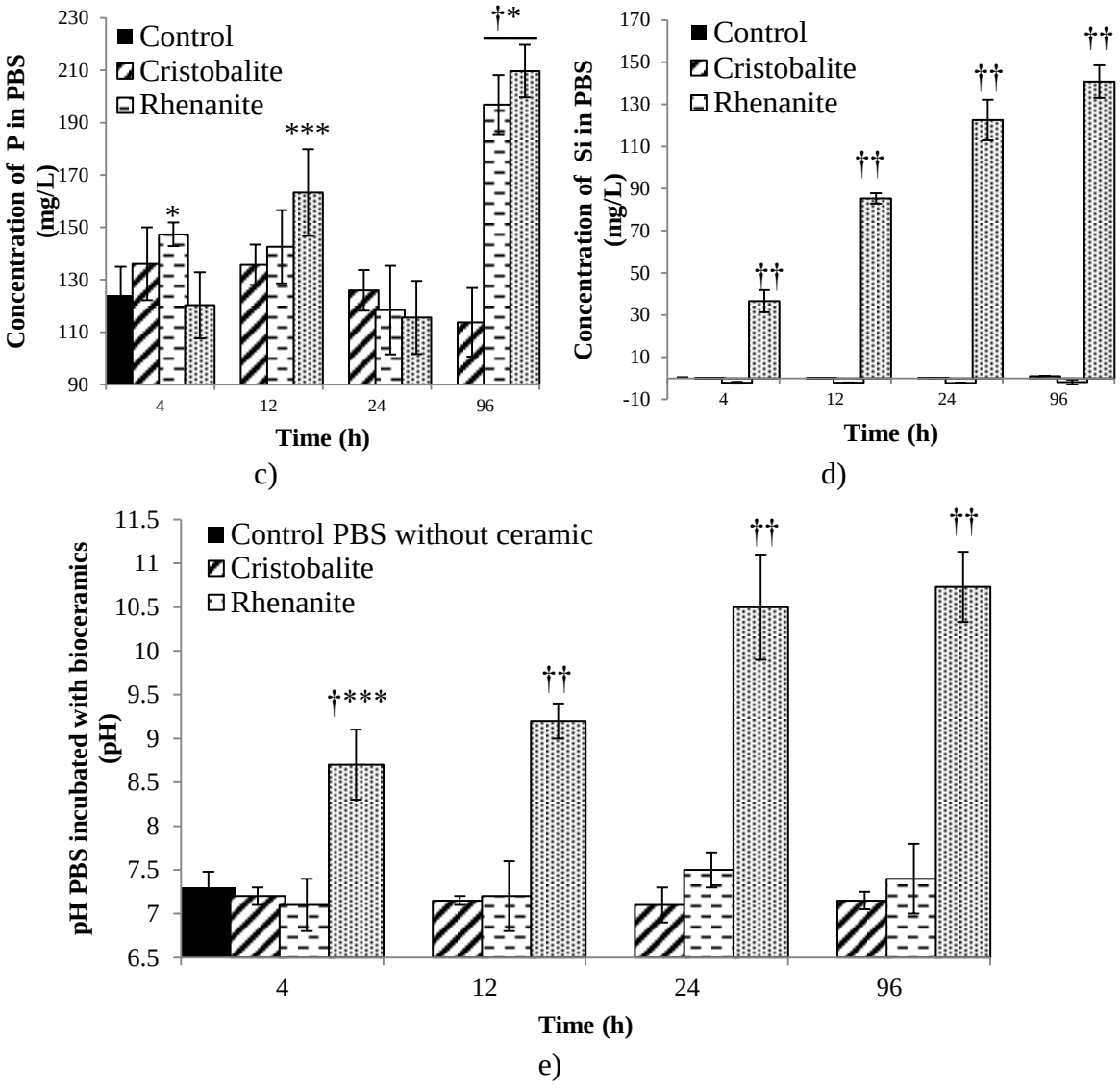

Figure 2.6: (Continued).

FTIR analyses of ceramics in the conditions: as sintered, and after immersion in SBF for 24 hours, is showed in Figure 2.7. Moreover, Table 2.4 depicts the main vibrations found on the Cris, Rhe and SCPC50 samples, and their correspondent assignments.

Cristobalite: characteristic peaks of Cris were detected within the range between 1200-400 cm^{-1}: Bending vibration (δ) Si-O-Si at 496.5 cm^{-1}, Cristobalite lattice structure vibration at 621.4 cm^{-1}, symmetric stretching (sν Si-O-Si at 798.5 cm^{-1}, stretching (ν)Si-

OH at 955.9 cm^{-1} and asymmetric stretching (aν) Si-O-Si 1196.3-1073.5cm^{-1}. In the region between 2500-1400 cm^{-1}, some overtones and compositions bands were noticed. In addition, hydroxyl band centered at ~3622.1 cm^{-1}, molecular water band at 1617.4 cm^{-1}, lonely Si-OH group at 3738.2 cm^{-1} and broad hydroxyl band at 3324.5 cm^{-1} respectively, were observed. Increased intensity of the bands of the hydrated groups of Cris was observed after the immersion in SBF for 24 h, indicating hydration of the ceramic surface without the appearance of an apatite layer (Figure 2.7a).

Rhenanite: fingerprint region of the unloaded Rhe sample showed the following peaks: asymmetric bending (aδ) P-O-P 610-520 cm^{-1}, sν PO at 962.0 cm^{-1}, aν PO between 1100-1000 cm^{-1}, $PO^{(-)}$ ionic group 1123-1117 cm^{-1} and P=O 1164 cm^{-1}. In addition, bands at 800.0 cm^{-1} and 2919 and 2849.6 cm^{-1}corresponding to P-OH were also noticed. Overtones and composition peaks were also seen in the range 1400-2500 cm^{-1}. Molecular water band was detected at 1613.7 cm^{-1} and a broad hydroxyl band centered at ~3293.4 cm^{-1}. After immersion in SBF characteristics bands of carbonate HAp at 3568 cm^{-1} (OH), 1567 cm^{-1} (C=O), and 605 cm^{-1}(P-O) were observed (Figure 2.7b).

SCPC50: as expected, SCPC50 sample showed peaks corresponding to its two major phases (Rhe and Cris). The location of the peaks in the range between 400-1200 cm^{-1} was: δ-Si-O-Si at 485.7 cm^{-1}, aδ P-O-P at 610-550 cm^{-1}, vibration from Cristobalite lattice structure at 620.6 cm^{-1}, sν Si-O-Si at 800.0 cm^{-1}, sν PO at 962.3 cm^{-1}, aν PO between 1100-1000 cm^{-1}, aν Si-O-Si 1200-1100.0 cm^{-1} and P=O at 1200.1 cm^{-1}. In addition, characteristics bands of immature carbonate hydroxyapatite were observed at: ν OH centered at ~3622.1 cm^{-1}, molecular water 1613.2cm^{-1}, and surface carbonate ions aν C=O at 1671.9 cm^{-1}. Lonely Si-OH group at 3737.4 cm^{-1}, broad band at 3299.6 cm^{-1}

corresponding to the hydroxyl group and P-OH bands at 2920.3 and 2850.4 cm^{-1} were also noticed. FTIR analysis suggested the apatite structure on SCPC50 due to the increase in the intensity of P-O bands together with the decrease in the intensity of Si-O bands after soaking in SBF (Figure 2.7c).Presence of immature apatite layer on the top of the ceramic particles was observed by SEM (Figure 2.8).

Table 2.4: Main Vibration Modes of Cris, Rhe and SCPC50 (FTIR Spectroscopy). The bands assignments are according to literature data.

Characteristic bands	Wavelength (cm^{-1})			
	Cristobalite	Rhenanite	SCPC50	Assignment
δ-Si-O-Si	496.5		485.7	460 [336]
aδ P-O-P		520-610	550-610	500-560 [337]
P-O(H) bending mode		565.9	567.5	565 [338]
Inter-tetrahedral vibrations for low-cristobalite	621.4		620.6	620 [339]
sυ Si-O-Si	798.5		797.2	798.5, 1025, 1050 [340]
υ P-OH		800		795 [341]
υ Si-OH	955.9			950 [336]
sυ P-O		962.0	961.7	962 [340]
PO_4^{-3} ionic group		1013.4	1010.2	1015 [340]
aυ P-O	1073.5, 1115.8, 1196.3	1025.1, 1051.7, 1075.7, 1087.6	1027, 1050.2, 1074.5, 1079.5	1000-1100 [340]
aυ Si-O-Si			1145.3, 1197.2	1120-1162 [295]
PO^- ionic group		1117-1123	1115.8	1122 [340]
P=O		1164	1201.0	1250-1150 [337]
In plane δ P-OH		1448.3		1450 [341]
OH bending	1617.4	1613.4	1613.2	1660-1600 [340]
C=O stretching		1657.0	1671.9	1650-1680 [342]
P-O-H stretching		2919, 2849.6	2920.3, 2850.4	2300-3200 [341]
H bounded Si-OH	3324.5			3438 broad [337]
free H_2O stretching or OH ions	3622.1	3670	3622.1	3600-3400 very broad [340]
Lone-silanol, stretching Si-OH	3738.2		3737.4	3738 [343]

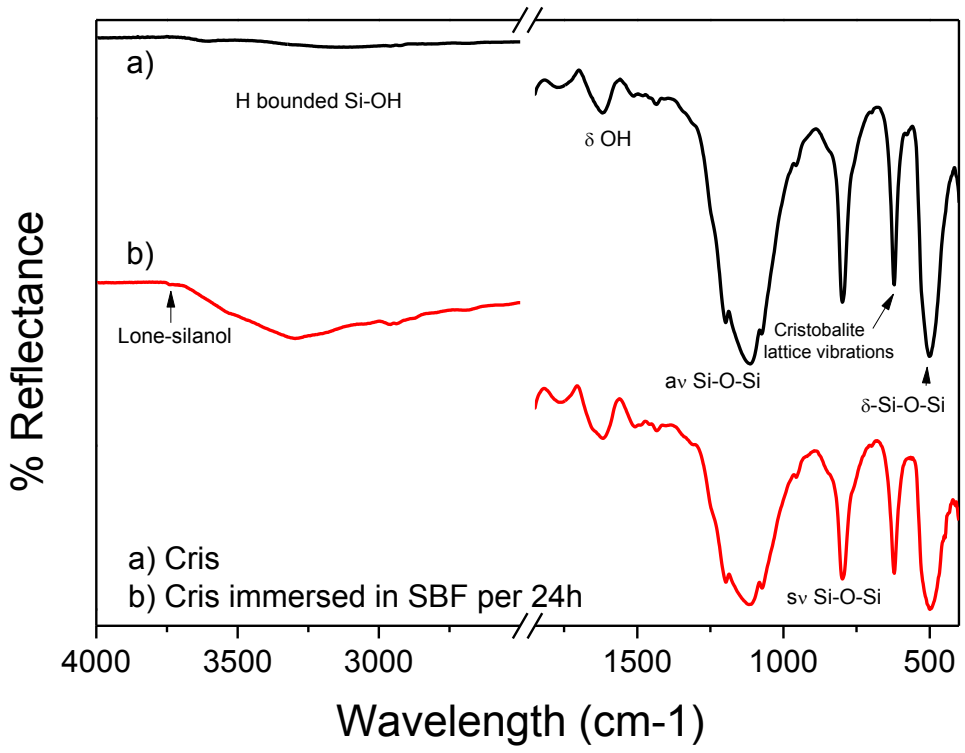

a)

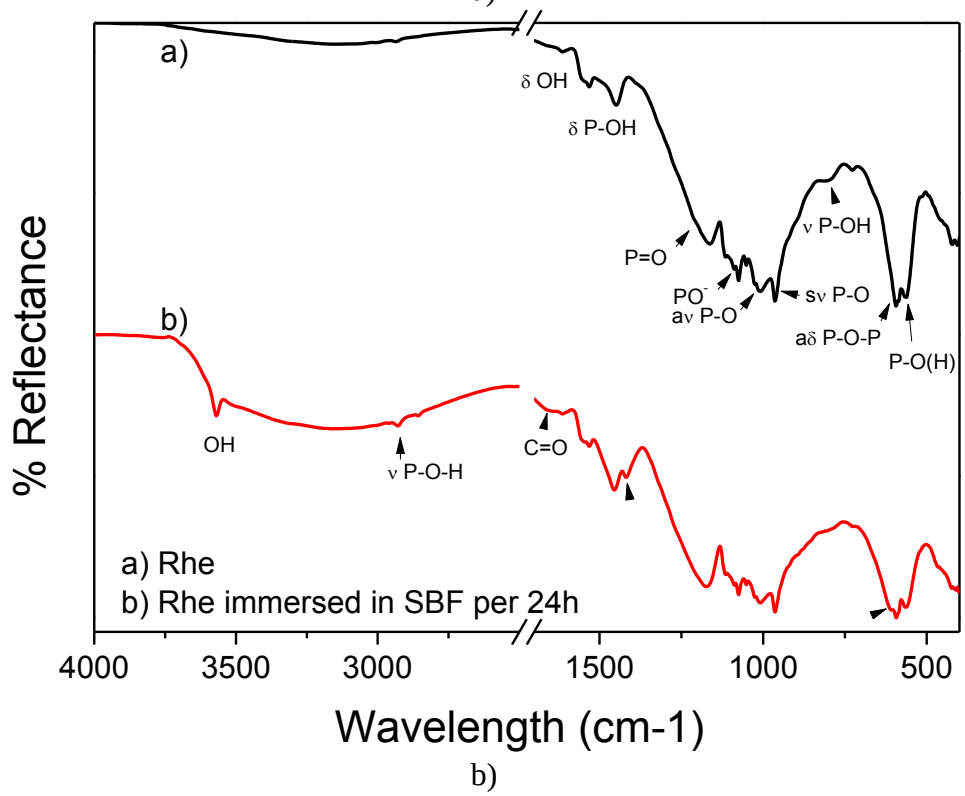

b)

Figure 2.7: FTIR spectra of a) Cris, b) Rhe, and c) SCPC50, before and after soaking in simulated body fluid (SBF) for 24 h at 37oC.

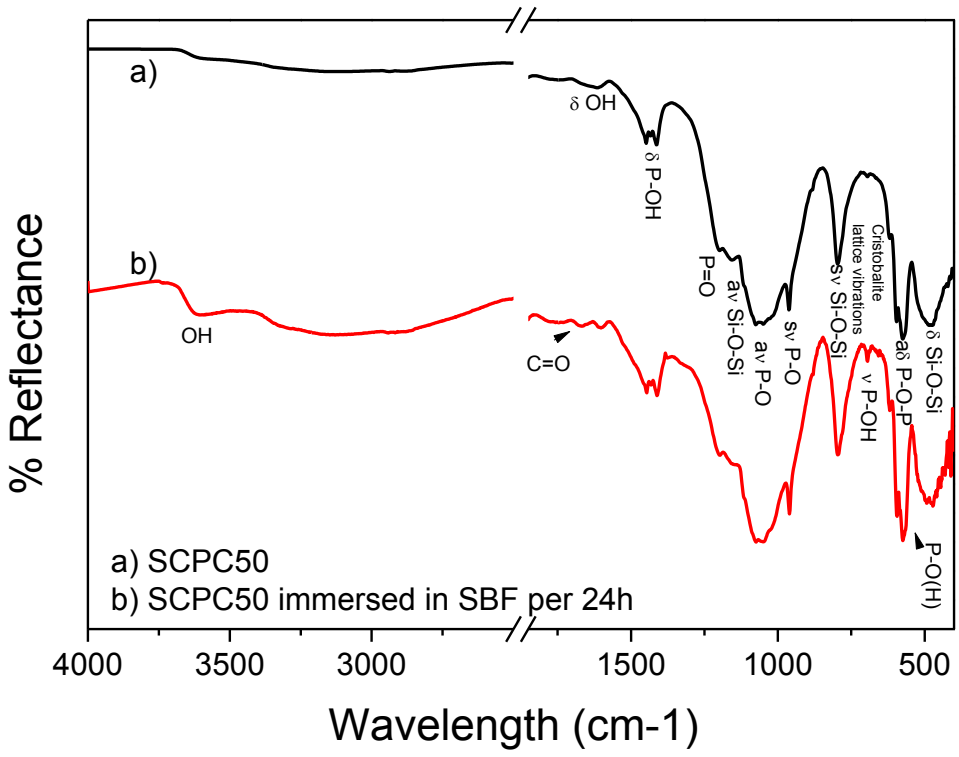

c)

Figure 2.7: (Continued)

To minimize the increase in the pH of the PBS incubated with SCPC50 during drug loading or release, SCPC50 granules were soaked in simulated body fluid (SBF) in 33 mg/ml, ceramic/SBF ratio, for 24 hours at 37°C. Particles were collected and dried at 37°C for 24 hours and used for drug loading and subsequent release.

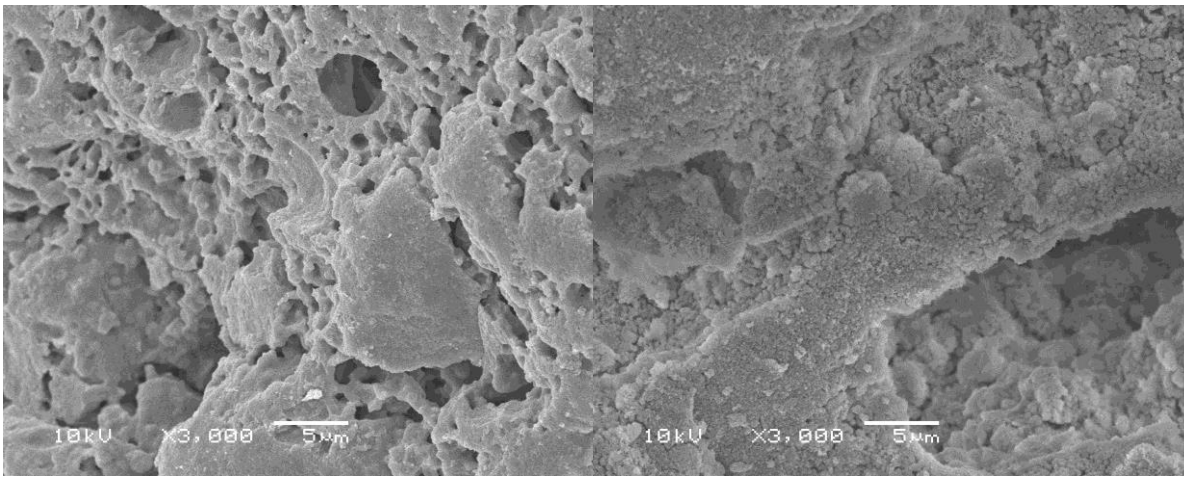

a) b)

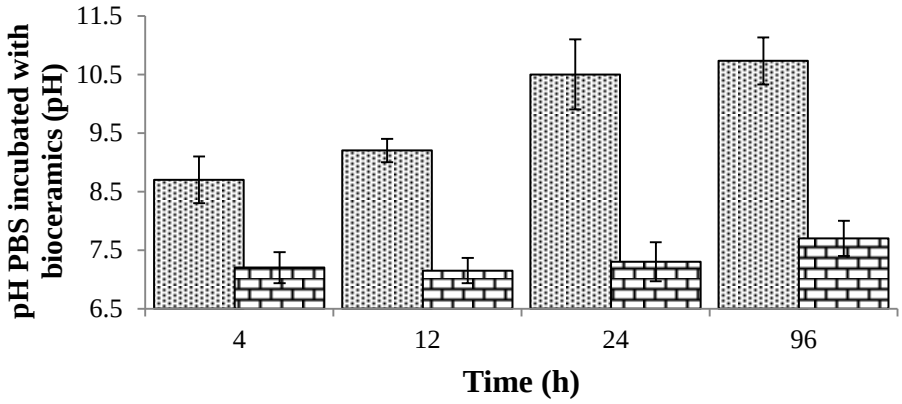

c)

Figure 2.8: SCPC50 a) before and b) after immersion in SBF solution for 24h. The bar chart (c) shows pH change of PBS incubated with SCPC50 and SCPC50 pre-immersed in SBF for 24h.

2.4. Discussion

Desired composition of three different ceramics, Cris, Rhe, and SCPC50 were successfully achieved by thermal treatments and corroborated by microstructure characterization. The efficiencies of the process to generate particles in the size 250-425 µm for the three ceramics were 40% for SCPC50, 30% for Cris and 9% for Rhe. Furthermore, the dissolution and bioactivity of the three different carriers were evaluated

in vitro. XRD analyses confirmed the presence of crystalline α-cristobalite and β-rhenanite in Cris, Rhe and SCPC50 ceramics respectively. BET, mercury intrusion, and SEM analyses demonstrated the high hierarchical interconnected porosity for the ceramic particles with pores in the nano and micro sizes. Results also showed that the pore size distribution has a direct effect on the ceramic surface area. Cris with the highest number of nano pores showed significantly higher surface area than Rhe and SCPC50 samples. Stability of the materials showed to be affected by the microstructure of the ceramics, specifically the phase compositions. The high elution rate of negatively charged ions from SCPC50, most probably due to the dissolution of Si-rich amorphous phase [18], demonstrated significantly increasing the alkalinity of immersing physiological solutions. However, in vitro bioactivity tests showed SCPC50 and Rhe ability to form carbonate HAp layer on the surface of the ceramics particles after immersion in SBF for 24 h at 37^{o}C. On the contrary, high stability of Cris sample showed few changes when immersed in physiological conditions. Immersion of SCPC50 for 24 h in SBF before drug loading and release showed to help controlling the pH of PBS incubated with SCPC50 particles (Figure 2.8c).

Morphological analysis by SEM demonstrated that all ceramics are formed by small fuse polycrystalline particles. Inter-granular cracks were observed on Cris and Rhe samples. SCPC50 showed a fused interphase that serves as a smooth transition between two contiguous poly-crystals. Crack observed in Cris and Rhe samples are indicative of brittleness and low fracture toughness. XRD-Rietveld analysis showed crystallite size in the range between 150-300 Å, confirming the polycrystalline nature of the fused particles. These indicate that, besides the porosity, the three ceramics showed high

density of grain boundaries. As a consequence, crystal defects increases the free energy of the three materials and facilitates additional physical or chemical interactions. Moreover, hierarchical porous distribution was found for the three ceramics. Cris showed a binomial distribution with 68% of the pores centered on the size 90μm, and 24% on the size 500nm. About 77% of the pores of Rhe and SCPC50 was in the range >10μm, and 2.4% and 6.0% below 1μm. These porosities are suitable for tissue engineering and drug delivery applications.

XRD analyses showed that the total lattice volume of α-cristobalite and β-rhenanite in SCPC50 vary slightly with respect to those in Cris and Rhe samples, indicating cell deformation most probably caused by elemental solid substitutions. Substitution of Si for P (or vice versa) is feasible due to the proximity of their ionic radii, crystal structure, valence, and electronegativity as established by Hume-Rothery rules. These modifications of the lattice parameters decrease the thermodynamic stability of SCPC50 crystalline phases enhancing its bioactivity, and degradability [320]. Additionally, 11.37% SCPC50 was measured to be amorphous. TEM analysis carried out by Liu et. al., demonstrated that the amorphous component of SCPCs is a silica-rich phase [18]. Therefore, it is expected that the dissolution of this phase boost the Si measured from the immersing media (PBS). As a consequence, increasing in the pH can be explained by the accumulation of negatively charged poly-ions released in the saturated physiological solution during SCPC50 degradation, leading to the thermodynamically favorable reactions [344] described in Equation 2.1and Equation 2.2.

$$2SiO_4^{-4} + 8H_2O \rightarrow 2H_4SiO_4 + 8OH^- \qquad \text{Equation 2.1}$$

$$2H_4SiO_4 \rightarrow 2SiO_2 + 4H_2O \qquad \text{Equation 2.2}$$

FTIR analyses demonstrated the capacity of Rhe and SCPC50 samples to form a bioactive layer of carbonated hydroxyapatite-like surface upon immersion in SBF. ON the other hand, Cris showed to have negligible interactions under the same conditions. ICP analyses demonstrated that Cris dissolution is limited and, therefore, the low reactivity of the materials when immersed in body fluids. The rapid exchange of silicon, sodium and phosphate ions from Rhe and SCPC50 with the solution promoted the hydrations of the ceramics. This allows the back precipitation of Ca^{2+} and PO_4^{-3}on the various ceramic surfaces leading to the formation of an apatite layer as explained elsewhere [245]. It is well known that formation and maturation of CaP layer on the top of the ceramic surface reduce the leaching of ions. This result might help to control the increasing pH of the immersing solution incubated with SCPC50 [245].

2.5. Conclusion

Successful thermal treatments were achieved for the preparation of Cris, Rhe and SCPC50. Phase composition and crystallinity of the three ceramics showed to play an important role in the materials porosity and reactivity. Cris showed to be the most porous ceramic with a large amount of surface area generated by the superior number of nanopores compared to Rhe and SCPC50. Degradability properties of Rhe and SCPC50 facilitated chemical reaction when immersed in SBF that promoted the formation of CaP-like layer on the surface of the two ceramics. Rapid leaching of Si from SCPC50 showed significantly increasing the alkalinity of immersing buffer solution. The high stability of Cris was corroborated by the poor ceramic dissolution study and in vitro.

CHAPTER 3: CRISTOBALITE AND RHENANITE AS DRUG DELIVERY SYSTEMS FOR VANCOMYCIN AND CISPLATIN

3.1. Introduction

Drug delivery systems (DDS) have been tested to provide controlled release of highly potent drugs in a localized/targeted manner with minimal acute and chronic side effects. Biomaterials of all kinds have been tested as drug delivery system platforms. Different formats of polymers [307, 345, 346] and bioceramics [347, 348] such as nano-particles [349, 350], microparticles [351-353], gels [354, 355] and tablets [356, 357], have been investigated with various degrees of success. The use of microparticles and scaffolds as DDS overcomes the poor loading capacity and rapid release that most of the nano size DDSs offer [56, 118]. Most of the research coping with microparticles and scaffolds try to explain the ability of these devices for loading and release drugs based on their porosity [358-361], surface area[362, 363] and degradation rates [354, 362, 364]. However, little has been reported regarding the importance of the physic-chemical properties that regulate the adsorption and release of pharmaceutics from these biomaterials. Multiple examples can be found in the literature showing significant differences in the loading and release capacities of DDS from different drugs and the same carrier, or same drug and different biomaterials.

Shiho et.al., prepared hydroxyapatite nano particles (n-HAp) containing different concentrations of mercaptosuccinic acid (Mer) using hydrolysis. It was found that as the concentration of Mer increased, the specific surface area of HAp increased, and its

crystallinity decreased. Interestingly, the authors reported a decreased in the adsorption capacity of the Mer-HAp towards BSA in samples rich in Mer which have high specific surface area. The authors speculated that the decrease in the loading capacity was attributed to the high negative charges induced by the higher amount of Mer. However, it is also possible that increasing the Mer lowers the amount of surface Ca^{2+} available for BSA binding since BSA is a calcium binding protein. Furthermore, the atomic absorption data reported by Ishihara showed minimal changes in the Ca^{2+} content of different Mer-HAp samples. Although the surface area was analyzed, the pores size distribution was not reported. Considering the big molecular size of BSA (MW=67200) it is possible that porosity in the order of magnitude of angstroms and in the nano scale could contribute to the reduced loading capacity of the material. On the other hand, same Mer-HAp samples showed significantly higher adsorption of positive charged Cytochrome C protein as increasing the surface area and the Mer concentration. The interaction between the negatively charged carboxylate group of the Mer and the protein and the functional groups on the HAp surface was not analyzed.

Gautier et al., examinated the effect of surface area of different heat treated apatites on its capacity for loading and release human growth hormone hGH. As expected, the authors found enhanced drug loading capacity on the carrier with the highest specific surface area. Interestingly, no differences in the drug adsorption were measured among all the other samples, even when the difference between the lowest and highest surface area in the group was about 8-fold. The Authors suggested that the similarities in loading capacity could be attributed to differences in the porous size distribution of the carriers. Influences of different parameters such as the crystallinity,

phase composition, and possible drug bonding with the carrier's surface, were not addressed by the authors. Besides, drug release kinetic showed significant differences in the drug release half time that did not follow a clear trend with the specific surface area of the carriers. These clearly indicated that the drug release kinetics is not just controlled by the surface area but also by the surface chemistry and charge.

Recent publications by the group of Uskokovic, et al., tested various calcium phosphates (CAP) nanoparticles including monocalcium phosphate monohydrate (MCPM), dicalcium phosphate anhydrous (DCPA), amorphous calcium phosphate (ACP) and hydroxyapatite (HAp), for drug loading and release. Loading efficiency tests on HAp showed that the adsorption of BSA was about two orders of magnitude higher than that observed for fluorescein on HAp. This was explained due to the stronger attraction between positively charged sites on HAp, Ca^{2+}, and BSA protein, which allows more affinity between HAp and the protein than on fluorescein. Experimental evidence was not provided in this matter, and no further data with respect to the adsorption capacity of the other carriers were shown. In addition, authors found a correlation between the sustained release of BSA and fluorescein relatable to the degradation rates of the different CAP carriers. Moreover, they found a higher release rate of fluorescein at any time point and for all CAP phases tested than that found for BSA, explained by its weaker linkage to the carriers. The porosity, specific surface area, shapes and size of the nanoparticles were not analyzed.

Vancomycin (Vanc) is a clinically important amphotericgylcopeptide (short chain of amino acids that has sugar molecules attached to it) antibiotic [365]. This drug has been extensively used against serious infections caused by Gram-positive bacteria [366].

The mechanism of action of gylcopeptide antibiotics, including Vanc, is through the inhibition of the bacterial cell-wall synthesis achieved by binding to the C-terminal peptide sequence L-lysyl-D-alanyl-D-alanine in muco peptide precursor molecules [367]. Vanc exhibits a slow anti-bacterial activity with low minimum inhibitory concentration (MIC). Vanc is poorly absorbed from the gastrointestinal tract, requiring intravenous systemic administration that has been associated with severe adverse effects [368]. Therefore several attempts have been made to deliver Vanc using carrier vehicles to locally treat diseases in places with difficult irrigation, such as osteomyelitis [369, 370].

Cisplatin (Cis) chemotherapeutic agent commonly used for treatment of various kinds of cancer [371, 372]. Its antitumor activity is exerted by binding DNA via intrastrand cross-links to nucleoside component of DNA interfering with DNA replication and transcription, and causes cellular apoptosis [373]. Chronic usage of Cis can induces to cellular resistance by several possible mechanisms, including increased interactions with metallothionein and glutathione and increased DNA repair, which lowers the efficiency of the drug significantly [374]. Therefore, high doses of Cis are generally clinically administrated, causing many severe toxic side effects, such as gastrointestinal problems, ototoxicity, nephrotoxicity and visual abnormality [375, 376]. As such, mechanisms of delivering Cisplatin to the local environment of a tumor are under research [377, 378]

SCPC is a silica calcium phosphate composite mainly constituted by β-Rhenanite ($NaCaPO_4$) and α-Cristobalite (SiO_2) as dominant phases. This bioactive composite has shown enhanced resorption and significantly higher ability to adsorb serum proteins when compared with bioactive glasses in vivo [293]. Ning, et al., showed superior

sustained release of rhBMP-2 protein from SCPC when compared with porous hydroxyapatite [296]. Moreover, SCPC has demonstrated potential for loading and release of antibiotics, like Gentamicin [298] and Vancomycin [364] , and anticancer drugs, such as 5-FU [379] and Cisplatin [380]. The authors pointed out that the porosity distribution of SCPCs together with the chemical interactions taking place on the particle's surface allowed sustained release kinetics. Although numerous studies have been published on the use of silica-calcium-phosphates materials, the role of ceramic microstructure on drug binding and release is not fully understood. The goal of the present work is to analyze the role of SCPC phase composition on drug binding and release kinetics. We report on the synthesis and characterization of Cristobalite and Rhenanite, and investigate their ability to bind and release Vancomycin and Cisplatin. The effect of surface chemistry on drug binding was evaluated and correlated to the release kinetics and ceramic dissolution.

3.2. Materials and Methods

3.2.1. Materials Preparation

SCPC50 immersed in SBF for 24h, Rhe, and Cris ceramic particles, in the size range 250-425 µm, were used for drug release studies. Various ceramics were prepared as described in section 2.2.1.

3.2.2. Drug Loading

Vancomycin (Vanc) solution at a concentration of 8 mg/mL, was prepared by dissolving 320 mg Vancomycin hydrochloride (Sigma-Aldrich) in 40 mL of PBS using a magnetic stirrer for 24 h. Loading test was performed by immersing three replicates of 0.2g of each material (Cristobalite, Rhenanite and SCPC50) in 1.5 mL of Vanc solution.

After periods 1, 2, 4, 8, 16 and 24 h a 20 µL of the solution was withdraw, and the concentration of the drug was measured by HPLC [381]. Briefly, Vanc was separated on a ZORBAX Eclipse XDB-C18 HPLC column (4.6x150mm, 5µm). The mobile phase consisting of a mixture of A: 5mM KH2PO4, pH 6.4, and B: acetonitrile (CHROMASOL V gradient grade, ≥99.9%, Sigma-Aldrich, US), was delivered at a flow rate of 1.5 mL/min. The gradient program for the test was as follow: 0 and 1.5 min: 97% A, 3% B; 10 and 13.5 min: 80% A, 20% B; 14.5 and 16.5 min: 97% A, 3% B. The sample was diluted ten times in a solution 97% A, 3% B and the injection volume used was 50µL. Chromatograms were obtained using VWM detector at 282 nm wavelength. Standards known Vanc solutions over the range 8.0-0.04 mg/mL were used to create the calibration curve. Once define the optimum loading time (time at which all samples loaded the maximum amount of Vancomycin), 1.5 g of each powder was loaded by immersion in 8 mg/mL Vancomycin solution during this time. Simultaneously, Setaram Instrumentation, Sensys evo TG-DSC analyzer was used to determine the presence and the amount of drug loaded on each ceramic. The samples (~70 mg) were placed in an alumina crucible and heated in air at 2 ^{o}C min^{-1} to 800 ^{o}C. Control samples of Vancomycin or ceramic without drug were run in parallel for comparison. TG and DSC of the loaded particles were adjusted with respect to the unloaded ceramics. Areas under the peak in the DSC curves were calculated by Gaussian peak fitting and integration of the adjusted peaks using OriginPro 8.0.

All ceramic samples were loaded with Cis following the procedure reported earlier [300]. Briefly, Cisplatin (Cis, Cis-dichlorodiamineplatinum (II)) solution at a concentration 10 mg/ml was prepared by dissolving 500 mg of Cis in 50 mL of Dimethyl

sulfoxide (DMSO). 5 g of each ceramic sample was immersed separately in 15mL of Cis solution at 37^{o}C. After 42 h, loaded particles were separated from the solutions and left to dry inside chemical hood for 48 h. Control ceramic samples were treated with DMSO without Cis under the same experimental conditions. The total amount of Cisplatin loaded onto each ceramic was determined by consecutive washing steps of 80 mg of each drug-ceramic hybrids (four repetitions each, n=4) in 70% nitric acid. Aliquots were centrifuged at 5000xg for 3-min. The supernatant was collected and the concentration of Cis was determined by measuring the concentration of Pt using Inductively Coupled Plasma-Optical Emission Spectrometer (ICP-OES; Optima 3000, Perkins Elmer) at a wavelength of 265.945 nm in axial plasma view.

3.2.3. Surface Chemistry:

Drug loaded and unloaded samples were analyzed using Fourier transformed infra-red spectroscopy (FTIR) in the smart diffuse reflectance mode, employing Nicolet 6700 spectrometer (ThermoNicolet, Madison, WI) equipped with triglysine sulfate (DTGS) detector. Vancomycin and Cisplatin alone were also analyzed by FTIR for comparison. Spectra were acquired in the wavenumber range 400-4000 cm^{-1} at a resolution of 2 cm^{-1} after 200 scans.

3.2.4. Kinetics of Drug Release

The drug release kinetics from ceramics loaded with Vanc were analyzed under the same experimental conditions. Eight replicates of 0.2 g each of the Vancomycin loaded ceramic (n=8), and an equal number of Cis-loaded ceramic (n=8) were immersed separately in 10 ml of PBS (pH 7.4) on an orbital shaker at 120 rpm and 37 °C. At sequential time points of 2, 4, 8, 12, 24 h; and then every 24 h thereafter up to 144 h; and

then each 4 days up to 20 days (480 h) aliquot (1 mL) of the sample was withdrawn from the immersing solution. At each sampling time point, an equal volume of fresh PBS was added to maintain a constant (10 mL) total volume of release media. The aliquot was then centrifuged to 3000 rpm for 3 min at room temperature, and the supernatant was collected for drug concentrations measurements. Released Vanc concentrations were measured by HPLC, and those of Cis by measuring the Pt concentration using ICP-OES as described earlier. The cumulative percentage release was calculated as the ratio of the drug mass released at each time point to the total amount of drug initially loaded in the powders.

To analyze the in vitro release data, different kinetic models were used to describe the release kinetics. 1) Zero Order Release (systems with a constant drug release), 2) First Order Release (systems with a concentration dependent release rate), 3) Higuchi (systems with insoluble matrix where the release of drugs depends to the square root of time, based on Fickian diffusion) and 4) Hixson-Crowell cube root law (systems with surface area and diameter of particles or tablets changing during release of drug). The mechanism of drug release was calculated using Korsmeyer–Peppas model (also known as power law), fitting the first 80% of drug release data.

3.2.5. Dissolution Analysis:

The ionic concentrations of Ca, P and Si in the solutions collected for the measurement of released drug were analyzed using ICP-OES at wavelengths of 315.887 nm, 213.62 nm and 251.611 nm respectively using radial plasma view. Parallel experiments including PBS incubated with unloaded control ceramic under the same experimental conditions were performed.

3.2.6. In Vitro Cytotoxicity Tests

3.2.6.1. Vancomycin

The therapeutic effect of the released antibiotic was analyzed using the Kirby-Bauer assay. Briefly, inoculate Luria broth with Staphylococcus aureus were incubated overnight in 37^{o}C shaker. Incubated culture was centrifuge at 70 rpm for 10 minutes, pours off supernatant and re-suspended in 1 ml PBS. The amount of bacteria present was quantified using the spectrophotometer. Additional PBS was added to the culture in order to standardize the bacterial concentration to $2x10^{9}$ bacteria/mL. Luria broth-agar plates were coat with 100 µL and let dry for 1h. Filter paper discs were soaked in the PBS incubated with drug-ceramic hybrids or unloaded ceramics, place onto the plate, and incubated overnight at 37^{o}C. Measurements of the inhibition zone were performed on digital images of the plates. Control experiments including PBS solutions incubated with ceramics without drug or standard drug solutions of known concentrations were tested in parallel.

3.2.6.2. Cisplatin

Rat H4IIE HCC cells (ATCC, Bethesda, MD) were cultured in αMEM medium supplemented with FBS (10% (v/v)) to 75-80% confluence. The cells were then detached using trypsin-EDTA and seeded into 24-well plates (cell counts) and grown to 70-80% confluence. At this point, cells were made quiescent by replacing culture medium with low serum αMEM (LSM; 0.1% (v/v) FBS) for 24 h. Culture medium was then aspirated. Cells were washed twice with PBS (37°C), and culture medium supplemented with 1% (v/v) FBS containing PBS-Cis collected from drug release kinetics studies at different immersion times. To perform these studies, 200 µL aliquots were added to cultured cells

(n=3). Preliminary measurements of cell death were performed by total cell counts. Briefly, cells were treated with either Cisplatin-DMSO (0-250 μM) or Cisplatin solution collected from the Cris-Cis, Rhe-Cis and SCPC50-Cis release studies. 24 or 48 h later culture medium was removed, cells detached (trypsin-EDTA), and counted using a Countess Automated Cell Counter (Invitrogen, Carlsbad, CA).

3.2.7. Statistical Analyses

The data were expressed as the mean ± SD. Statistical analyses were performed following the same procedure explained in section 2.2.7.

3.3. Results

3.3.1. Drug Loading

3.3.1.1. Cisplatin Loading

Three consecutive washing steps in 70% nitric acid were needed to wash out the total amount of Cisplatin loaded onto each ceramic. Measurements of the Pt content in the ceramic carriers using ICP indicated that the amount of Cis loaded was equal to 10.83±0.40, 7.15±0.20, and 5.38±0.44 μg Cis per mg of Cris, Rhe and SCPC50 respectively, i.e., (Figure 3.1). Statistical analysis showed significant differences among all the Pt concentrations measured by ICP ($p<0.05$). The normalized Cis absorbed with respect to the ceramics surface area resulted to be 8.59±0.32 μg Vanc/m^2 for Cris, 17.8±0.5 μg Vanc/m^2 for Rhe and 6.03±0.50 μg Vanc /m^2 for SCPC50.

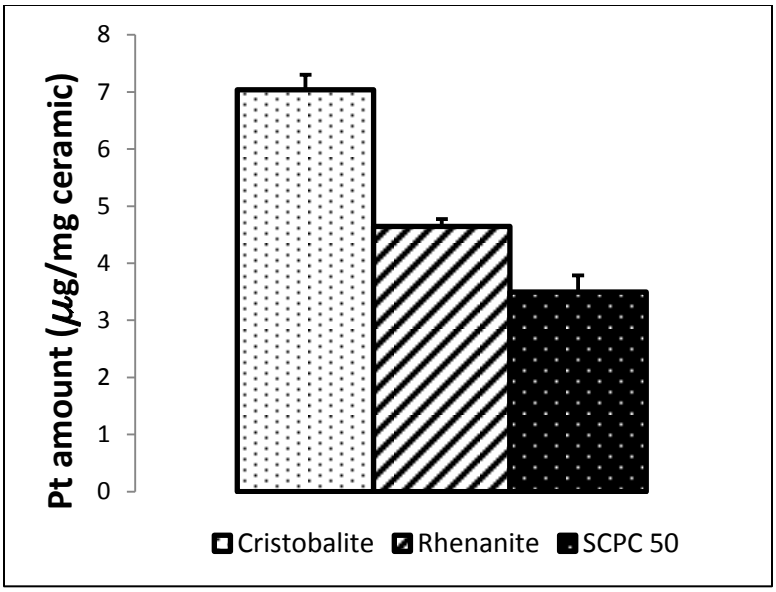

Figure 3.1: Total amount of Cisplatin loaded on Cris, Rhe and SCPC50.

3.3.1.2. Vancomycin Loading

HPLC measurements of the concentration of Vanc in PBS showed the dependence on the amount of drug adsorbed with respect to soaking time for the three samples. Similar concentrations were measured for all the samples at 16 h of immersion corresponding to 3.8±0.6, 3.2±0.4, and 4.0±0.04 µg of drug/mg ceramic on Cris, Rhe and SCPC50 respectively. Only the concentrations Vanc loaded on Rhe and SCPC50 showed to be significantly different ($p<0.05$). The normalized Vanc absorbed with respect to the surface area measured by HPLC resulted to be 3.01±0.5 µg Vanc /m^2 for Cris, 8.00±1.0 µg Vanc/m^2 for Rhe and 4.49±0.05 µg Vanc /m^2 for SCPC50. After 16 h of immersion, at 24 h of incubation, significant increase in the amount of Vanc adsorbed by SCPC50 was measured, together with a significant decrease in the amount of drug adsorbed by Cris and Rhe samples. At 48 h immersion, comparable amounts of Vanc to those measured at 16 h were measured, without significant differences among them (Figure 3.2). Therefore, 16 h was chosen as the loading Vanc loading time.

TG measurements of the Vanc loaded on the ceramics after 16 h immersion were 9.8±2.1, 7.3±0.8 and 6.6±1.8 µg of drug per mg of Cris, Rhe and SCPC50 respectively. The normalized Vanc absorbed with respect to the surface area measured by TG resulted to be 7.78 µg Vanc/m^2 for Cris, 18.25 µg Vanc/m^2 for Rhe and 7.41 µg Vanc /m^2 for SCPC50 (Figure 3.3). The amount of Vanc loaded measured by TG was nearly doubled that measured by HPLC. This can be due to the additional Vanc accumulated in the pores particles that stay during the drying step.

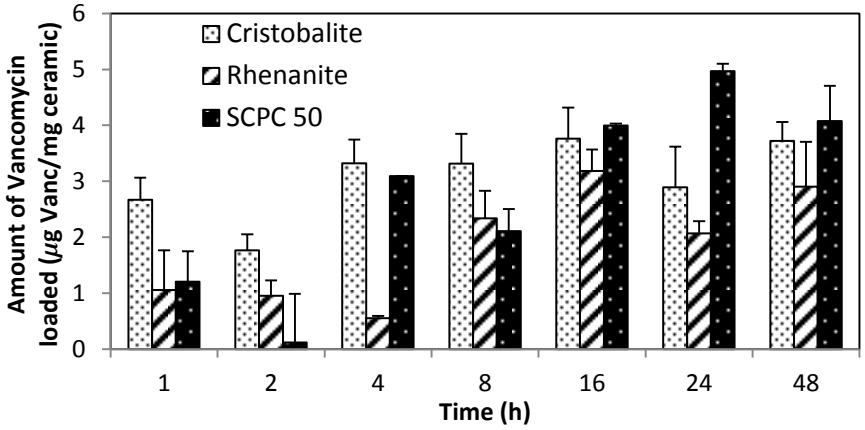

Figure 3.2: Differences between the initial Vanc solution (8 mg/mL) and the solution incubated with particles at different time points, indicating the amount of drug adsorbed by every carrier.

DSC analysis of the control Vancomycin showed a two steps process for the decomposition of the Vanc molecule. The first step was measured to occur around 327.82^oC and the second one at 474.32^oC. Vanc loaded on the different carriers also exhibit the two steps process, but the decomposition of the drug was measured at lower temperatures than the reference drug (Figure 3.3 a). Moreover, differences in the amount of energy needed to decompose Vanc control and that loaded on the ceramics were found. DSC showed that higher amount of energy is needed to burn out the Vanc loaded

on Cris and SCPC50 ceramics. Conversely, the amount of energy required to decompose the Vanc loaded on Rhe was significantly lower (Table 3.1).

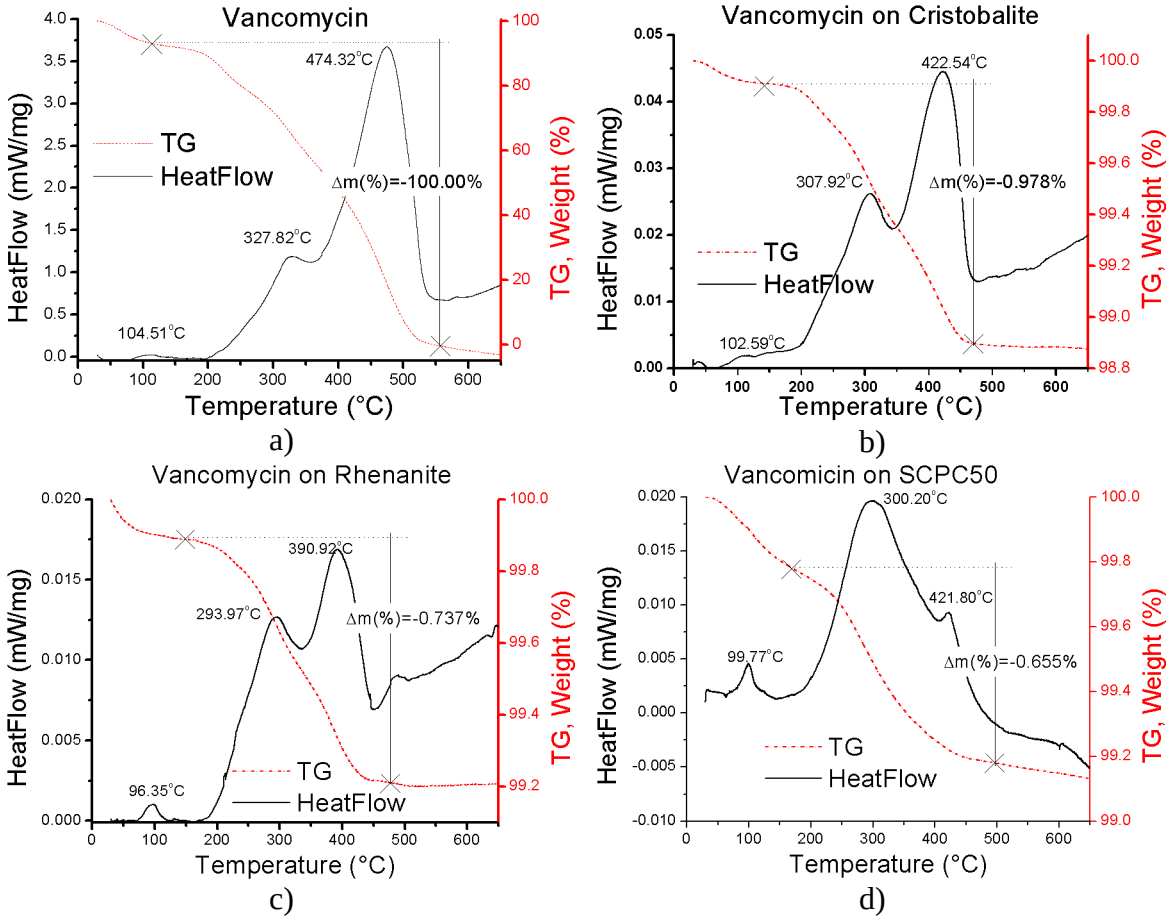

Figure 3.3: Thermal analysis (TG-DSC) of a) Vancomycin and Vancomycin loaded on b) Cristobalite, c) Rhenanite and d) SCPC50.

Table 3.1: Decomposition temperature and heat per Vanc unit mass measured by DSC. The temperatures T1 and T2 are the center of the exothermic peaks from the thermal decomposition of Vanc control and Vanc loaded on various ceramics. T1<T2.

Sample ID	Decomposition Temperature (°C)		Decomposition energy (mW/mg of Vanc)		
	T1	T2	Peak 1	Peak 2	Total
Vanc	327.82	474.32	79.18	322.43	401.61
Vanc on Cris	307.92	422.54	167.45	288.57	456.02
Vanc on Rhe	293.97	390.92	121.5	116.16	237.66
Vanc on SCPC50	300.2	421.8	405.45	77.7	483.15

3.3.2. Release Kinetics

Vancomycin: In vitro release kinetics Figure 3.4 a) shows the percentage of the mean cumulative concentration of Vanc released from Cris, Rhe and SCPC50 samples. About 50% of the Vanc loaded on Cris and SCPC50 samples, and 46% from the Rhe sample, were released during the first two hours of incubation. In order to analyze the drug release data from the different carriers, cumulative percentage of Vanc release vs. time (h) in logarithm scale was plotted (Figure 3.4 b). A linear region between 4 to 120 hours was observed in the three curves, indicating controlled release of drug within this period. After 120h, 100% of Vanc loaded on Cris and Rhe, and about 90% on SCPC50 was measured to be released from the different carriers. Therefore, plateau of Vanc release was observed after 120 h, and not further Vanc release was measured from the SCPC50 sample. Table 3.2 shows the correlation between the Vanc release kinetics data and release kinetic models over the period between 4 to 120 hours. Good correlation between the release profiles and the First order release model was seen as indicated by the R^2 values close to 1.0. This model describes the drug release rate relationship with the concentration of drug involved in the process. Likewise, good linear fittings were found using both Higuchi's and Hixson Crowell cube root models (similar R^2 between the two models). Higuchi model indicates the release of drug from the matrix as a square root of time dependent process based on Fickian diffusion. Hixson Crowell model indicates a change in surface area and geometry of the particles with the progressive dissolution of matrices as a function of time. The three models suggest variable release rate from the carrier with respect to time, and this variation can be calculated at each time point using the K values reported in Table 3.2. It is clear for all the models that the highest release

rate were obtained for Cris, followed by Rhe and then SCPC50. Using data from the zero release fitting, the average rate of release in terms of the amount of Vanc dissolved or released per unit time obtained for Cris, Rhe and SCPC50 are 26.2µg/h, 15.8 µg/h, and 14.5 µg/h respectively. Analysis of the mechanism of release kinetics, the values of the release exponent "n" in Vanc sustained release from Cris, Rhe and SCPC50 corresponded to 0.223, 0.210 and 0.180 which are beyond the limits of the Korsmeyer-Peppas model. Limitation of the power law to give discern into the exact kinetics mechanism of the drug release, lead to suggest a complex synergic between diffusion and erosion release control.

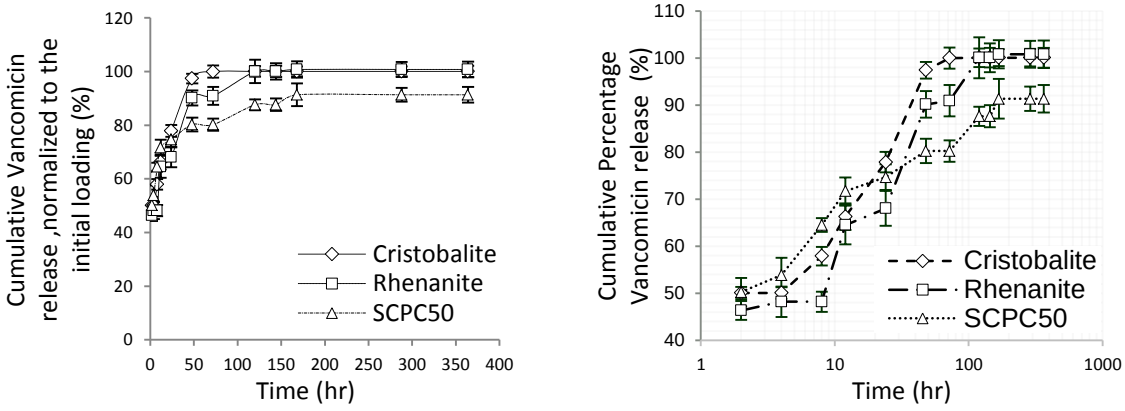

a) b)

Figure 3.4: a) Cumulative percentage Vancomycin release profiles from Cristobalite, Rhenanite and SCPC50 vs time, b) when data is plotted against squared root of time, it shows linear correlation, indicating diffusional drug release.

Table 3.2: Release kinetics constants and R^2 calculated from Vanc released from Cris, Rhe and SCPC50.

Matrix	Zero order		First Order		Higuchi		Hixson-Crowell		Korsmeyer-Peppas		
	R^2	$K_o(h^{-1})$	R^2	$K_1(h^{-1})$	R^2	$K_H(h^{-1/2})$	R^2	$K_{HC}(h^{-1/3})$	R^2	n value	$K_H(h^{-n})$
Cris	0.96	1.35	0.99	0.04	0.99	38.35	0.98	0.38	0.94	0.22	43.53
Rhe	0.76	1.06	0.79	0.03	0.79	31.94	0.82	0.34	0.96	0.21	37.14
SCPC50	0.72	0.49	0.82	0.02	0.95	31.12	0.85	0.43	0.94	0.18	37.20

Cisplatin: Release kinetics profiles of Cisplatin from Cris, Rhe and SCPC50 is presented in Figure 3.5, as the percentage of the mean cumulative concentration of Pt vs. time. The percentage of drug released from the carriers during the first 2h was respectively 53.4, 36.6 and 30.6 % for Cris, Rhe and SCPC50. Plot of the cumulative release vs. time in logarithm scale, showed continuous linear correlations in the region between 2-168 hours for Cris, 2-120 for Rhe and 2-216 h for SCPC50, was seen in the three curves, indicating controlled release of drug within these periods. After these time frames, no significant increase in drug release was measured with about 100% of the initial loaded Cisplatin released from each carrier. Good linear fittings were found using both Higuchi's and Hixson Crowell cube root models (similar R^2 between the two models). First Order release also showed good correlation in the case of Cris and SCPC50. Contrary to the Vanc release, it is clear for all the models that the highest Cisplatin release rate were obtained for Cris followed by Rhe and SCPC50. The average release rate of Cisplatin per unit time, calculated using data from zero order model, for Cris, Rhe and SCPC50 were 14.2µg/h, 8.01 and 4.66 µg/h respectively (Table 3.3).

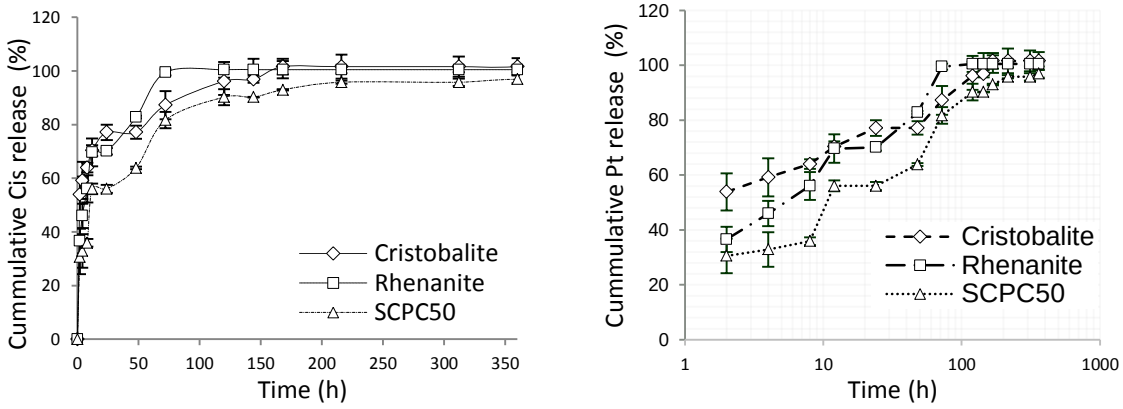

a) b)

Figure 3.5: Percentage cumulative release profiles of Cisplatin from SCPC50, Cristobalite and Rhenanite.

Table 3.3: Correlation coefficients (R^2) and release kinetics constants obtained by fitting release kinetic profiles of Cis from Cris, Rhe and SCPC50 data to different models of drug release.

Matrix	Zero order		First Order		Higuchi		Hixson-Crowell		Korsmeyer-Peppas		
	R^2	$K_o(h^{-1})$	R^2	$K_1(h^{-1})$	R^2	$K_H(h^{1/2})$	R^2	$K_{HC}(h^{-1/3})$	R^2	n value	$K_H(h^{-n})$
Cris	0.92	1.01	0.97	0.03	0.98	6.97	0.96	0.08	0.99	0.15	48.58
Rhe	0.76	0.86	0.89	0.02	0.87	6.83	0.86	0.05	0.95	0.26	32.38
SCPC50	0.95	0.70	0.96	0.02	0.97	7.23	0.90	0.04	0.96	0.28	22.94

3.3.3. Surface Chemistry

3.3.3.1. Vancomycin and Cisplatin loaded carriers

Cristobalite: after loading with Vanc bands at 1661.6, 1605.9, 1514.0 and 1485.0 cm^{-1} corresponding to ν C=O, δ N-H_2, δ N-H and aδ CH_3 from Vancomycin were observed. Lonely silanol group band at 3738 cm^{-1}, corresponding to those Si-OH bonds without H bridges among them [343], was significantly reduced (Figure 3.6*a*). After Cis loading FTIR analysis showed bands characteristic for the ammonium ions and secondary amine of Cisplatin can be seen (Figure 3.6a). No appreciable changes in location or intensity of the silica bands were observed including the Si-OH functional group signal at 953 cm^{-1}.

Rhenanite: a broadband at 1654.3-1695.2cm^{-1} corresponding to ν C=O, δ N-H_2, δ N-H and aδ CH_3 bonds at 1586.5, 1505.0 and 1487.5 cm^{-1} respectively, were detected. Intensity of the band close to 800cm^{-1} corresponding to P-OH significantly decrease after Vanc loading. Interactions between drug and P-OH group were confirmed by the disappearance of the bands at 2854-2962 cm^{-1} corresponding to ν P-OH and the broadening of bands at 1213 -1190 cm^{-1} corresponding to the stretching vibration and plane bending of the ν P=O respectively (Figure 3.6 b). FTIR analyses of the Cis loaded ceramic showed bands at 2913-3275 cm^{-1} corresponding to ammonium ions and

secondary amine [382]. The presence of theses amine bands indicates the expression of these NH_2 functional groups on the ceramic surface. The area of the FTIR band in the wave number range 566-595 cm^{-1} corresponding to O-P-O(H) [341] on the surface of Rhe decreased from 47.743 to 35.376 after Cisplatin binding, and then goes back to 46.783 after the drug release period. The decrease in the area can be taken as evidence of chemical bonding between the Cisplatin molecule and the ν P=O functional group on the material surface. Moreover, broadening of bands at 1213 -1190 cm^{-1} were observed (Figure 3.6*b*).

SCPC50: A broad band centered at 1666.3 cm^{-1}, corresponding to ν C=O, and another at δ N-H_2 at 1611.9 cm^{-1} confirmed the presence of Vanc on the SCPC50 surface. P-OH bands were not seen in the SCPC50-vanc loaded sample (Figure 3.6c). The presence of Cisplatin on the surface of SCPC50 was confirmed by identification of bands centered at 788.9, 1436.7, 1486.4 and 1645.5 cm^{-1} on the SCPC50-cis loaded spectra (Figure 3.6c). The area under the peaks at 1153.6-1214.6 cm^{-1} and 1084 cm^{-1} corresponding to ν-P=O and ν-P-O increased. On the other hand, FTIR did not measure any changes in the energy or area under the peak for the Si-OH group after drug loading on SCPC50 (Figure 3.6c).

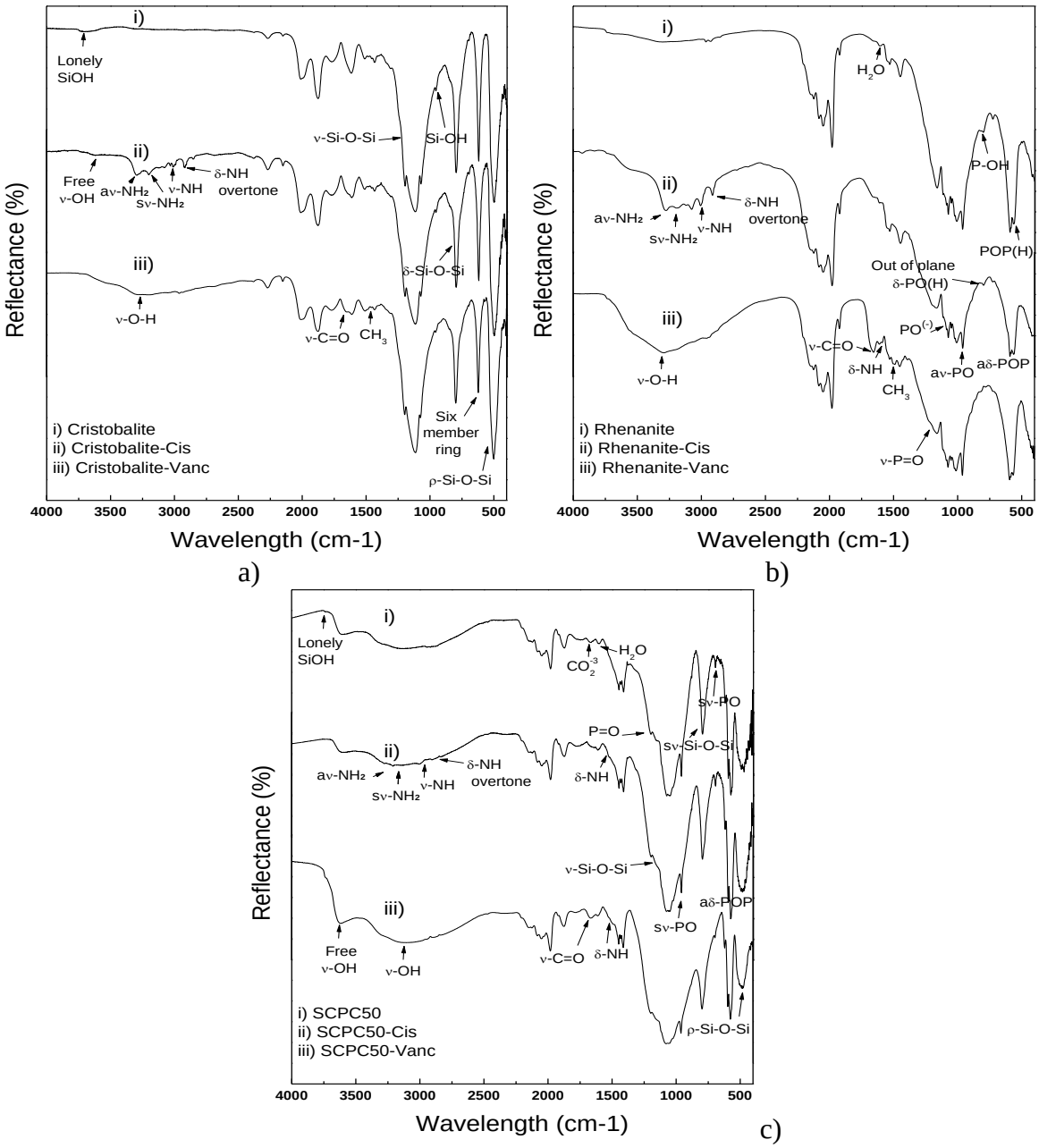

Figure 3.6: FTIR spectra of a) Cristobalite, b) Rhenanite and c) SCPC50, as starting materials, after soaking SCPC50 for 24 hours in SBF, after drug loading.

3.3.4. Dissolution Analysis

3.3.4.1. Ca Dissolution

ICP measurements of the Ca concentration from the PBS incubated with SCPC50-Cis, SCPC50-Vanc and SCPC50 Control showed no significantly difference between the amount of Ca released from the SCPC50–drug hybrids (drug could be either Cis or Vanc) and the control SCPC50 ($p<0.05$). Amount of Ca released from SCPC50-drugs and SCPC50 control oscillated between a maximum of 1.226±0.528 µg/ml and zero indicating absorption and desorption at different periods of time (Figure 3.7a). On the other hand, Ca dissolution kinetic in the PBS incubated with Rhe-Cis, Rhe-Vanc and Rhe Control showed three different stages. The first stage, between 2 to 24h, did not show significant increment in the Ca release rate for Rhe-Cis and Rhe-Vanc. During the second stage from 24 to 120 h, an increase in the rate of calcium dissolution of about 0.124±0.011 µg/ml/h, 0.039±0.004 µg/ml/h and 0.127±0.051 µg/ml/h for Rhe-Cis, Rhe-Vanc and Rhe Control respectively. At 120h the concentrations of Ca measured from Rhe-Cis, Rhe-Vanc, and Rhe control were 12.817±0.610 µg/ml, 6.039±0.090 µg/ml and 15.541±0.223 µg/ml respectively. During the third stage from 120 to 520 h (when both drugs have been released almost completely from the Rhe), the Ca concentration in the PBS incubated with Rhe-Cis hybrid gradually decline at a rate of -0.020±0.008 µg/ml/h until the last time point, while for the Rhe-Vanc sample it is maintained almost constant. Interestingly, a further increase of Ca concentration was measured in the PBS incubated with Rhe control at a rate of 0.024±0.001 µg/ml/h during the same period of time (Figure 3.7b).

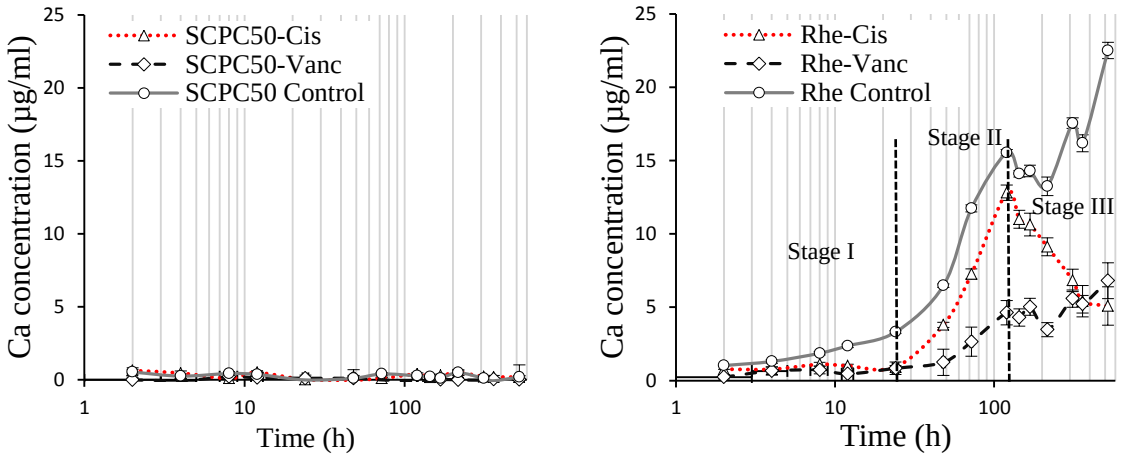

Figure 3.7: ICP measurements of the amount of Ca released in PBS incubated with a) SCPC50-Cis hybrid and SCPC control and b) Rhe-Cis hybrid and Rhe control.

3.3.4.2. P Dissolution

No significant differences were measured in the dissolution kinetics profiles for P from the PBS incubated with neither SCPC50-drugs and Rhe-drugs nor SCPC50 and Rhe control samples. Difficulties in the phosphorous detection could be due to the relatively high amount of P in the PBS (Figure 3.8).

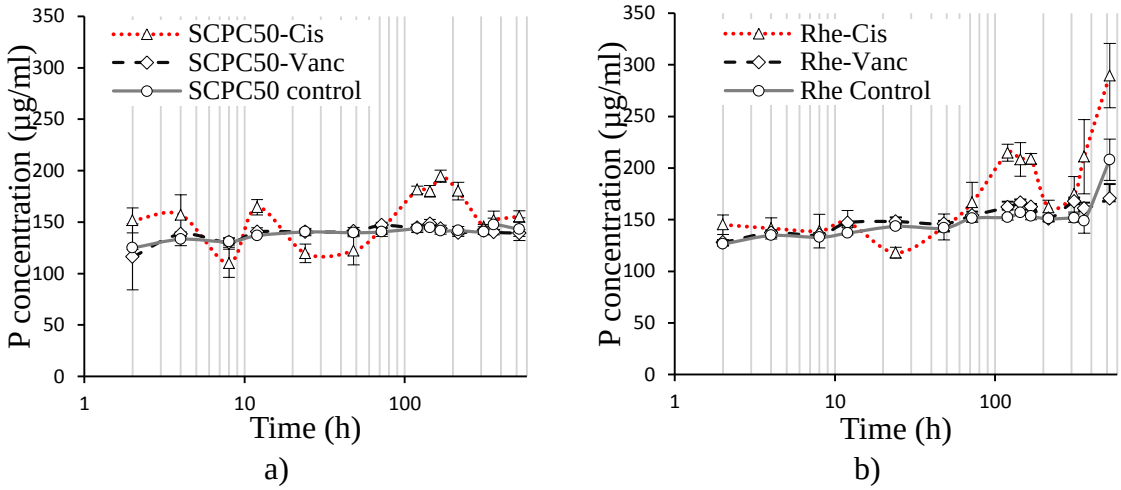

Figure 3.8: ICP measurements of the amount of P found in PBS incubated with a) SCPC50-Cis hybrid and SCPC control and b) Rhe-Cis hybrid and Rhe control.

3.3.4.3. Si Dissolution

No significant difference in the dissolution kinetic profiles for the silica released from SCPC50-drug hybrids and SCPC50 control was found throughout the entire period of the experiment. Between 2 and 24 hours no significant increase in the Si content was measured for any carrier. After that, from 24 to 168 h, the concentration of Si in the solution increased at a rate of 0.719±0.010, 0.582±0.049 and 0.612±0.056 µg/ml/h for SCPC50-Cis, SCPC50-Vanc and SCPC50 control respectively. Then, for the period between 168 to 520 h, the Si release rate is reduced to 0.173 ±0.087, 0.180±0.053and 0.202±0.091 µg/ml/h for SCPC50-Cis, SCPC50-Vanc and SCPC50 control (Figure 3.9a). In contrast, minimal changes in the concentration of silica during the release time period were measured for Cris-drug hybrids and Cris control (Figure 3.9b).

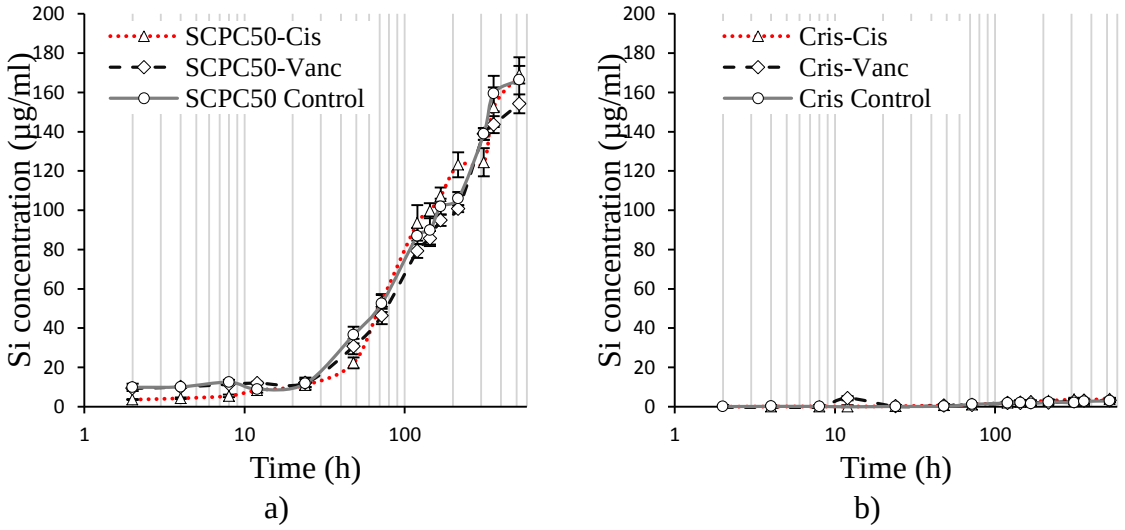

Figure 3.9: ICP measurements of the amount of Si released in PBS incubated with a) SCPC50-Cis hybrid and SCPC control and b) Cris-Cis hybrid and Cris control.

3.3.4.4. Particles Deterioration after Release Kinetics

SEM analysis showed significant erosion and breakdown of the ceramic particles tested for the release kinetics experiments. Cris sample showed the most notorious

deterioration followed by Rhe and then SCPC50 (Figure 3.10). The lower deterioration of the SCPC50 particles can be attributed to the high sinterability of the SCPC50 particles. Partially melted Si-rich glassy phase, form during sintering, enhance the adhesion among Rhe and Cris grains of the SCPC50 particles [18, 383]. Presence of small particles (< 250-425 μm) indicates the breakdown of SCPC50 (Figure 3.10*c*). The highest deterioration of the Cris particles indicates low sintering between the small cristobalite grains forming the micro particles (Figure 3.10*a*). The highest dissolution rate of Rhe yielded to a notorious increase in the pore size of Rhe particles, and an intermediate breakdown between Cris and SCPC50 (Figure 3.10*b*).

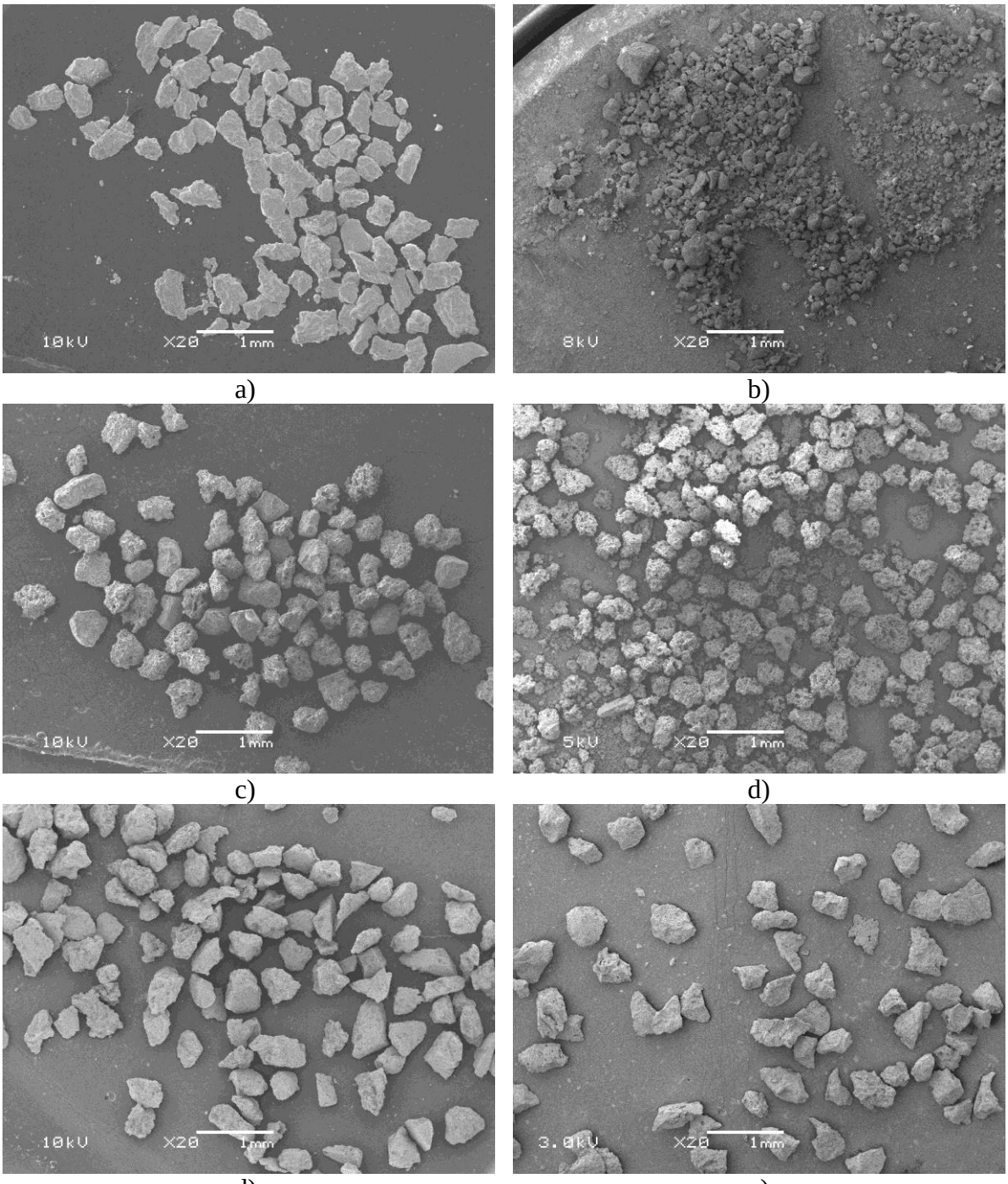

a) b)

c) d)

d) e)

Figure 3.10: a) Cristobalite, c) Rhenanite and d) SCPC50 drug loaded particles, and b) Cristobalite, d) Rhenanite and e) SCPC50 after 20 days in vitro release kinetics experiment; Cristobalite particles undergo significant degradation and most of the particles are completely eroded; Rhenanite showed less severe particle deterioration with significant increase in its pore size; and SCPC50 showed to be the least eroded particles most probably due to the calcium phosphate layer form on the surface of the particles.

3.3.5. Cytotoxicity Tests

The bacterial inhibition assay revealed the retained biological activity of Vanc eluted from the ceramics (Cris, Rhe and SCPC50) at different time points. The average diameter of the inhibition zone as a function of the release time is represented in Figure 3.11. During the first day, the diameters of the inhibition zones due to Vancomycin release from Cris were significantly higher than those due to Vanc release from Rhe and SCPC50. After one day, no significant differences were measured among the Vanc eluded from all the carriers. Besides, aliquot of PBS incubated with Cris, Rhe or SCPC50 without antibiotic did not show any inhibitory effect. This indicates that the bactericide effect is mainly due to the antibiotic released from the ceramic-drug hybrids into the solution.

Experiments of aliquots of PBS incubated with Cris, Rhe, and SCPC50 + Cis hybrids, collected at different time points, showed retained cytotoxicity of the drug eluted from the ceramic-Cis formulations against H4IIE HCC cells (Figure 3.12). Significant reduction ($p<0.05$) of about ~25% in the number of cells counted was observed compared with untreated cells and control aliquots of PBS incubated with unloaded ceramics.

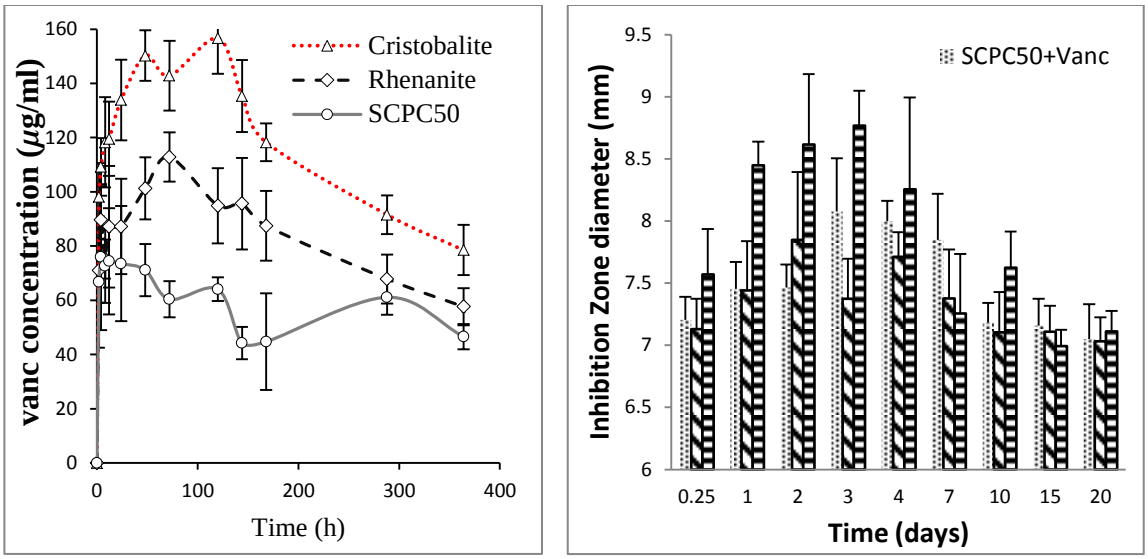

a) b)

Figure 3.11: a) Dose response curve for the cytotoxicity of Vanc in S. aureus is also showed. b) Inhibition zone measured for S. aureus treated with aliquots taken from the PBS incubated Cris, Rhe, and SCPC50 loaded with Vanc. No zone of inhibition was observed for the control samples (PBS incubated with Cris, Rhe and SCPC50 without any drug).

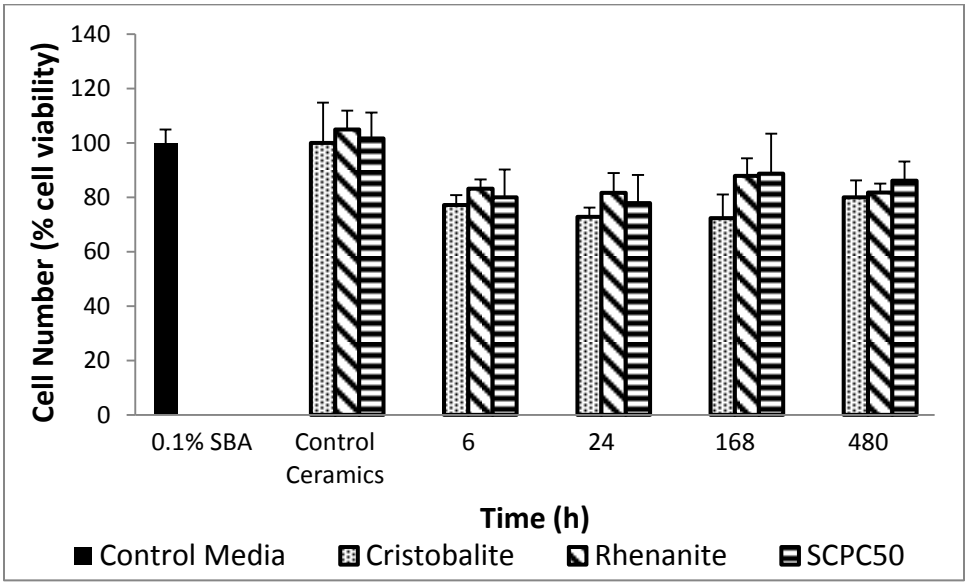

Figure 3.12: Cytotoxicity effect of Cisplatin released from Cris, Rhe and SCPC5 in H4IIE cells in vitro 24h. Cris, Rhe and SCPC50 alone (no Cisplatin) do not affect cell viability, control Media with 0.1% Bovine Serum Albumin (BSA) is also depicted. Dose response Cisplatin toxicity has been reported already for our group [380].

3.4. Discussion

The ceramic composition and microstructure controlled drug binding and release kinetics. Furthermore, per each ceramic, the ability of drug binding and release was dependent on the type of drug. These observations suggest that a custom made delivery system is necessary for each drug. With respect to cristobalite, binding was mainly dependent on the surface area. FTIR analyses did not show a detectable change in the absorption bands of the Si-O functional group suggesting physisorption. On the other hand, for Rhe and SCPC50 FTIR analyses suggested that the P-O functional groups are the active site for drug binding. Although, Cris has three times higher surface area than Rhe, yet comparable amounts of Vanc were bond to the two materials. These results emphasize the significant role of surface chemistry and functional groups in drug binding to bioactive materials. The nature of bonding at the interface between drug and ceramic contributed to significant variations in release kinetics. Cris showed the fastest release rate compared to Rhe and SCPC50. In contrary, SCPC50 showed the lowest rate of release due to the high bioactivity of the material surface and the continuous deposition of hydroxyapatite in physiological solution. Therefore, it is possible to tailor custom made SCPC-drug release kinetics hybrids by controlling the crystalline structure of the material, and the ratios of Cris and Rhe in the composite.

3.4.1. Role of Porosity and Surface Area:

Porosity and surface area are usually the key factors correlated with a biomaterial capacity for drug loading and release kinetics [362, 363, 384, 385]. Indeed, TG and ICP analyses showed that the drug binding per unit mass of Cris was significantly higher than that per unit mass of Rhe or SCPC50. This is attributed to the high surface area of Cris

strongly related to the pore size distribution. About ~22.5% of Cris porosity was found in the pore size range 0.2-1 μm while 4.7% and 2.2% of SCPC50 and Rhe porosity was found in the same size range, respectively. On the other hand, although SCPC50 had two fold higher BET surface area than rhenanite, yet the amounts of Cisplatin and Vancomycin adsorbed per unit mass of rhenanite was significantly higher than that adsorbed per unit mass of SCPC50. These results suggest that the effect of phase composition and surface chemistry on drug binding to bioactive ceramics overrule the effect of surface area. Rhe doubled the amount of Cis or Van adsorbed per surface area compared to those adsorbed onto Cris or SCPC50. Similar amounts of drug adsorbed per unit surface area of Cris and SCPC50 were measured. These results were obtained even when Cris has significantly higher surface area and nano-porosity than SCPC50. Rhenanite is a bioactive ceramic known to have high chemical reactivity that leads to material dissolution [386]. Therefore, the surface of Rhenanite is dominated by the active functional groups PO_4^{3-} that induces high surface charge and chemical reactivity which enhances both physical adsorption and chemisorption of drug molecules.

3.4.2. Role of Surface Chemistry

FTIR analyses suggested that the drug binds Rhe is through the non-bridging Oxygen in the P-O-P network. The involvement of the P-O functional groups in drug binding is supported by the consistent broadening of the P=O signal at 1213-1190 cm^{-1} Figure 3.6b) after adsorption of Vancomycin adsorption. Moreover, the disappearance of the P-OH band at 2854-2962 cm^{-1} is an additional confirmation to the role of the phosphate group in enhancing drug binding to Rhe. On the other hand, FTIR results did not show a strong evidence for the alteration of the Si-O functional groups in cristobalite.

FTIR analyses (Figure 3.6a) showed the disappearance of the small signal characteristic of lonely silanol group after drug adsorption indicating that this is the active site for the drug adsorption on Cris. The weakness of the lonely silanol group suggests that most of the drug loaded on the Cris is bound by physisorption forces. For SCPC50, 73 % of the material is rhenanite (Table 2.2). Therefore, similar interaction between the P-O functional groups and the drug molecules is expected. Indeed, FTIR showed an increase in the area under the peaks for the bands at 1153.6-1214.6 cm^{-1}, 1408 cm^{-1} and 1084 cm^{-1} corresponding to P-O (H) bending mode suggesting a chemical interaction between drug molecules and the P-O groups on the material surface. On the other hand, the persistence of the Si-OH band after drug loading (Figure 3.6c) suggests a minimal role of this functional group in drug binding to SCPC50.

3.4.3. Comparison of TG with HPLC

Measurements of the Vanc loaded on the ceramics were carried out using two different methods: HPLC and TG. The amounts of Vanc determined using TG were higher than those measured using HPLC. The difference in the amount of Vancomycin is understood in view of the method of determination of the adsorbed drug. For the HPLC, the Vancomycin bound to the ceramic was calculated as the difference in the drug concentrations of the immersing solution before and after immersion. On the other hand, for the TG method, the particles were removed from the immersing Vancomycin solution, dried then thermally analyzed without washing. The drying of the remnant Vancomycin solution inside the porous particles after immersion contributed to the increased amount of drug loaded per each ceramic. The amount of dried drug on the porous ceramic particles was proportional to the surface area of each material and

increased in the order Cristobalite > Rhenanite > SCPC50. For release kinetics studies we used ceramic particles loaded with the drug without washing. After complete release of the drug from the ceramics, calculation of the cumulative drug released matched the initial amount of drug loaded on each material as determined by TG or ICP-EOS methods. The dried drug on the material surface contributed to the burst release stage seen in the release kinetics profiles (Figure 3.4a, and Figure 3.5a). Considering that the HPLC difference in Vancomycin concentrations, before and after ceramic immersion, represents the absorbed drug on the material surface, the Vanc absorbed on each material per surface area, confirm the high affinity of Vanc to the surface of Rhe, and also reveal that SCPC50 has higher drug loading capacity per surface area when compared to Cris. Therefore, the drug loading capacity of bioactive ceramics is significantly dependent on the phase composition, surface area, and surface chemistry.

3.4.4. Thermal Analyses

DSC analyses demonstrated a reduction in the thermal decomposition energy of Vancomycin after adsorption onto Rhenanite surface. This decrease is expected in view of the separation of the drug molecules on the material surface during adsorption as compared to the presence of these molecules in crystalline form in the control drug. On the other hand, the thermal decomposition energy of Vancomycin adsorbed onto Cris was significantly higher than that of control Vancomycin. The increase in the thermal decomposition energy of Vancomycin can be understood in view of the pore size distribution of Cris as well as the nature of the interaction between the drug molecules and the substrate. Although Cris has a comparable porosity percent to Rhe, however, 22.5 % of the pores in the former material were (< 1 μm) compared to 2.2 % of the same pore

size for the later material (Table 2.1). Therefore, Vancomycin molecules entrapped in Cris nano pores require higher amounts of energy to break down (Table 3.1). Additionally, the significantly low thermal conductivity of Cris [387] can contribute to the increased decomposition energy for Vancomycin. Although, SCPC50 has 6.0 % of its pores<1 μm, yet the Vanc adsorbed onto its surface demonstrated higher decomposition energy than that adsorbed onto Cris. The increase in the decomposition energy of Vancomycin adsorbed on SCPC50 can be attributed to the nature of bonding between the drug molecules and the substrate, and the presence of nanopores. Therefore, more heat energy is required to achieve the critical value for the decomposition of Vanc. Furthermore, the surface hydroxyapatite layer represents an additional obstacle to the thermal decomposition of the Vancomycin adsorbed in the inner pores of SCPC50. Vanc loaded on all carriers showed lower decomposition temperature compared to the control Vanc (100% Vanc powder). The reduction in the decomposition temperature can be attributed to the resolution of the crystalline structure of Vancomycin and separation of the individual drug molecules adsorbed onto the material surface. It is also possible that the denaturation of the adsorbed molecules contributes to the decrease in the thermal stability.

3.4.5. Drug Release and Ceramic Dissolution Kinetics

Results of drug release kinetics demonstrated the ability of all carriers to bind and provide a sustained release of Vancomycin and Cisplatin. The low affinity between the drugs and Si-O-Si network; as demonstrated by FTIR (Figure 3.6*a*) and DSC analyses (Figure 3.3*b*), suggests that the drug release kinetics from Cris is mainly diffusion dependent; controlled by the large number of pores in the size range <1 μm (22.3%). In

addition, SEM analysis showed evidences of particles disintegration during immersion in PBS, thus increasing the surface area in contact with the immersing solution and enhanced the drug release (Figure 3.10). In contrast, the transport of drug out of the Rhe particles is controlled by its surface chemistry rather than its pores size distribution. The non-bridging P-O functional groups, including P-O(H), P-O(Ca), and P-O(Na), which dominate the surface of Rhe, has been demonstrated to chemically bind Vancomycin and Cisplatin (Figure 3.6). Hence, the drug release kinetics correlated well with the Rhe dissolution rate (Figure 3.7). It is interesting to note that, while a significant reduction in Ca dissolution from Rhe-drug hybrids was measured after 120 hours of immersion in PBS; the Ca dissolution rate of control Rhe without drug continued to increase. The decreased Ca concentration in the PBS incubated with Rhe after this period could be attributed to the enhanced precipitation of a calcium phosphate layer on the material surface. In the case of SCPC50 a more complex drug release mechanism is expected due to its hierarchical porous structure and its phase composition that comprise both Cris and Rhe and a silica rich glassy phase. It is also important to note that SCPC50 has a dynamic surface with a continuous dissolution-precipitation reactions taking place in PBS. SCPC50, SCPC50-Van and SCPC50-Cis samples showed comparable calcium and phosphorous dissolution rates. This is due to the domination of dissolution precipitation reactions continuously happening on the surface of the material during the incubation period in PBS as confirmed by FTIR. Ning, et al., and Liu, et al., demonstrated that the amorphous phase in SCPC50 is Silica-rich [18, 383]. Therefore, it is expected that Si from the amorphous phase dissolves faster than any other phase in the SCPC50. Dissolution of the Si from SCPC50 glassy phase seems to have no further effect in the

drug release other than its contribution in the material degradation and CaP layer formation. The bacterial inhibition assay (Figure 3.11) revealed that released Vancomycin maintained their biological cytotoxicity against *S. Aureus* in vitro. Moreover, quantitatively, the average diameter of the inhibition zone as a function of time correlates well with the concentration of Vancomycin eluted at each time point and measured by HPLC.

3.5. Conclusion

Results of this study demonstrate the ability of Cris, Rhe and SCPC50 particles to bind and release in a controlled fashion Vancomycin and Cisplatin. The chemical composition of the carrier dramatically affected the loading capacity and the release kinetics of therapeutics, besides its structural features. Physical structural characteristics of Cris demonstrated to exert a high impact on its ability to serve as DDS. Presence of nano pores and superior surface area suitable for drug loading allowed more drug loading capacity compared to Rhe and SCPC50.Sustained release showed to be controlled mainly by the tortuosity of constricted porous matrix due to the stability of the ceramic. Rhe demonstrated to be more chemical reactive and form more stable bonds with drug molecules, contributing to prolonged release of therapeutics. SCPC50 has the advantage to have both physical and chemical mechanisms for loading and release molecules. Therefore, microstructure and DDS ability of SCPC50 (which has more active Cris and Rhe phases) can be tailored depending on the ratio Silicate/Phosphate used to make the ceramic compound. Additional considerations should be taken into account when selecting the composition of SCPC composite for drug delivery. Final format of the ceramic matrix can represent additional obstacles. For example, particles compacted to

discs significantly limits the contact between the inner nanopores surface and surrounding fluids, complicating the diffusion of drug molecules entrapped inside the discs. Therefore, Si-rich SCPC (SCPC75) should be selected to overcome the increased tortuosity in the discs. As a result, reduced affinity between the bioceramic and drugs molecules would be obtained, yielding to faster release rates and reducing the possibility of drug retention, plus significantly increase drug loading capacity per unit of mass.

CHAPTER 4: EVALUATION OF THE EFFECT OF SCPC DISSOLUTION ON THE BIOACTIVITY OF THE ANTI-CANCER DRUG DOXORUBICIN

4.1. Introduction

Silicon calcium phosphate (SCPC) has been tested as a drug delivery platform to treat infection and cancer. The bioactivity reactions at the interface of bioactive ceramics and tissue fluids include a partial dissolution of the surface followed by a back-precipitation. These reactions have been shown to regulate the drug release kinetics. While most of studies have focused on the release kinetics and the bioactivity of released drug, little is known about the effects of dissolution products of the ceramic on drug bioactivity. SCPC has shown to cause minimum effect on the bioactivity of Cisplatin [388] and 5-FU [300] anticancer drugs, as well as on antibiotics Vancomycin and Gentamycin [299]. However the deterioration of drug agents caused by its interaction with ionic degradation products from SCPC deserves more attention. Doxorubicin (Dox) is a powerful anthracycline antibiotic that interacts with DNA by intercalation inhibiting its replication, transcription, and translation. Dox is commonly used in the treatment of a wide range of cancers, many human neoplasms, including acute leukemias, lymphomas, stomach, breast and ovarian cancer, and bone tumors. The high availability of functional groups (-C=O, -COOROH, -OH, -OR, -NH_3) within Dox molecule can lead to tautomerize from one functional group to other [389, 390]. The objective of this work is to analyze the interactions between drug molecules and the ionic degradation products of bioactive ceramics. Nuclear magnetic resonance (NMR) was proposed to analyze

possible chemical bonding between Dox with common elemental dissolution products from the dissolution of SCPC (Si, P, Ca and Na). Additionally, the effect of individual ion Doxorubicin toxicity for cancer cells is presented.

4.2. Materials and Methods

4.2.1. Reagents

Doxorubicin Hydrochloride, Reddish-orange Powder ≥95% (by HPLC), was purchase from Fisher Bioreagent (Fairlawn, NJ). Ions were obtained from H_2SiF_6 ICP/DCP standard solution at 10042µg/mL concentration in water, NaCl (≥99% ASC), and $CaCl_2$ $2H_2O$ (99+% ACS) purchased from Sigma-Aldrich (St. Louis, MO). Orthophosphoric acid (H_3PO_4), 85% aqueous Solution, was purchased from Alfa Aesar (Ward Hill, MA). Ions solutions were prepared in D_2O (D, 99.9%) purchased from Cambridge Isotope Laboratories Inc (Andover, MA). The pH was adjusted using Ammonium hydroxide (NH_4OH), volumetric standard, 4.98N solution in water purchased from Sigma-Aldrich., dissolved in D_2O at 1:10 volume ratio.

4.2.2. Sample Preparation

Stock solution of Doxorubicin (Dox) in D_2O at 1 mg/mL was prepared. Homogeneous drug solutions containing Silicon, Phosphorous, Sodium and Calcium in ion:drug molar ratios of 0:1, 32:1, 16:1, 8:1, 4:1, 1:1, 0.5:1, 0.25:1, and 0.05:1 were prepared. Final Dox concentration equals to 500 µg/mLwas maintained in all sample solutions. The samples were adjusted at pH 5.0±0.2 using NH_4OH solution dissolved in D_2O diluted at 1:10 volume ratio. A total of 1ml of each sample was prepared, from this 600 µL of each drug-ion solution was analyzed by NMR and left 400 µL used for cytotoxicity studies.

4.2.3. In Vitro Cytotoxicity of Ion:Dox Solutions

Aqueous solutions of Dox mixed with Ca, Na, P or Si at ion:Dox molar ratios 0:0 (control without Dox and ion) 0:1 (control "only Dox"), 32:1, 16:1, 8:1, 4:1, 1:1, 0.5:1, 0.25:1, and 0.05:1, 1:0 (control "only ion" at low concentration) and 32:0 (control "only ion" at high concentration) were sterilized through 0.2 μm filters. These samples were diluted to reach Dox final concentrations of 20, 2, 0.8 and 0.4 μM. Serum-free MCF7 breast cancer cells in a growing phase, confluence ~75-85 %, were seeded with all ions:Dox solutions in 96 well plates (n=6) and incubated at 37°C, 5% CO_2, and 100% humidity for 96 hrs. Cell cytotoxicity was tested using MTT assays, which are commonly used in cytotoxic studies and measure the mitochondrial activity [391], which is proportional to the live cell number. MTT assays were read using a plate reader (color change), and the results expressed as % cell survival compared to control conditions (i.e., no treatment). Control "only ion" samples (32:0 and 1:0) without Dox were calculated to match the Ca, Na, P or Si concentrations of 32:1 and 1:1 ion:Dox solutions but without Dox. These samples were thought to measure the cytotoxicity of Ca, Na, P and Si solutions without drug.

4.2.4. Nuclear Magnetic Resonance (NMR)

Proton NMR spectra were recorded on Bruker Avance at 700 or 500 MHz spectrometers with gradient shimming, auto sampler, and auto tuning at 298 K. Assignment of proton NMR signals was achieved using 2D COSY and NOESY spectra. The interactions of different ions with Dox were evaluated based on the changes of the chemical shifts of Dox. Chemical shifts of Dox were monitored by 1D proton spectra of Dox acquired at the constant concentration of the drug (500 μg/mL) in the presence of

increasing concentrations of Ca, Si, P, and Na (ion:drug molar ratios: 0:1, 1:1, 8:1 and 32:1). One dimensional 1H spectra were acquired into 32768 data points, spectral width of 12 ppm, 5 ppm offset, and relaxation delay 0.1s. No weighting functions were applied prior to Fourier transformation.

4.2.5. Treatment of NMR Data

Benesi-Hildebrand (B-H) linearization treatment was applied to calculate the association constant (K_a) of the drug with the various ions [392, 393].

$$1/\Delta\delta = 1/(K_a * \Delta\delta_{max}[Ho]) + 1/\Delta\delta_{max} \qquad \text{Equation 4.1}$$

Where $\Delta\delta=(\delta_{Dox}-\delta_{obs})$, $\Delta\delta_{max}=(\delta_{Dox}-\delta_{sat})$, K_a Dox-ion association constant, $[H_o]$ is the known total concentration of ions, δ_{obs} is the observed chemical shift in the Dox-ion solutions, δ_{Dox} is the observed chemical shift in the Dox solution without any ion.

4.2.6. Statistical Analysis

The data were expressed as the mean ± SD. One-way ANOVA was used to test for variance among two or more independent groups of data. Differences among treatment groups were evaluated using Tukey post-hoc testing. Results were considered to have statistical significance difference at the 0.05 level.

4.3. Results

MTT assays showed no significant influence on the MCF7 cell survival at Dox final concentrations of 20 and 2μM regardless the molar ratio between ions (Ca, Na, P or Si) and Dox (Figure 4.1, 4.2, 4.3 and 4.4). In contrast, solutions at Dox final concentrations of 0.8 and 0.4 μM showed a significant decreased ($p<0.05$) in the MCF7 cell survival when the molar ratio between Na or Ca ions and Dox were ≥ 0.5:1 (Figure 4.3). Moreover, in the case of P:Dox mixtures, only the solution with final Dox

concentration of 0.8μM and P:Dox molar ratio 8:1 showed significant decreases ($p<0.01$) in the survival of MCF7 cell with respect to the control "only Dox" (Figure 4.3). Solutions of Dox mixed with Si regardless of the molar ratio of Si to Dox did not alter the MCF7 cell Dox cytotoxicity at any of the Dox final concentrations tested (20, 2, 0.8 and 0.4 μM, Figure 4.4). Control "only ion" for Ca and P did not show cytotoxicity at any concentration tested. Conversely, control "only ion" Si and Na showed significant toxicity (**$p<0.01$ and *$p<0.05$). Si and Na samples labeled 32:0 and 1:0 showed a decrease in the viability of MCF7 cells when matched the Si or Na concentration of 32:1 and 1:1 with final Dox concentrations at 20 and 2μM (Figure 4.3 and Figure 4.4).

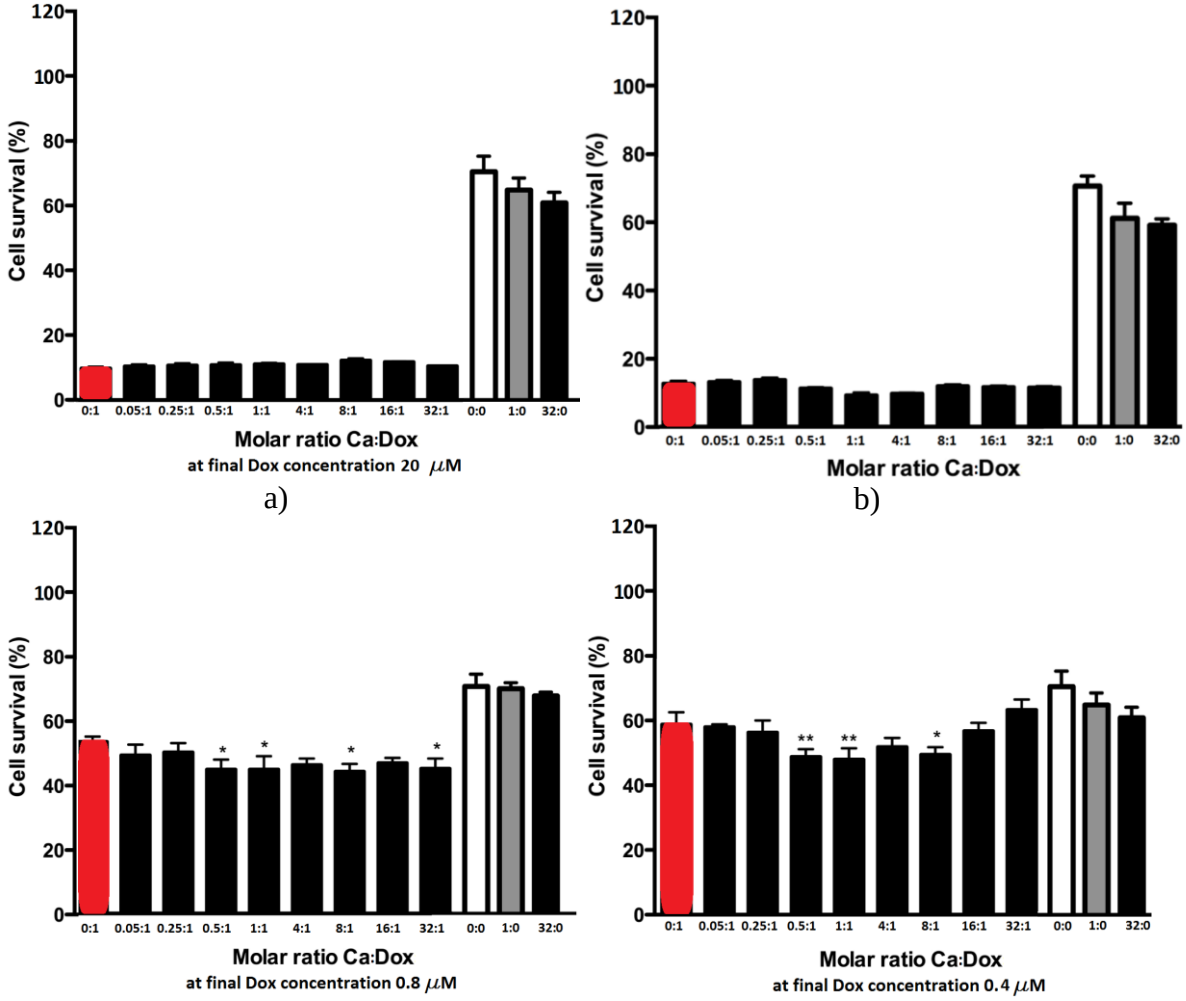

Figure 4.1: MTT assays showing the MCF7 Cell survival (%) against molar Ca:Dox solutions at molar ratios 0:0 (control media without drug or Ca), 0:1 (control "only Dox"), 32:1, 16:1, 8:1, 4:1, 1:1, 0.5:1, 0.25:1, and 0.05:1, 1:0 (control "only Ca" at low concentration) and 32:0 (control "only Ca" at high concentration). Results between were considered to have statistical significance difference at *P<0.05 and ***P<0.01. Statistical significance was evaluated between samples containing Dox and samples without Dox samples separately.

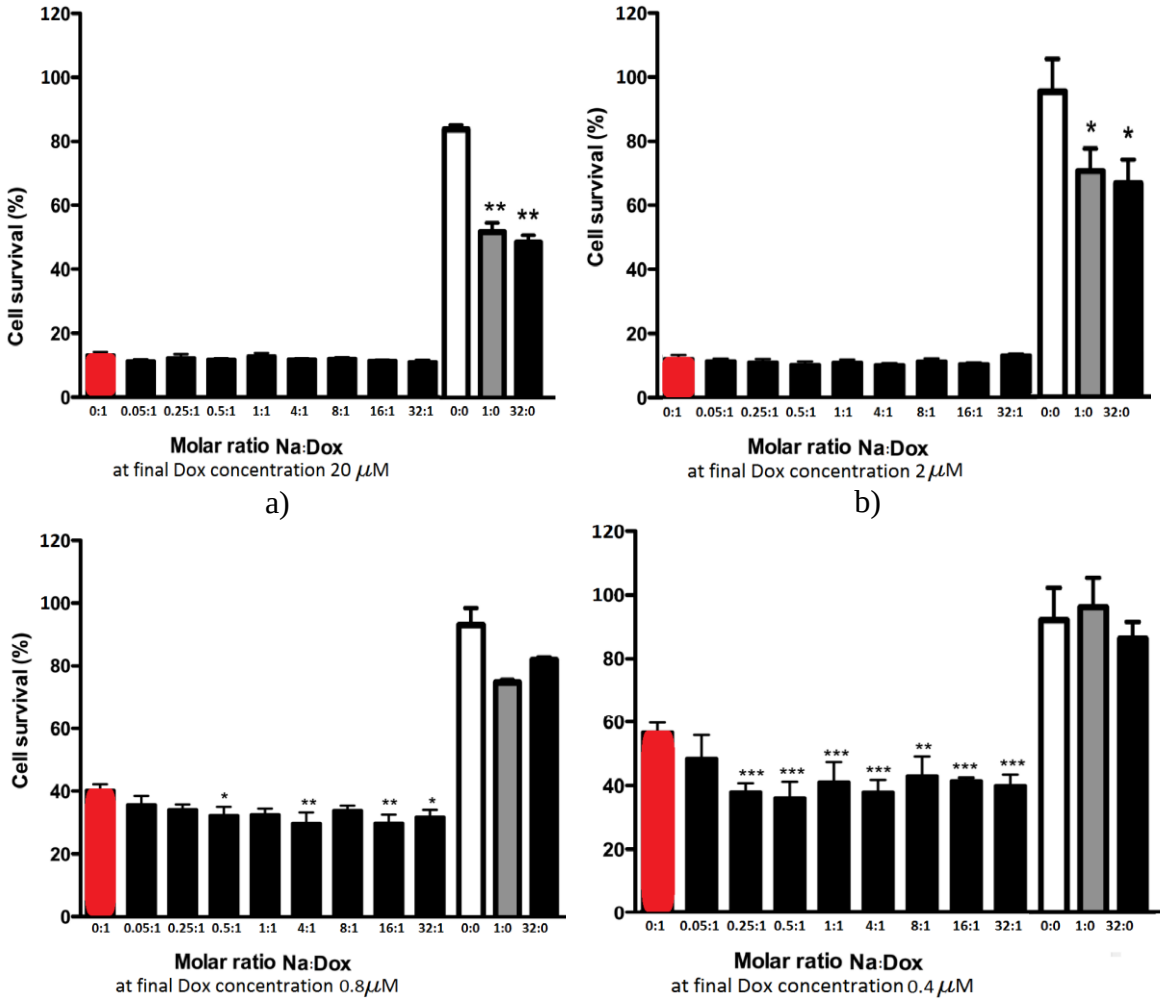

Figure 4.2: MTT assays showing the MCF7 Cell survival (%) against molar Na:Dox solutions at molar ratios 0:0 (control media without drug or Na), 0:1 (control "only Dox"), 32:1, 16:1, 8:1, 4:1, 1:1, 0.5:1, 0.25:1, and 0.05:1, 1:0 (control "only Na" at low concentration) and 32:0 (control "only Na" at high concentration). Results between were considered to have statistical significance difference at *P<0.05 and ***P<0.01. Statistical significance was evaluated between samples containing Dox and samples without Dox samples separately.

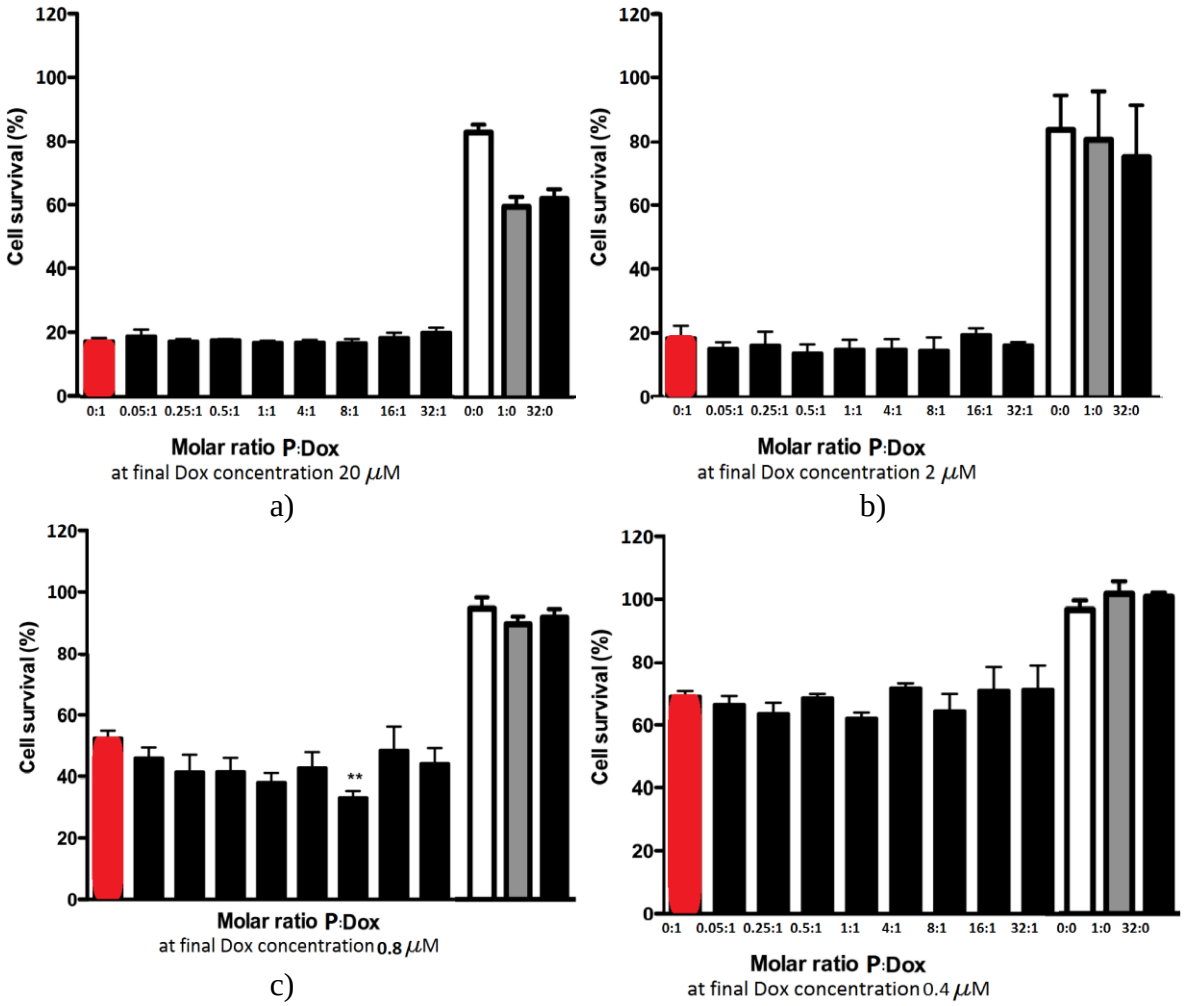

Figure 4.3: MTT assays showing the MCF7 Cell survival (%) against molar P:Dox solutions at molar ratios 0:0 (control media without drug or P), 0:1 (control "only Dox"), 32:1, 16:1, 8:1, 4:1, 1:1, 0.5:1, 0.25:1, and 0.05:1, 1:0 (control "only P" at low concentration) and 32:0 (control "only P" at high concentration). Results between were considered to have statistical significance difference at *P<0.05 and ***P<0.01. Statistical significance was evaluated between samples containing Dox and samples without Dox samples separately.'

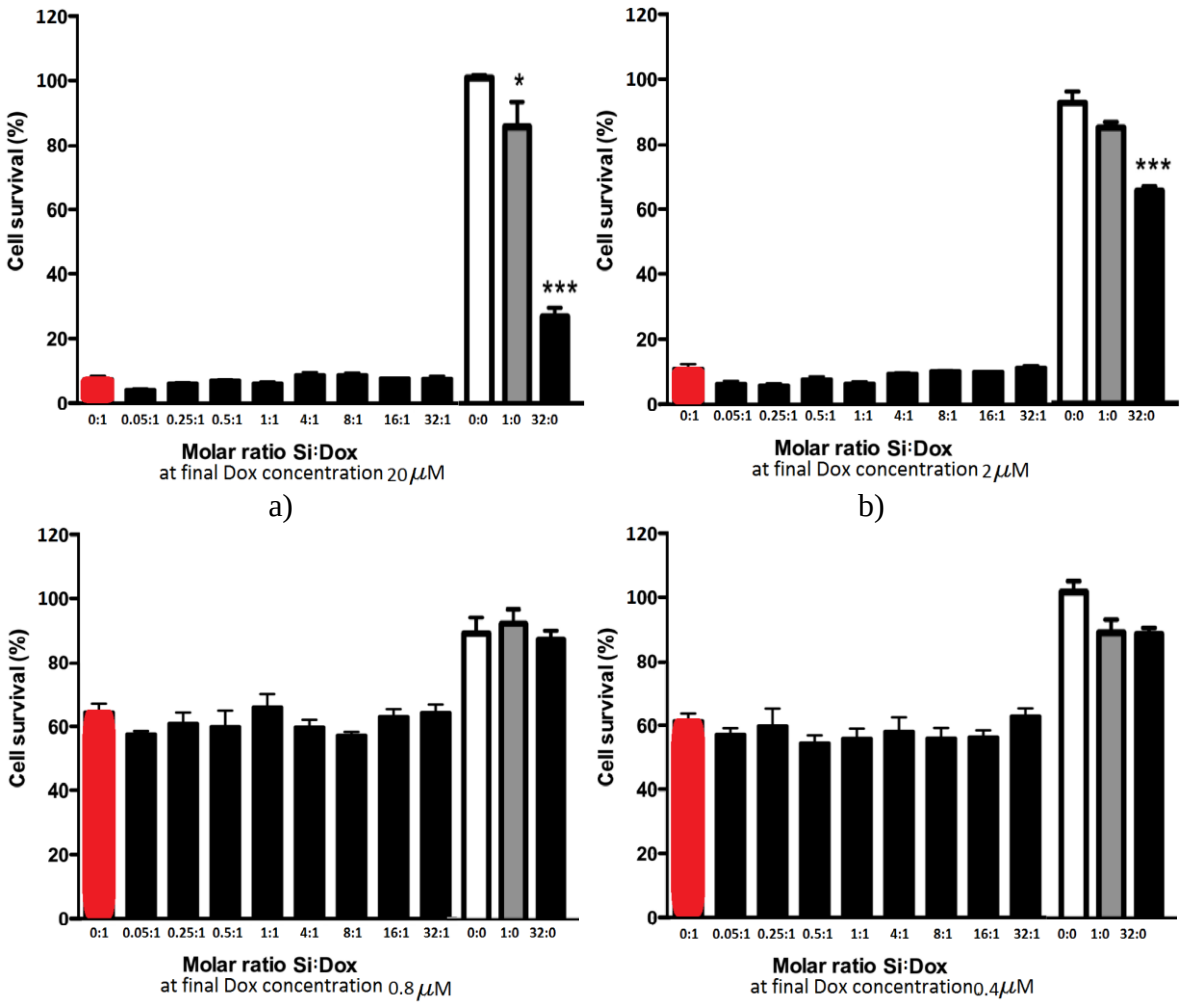

Figure 4.4: MTT assays showing the MCF7 Cell survival (%) against molar Si:Dox solutions at molar ratios 0:0 (control media without drug or Si), 0:1 (control "only Dox"), 32:1, 16:1, 8:1, 4:1, 1:1, 0.5:1, 0.25:1, and 0.05:1, 1:0 (control "only Si" at low concentration) and 32:0 (control "only Si" at high concentration). Results between were considered to have statistical significance difference at *P<0.05 and ***P<0.01. Statistical significance was evaluated between samples containing Dox and samples without Dox samples separately.

Assignments of the proton NMR chemical shifts of Dox performed using 2D COSY are showed in Figure 4.5. The three most downfield signals, one triplet and two doublets, were assigned to non-exchangeable protons of ring A. The triplet signal was assigned to proton 2H. The upfield doublet at 7.39 ppm was assigned to 3H proton, and the downfield doublet at 7.44 ppm was assigned to 1H proton. A strong single peak

appearing at 3.90 ppm had integral intensity due to three protons. These protons provided a strong NOE cross-peak to 3H proton and weak NOE cross-peak to 2H proton, and were assigned to 5H protons of the O-CH_3 group of ring D. Two pairs of strongly coupled protons were observed as doublets at 2.95 and 2.63 ppm; and at 2.26 and 2.06 ppm. The two protons that provided a cross-peak to a singlet at 4.88 ppm were assigned to 8axH (2.26 ppm) and 8eqH (2.06 ppm) of ring D. Consequently, the peak at 4.88 ppm was assigned to 7H proton. The other two protons were assigned to 10axH and 10eqH of ring D, respectively. The peak appearing at 5.46 ppm was assigned to 1'H of the sugar moiety. This proton is strongly coupled to the resonance peak at 1.99 ppm, assigned to 2'axH and 2'eqH protons. The 2'H protons are further coupled to the resonance peak at 3.69 ppm, assigned to 3'H proton. The other two strongly coupled resonances appearing at 4.24 ppm and 1.31 ppm were assigned to 5'H and 6'H protons of the CH_3 group of the sugar moiety. No signal could be definitively assigned to 4'H proton due to signal overlap. The peak at 3.86 ppm was due to two protons and was assigned to 14H protons. These protons did not give cross-peaks to any other protons in COSY spectrum as expected. All assignments are in a good agreement with those published previously [394, 395].

NMR 1D proton spectra analyses (Figure 4.6) showed that the addition of Ca, Na and P to Dox solution resulted in proton NMR isotropic shifts of the peaks characteristic for 1H, 2H and 3H protons of ring A, the 5H proton of the O-CH_3 group linked to the same ring, and the 10H and 8H linked to the ring D. It was observed that the shift of these peaks increases as P and Na concentration increases (Figure 4.6 b and c). In the case of Ca plateau was observed for Ca:Dox ratio higher than 8:1 (Figure 4.6 a). On the other

hand, no significant shift was observed when Si was added to Dox solution. (Figure 4.6 d)

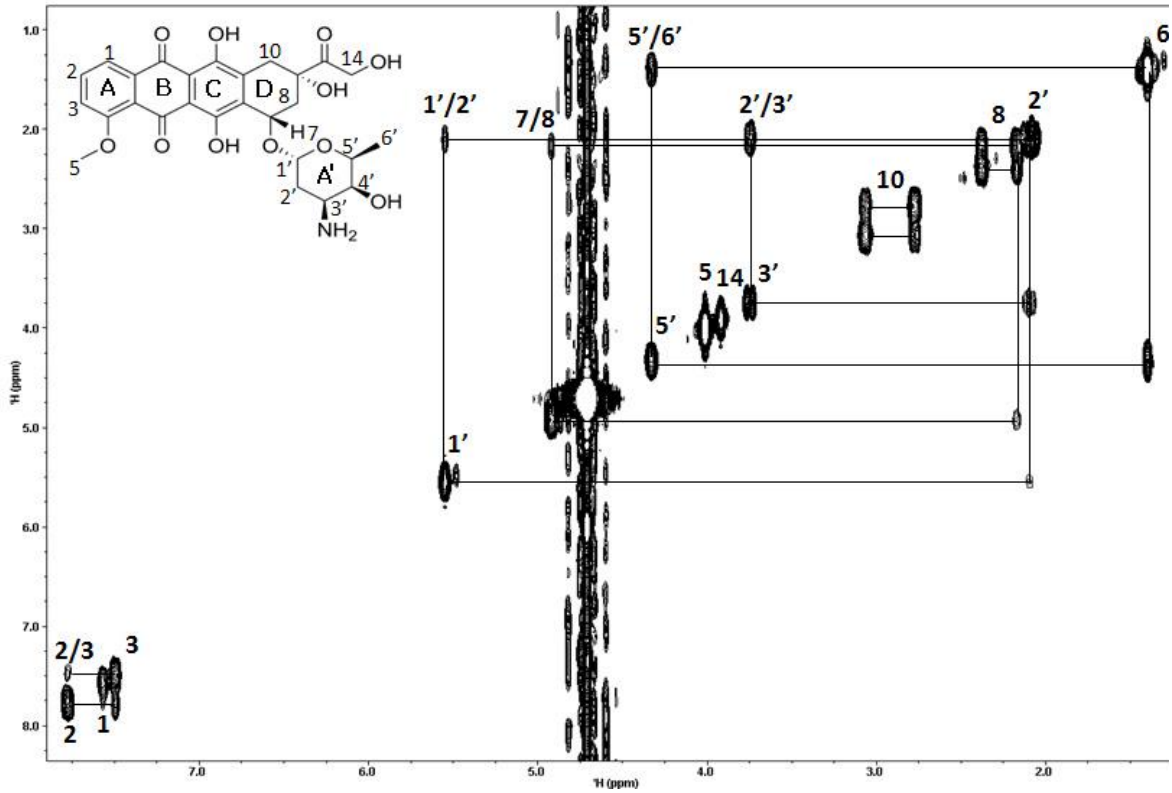

Figure 4.5: Doxorubicin molecule; protons assignment using NMR COESY

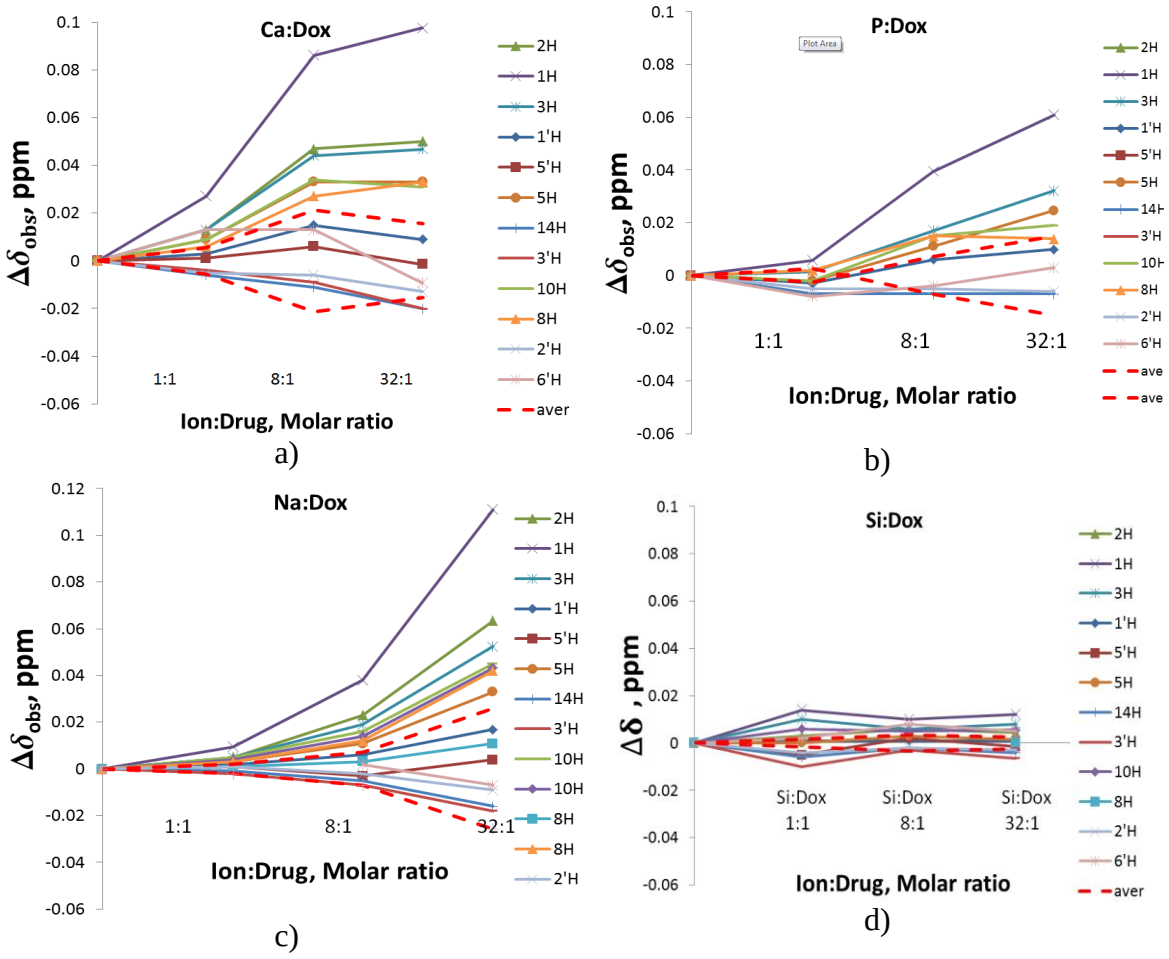

Figure 4.6: Chemical shifts detected by NMR for different complex: a) Ca:Dox, b) P:Dox, c) Na:Dox, and d) Si:Dox, at different ion:Dox molar ratios. Dashed lines (in red), in the figures, represent the trend of the average chemical shift of different protons calculated at each ion:Dox concentration. Changes in the protons chemical shift were considered significant when their values were above the red dashed line.

Table 4.1 shows the "association constants" (K_a) were calculated using NMR data and B-H linearization method for the formation of complexes Dox-Ca, Dox-Na and Dox-P.

Table 4.1: Association constants calculated using NMR data and Benesi-Hildebrand linearization method for the formation of complex Dox-Ca, Dox-Na and Dox-P. No data is presented for Si since not significant association Dox-Si was detected.

Proton	2H	1H	3H	5H	10H	8H	average	stdv
	Ca							
Ka (M^{-1})	281.2	331.44	315.75	290.98	301.73	291.5	302.1	16.93
	Na							
Ka (M^{-1})	139.85	76.19	156.09	137.03	144.22	106.23	126.6	27.14
	P							
Ka (M^{-1})	18.65	33.52	15.38	17.43	16.05	34.47	22.58	8.14

4.4. Discussion

Results of the study indicate that the kind and concentration of ions released from bioactive ceramics can alter the therapeutic effect of the released Dox. Positively charged ions of Ca^{+2} and Na^{+} showed to have the highest affinity with Dox molecules as demonstrated by the association constants obtained by NMR analyses. In contrast, negatively charged ions PO_4^{-3} and SiO_4^{-4} showed either low affinity or no significant association with Dox respectively. Cytotoxicity test on MCF7 breast cancer cells showed enhanced cytotoxicity of Dox when mixed with Ca and Na at molar ratios ion:Dox greater than 0.5:1. Furthermore, no measurable detriment of the drug bioactivity was seen by the incorporation of Ca, Na, P or Si in Dox solutions.

The high availability of functional groups (-C=O, -COOROH, -OH, -OR, $-NH_3$) within Dox molecule can lead to tautomerize from one functional group to other by changing the pH of the immersing solution [389] [390]. As such, changes in the ionic concentration of the immersing solution should be able to cause tautomerization of Dox molecules facilitating drug ion binding. NMR results of Dox mixed with Ca and Na showed isotropic shifts of the protons signals corresponding to the assigned ring A and D (Figure 4.5). This suggested that the metal ions interact with the beta-ketophenolate site

of the Dox molecule as indicated in Figure 4.7. Wei et. al., reported the binding of Dox with positively charged Yb^{3+} ions on the same site on the Dox molecule [396]. Moreover, the same protons, those assigned to the ring A and D, in Dox molecule are affected by the presence of negative ions. Therefore, further hydrolysis reactions are required to make possible the interaction of negatively charged molecules with the same molecular site, which is in agreement with the lower affinity between negative ions and the drug.

In vitro cytotoxicity tests against MCF7 cell line demonstrated that the presence of ionic dissolution products of SCPC does not affect the bioactivity of the anticancer molecule. Solutions tested at final Dox concentration greater than 2 μM were highly toxic and did not show significant variations in the % of cell survival regardless the presence of Ca, Na, P or Si. At lower final Dox concentration 0.8 and 0.4 μM, only Ca and Na improved the mortality of the MCF7 cells at ion:drug molar ratios higher than 0.5:1. In fact, control samples with Ca or Na without Dox did not affect the % of cells survival, confirming that the increase in the mortality of MCF7 cell should be by the Dox-ion interactions. Rose et. al., reviewed the effect of Ca^{2+} concentration [Ca^{2+}] on the permeability of in Chironomus salivary gland cell junction. Authors reviewed high permeability of the cell membranes was observed for Ca concentration [Ca^{2+}]$<10^{-7}$M, allowing the permeability of large peptide molecules of about 1,200–1,900 molecular weight. Moreover, they also reported that at [Ca^{2+}]$>5x10^{-5}$ M permeability falls drastically restringing the permeation for all molecular species including the small inorganic ions [397]. These suggest that rather than an ion-cell membrane mechanism, an ion-drug interaction is enhancing the bioactivity of Dox.

NMR and cytotoxicity tests allowed estimate interactions of Dox with SCPC dissolution products. The association constant "Ka" calculated for Ca was more than double that of Na and 15 times higher than that of P indicating that Ca is the most active ion interacting with Dox. However, dissolution-back precipitation reactions on SCPC surface limit the amounts of Ca in solution due to the continuous formation of apatite layer. Therefore, interactions between Dox and Ca^{+2} eluted from SCPC are not expected. On the other hand, due to the high elution of Na^{+} and the back precipitation of Ca^{+2}, Dox-Na bonding is expected to be more feasible than Dox-Ca bonding. Besides, dissolution of Si and P should not be a concern because of their low affinity with the Dox molecule.

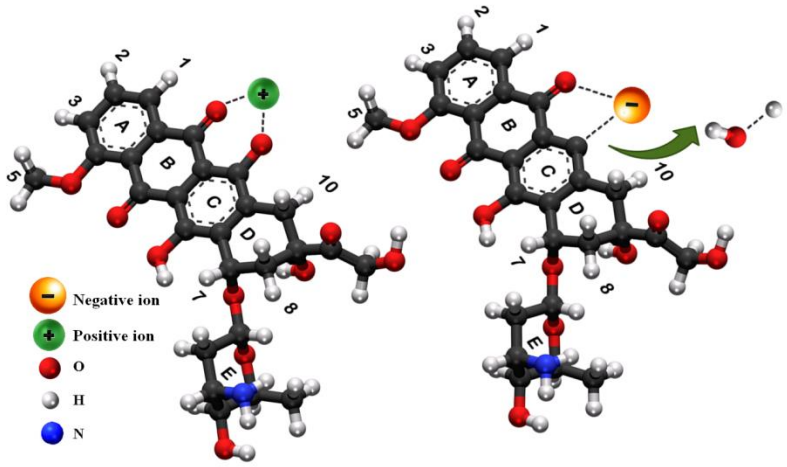

Figure 4.7 Schematic showing Doxorubicin molecule based on its crystal structure. NMR results suggested that positive (green) and negative (yellow) ions interact with the beta-ketophenolate site of the drug.

4.5. Conclusion

NMR results showed the binding between Dox and SCPC dissolution products. Positive ions Ca, Na showed the major affinity with the drug, while negative ions P and Si showed low or negligible affinity with Dox. Cell culture tests demonstrated that the interactions between the SCPC dissolution products and the released drug did not cause measurable adverse effects on the bioactivity of the tested drug. Therefore, it opens the possibility of use SCPCs with different composition for the delivery of the anticancer drug.

CHAPTER 5: A SILICA-RICH SCPC FOR DRUG DELIVERY SYSTEM FOR THE TREATMENT OF HEPATOCELULLAR CARCINOMA (HCC): IN VIVO STUDY.

5.1. Introduction

Hepatocellular carcinoma (HCC) ranks as the fifth most common cancer diagnosed in the world and the third leading cause of cancer-related mortality [398]. Current treatment for those diagnosed with HCC most commonly relies on surgical intervention (resection, transplant, or ablation). While potentially curative, these approaches are often compromised by late detection, the underlying liver disease associated with tumor development (cirrhosis), tumor location within the liver, intra- or extra-hepatic metastasis, and a lack of transplantable organs [399]. Chemotherapy for HCC, including localized transarterial chemoembolization (TACE), is similarly limited by late detection, advanced disease stage, and the etiology of the hepatic tumor [399, 400]. Chemotherapeutic approaches can also be further compromised by the presence of hepatic cirrhosis and diminished liver function, the liver being the primary site of drug metabolism [399, 400].

The failure to develop effective HCC treatment strategies has led to increased interest in the development of drug delivery systems (DDS) to provide increased, site-specific concentrations of cytotoxic agents. Nanoparticles of various biomaterials, including polymers[401], ceramics [379, 402], metals [403], and composites [404], have been tested as a means of effecting localized drug release while decreasing acute side effects. While these approaches have promise there are also potential problems to be

considered. For example, intravenous nanoparticle injection carries the risk of unfavorable interactions with the reticuloendothelial system [405]. Similarly, nano-size particles have the potential to cause harmful interactions with biological tissue(s) and trigger responses that affect cell metabolism and phenotype, including the potential to act as mutagens [406]. For example, Hussain *et al*., reported the use of metal/metal oxide nanoparticles led to changes in cell morphology and decreased mitochondrial function, membrane leakage, glutathione, and mitochondrial membrane potential in BRL3A (liver) cells [407]. Similarly, Lin, *et al*. report concentration dependent toxicity, including lipid peroxidation and membrane damage, for crystalline silica nanoparticles in lung cancer cells [408].

In addition to nanoparticles, calcium phosphate [409]and polymethyl methacrylate (PMMA) [410]have been tested as DDSs in the treatment of cancer. Unlike nanoparticles these agents are typically loaded with drug and implanted inside the tumor, or placed adjacent to it. While such approaches avoid many of the non-specific effects associated with nanoparticles, drug release kinetics are often limited by the rate of DDS degradation. As such, increased drug retention by the DDS can occur due to the inherent chemical stability of the material *per se* [409, 410].

Previous studies by our group reported the release kinetics of Cisplatin from SCPC75 in vitro. Results showed that diffusion and interfacial dissolution-back precipitation reactions controlled the release of the drug. Furthermore, following the release from the SCPC75, Cisplatin remained cytotoxic in hepatoma cells in culture [380]. The aim of the current study was to analyze bonding between Cisplatin molecules

and SCPC75 and determine the effect of SCPC75-Cis hybrids on HCC progression in vivo.

5.2. Materials and Methods.

5.2.1. Assurances

Male ACI rats (175-225g; Harlan Inc., Indianapolis, IN) were used for these studies. All experiments were approved by the Institutional Animal Care and Use Committee and conformed to The Guide for the Care and Use of Laboratory Animals.

5.2.2. SCPC75–Cis Hybrid Preparation

The SCPC75 (with chemical composition in molar percentage: 32.9% SiO_2, 11.4% P_2O_5, 22.8% CaO, and 32.9% Na_2O) was prepared by sintering, at 800^oC for 1 hour. The ceramic was ground and sifted to a final particle size range 250-425μm, and particles were immersed in simulated body fluid (SBF) at a ceramic/solution ratio of 33mg/mL (24-Hrs, 37^oC). The SCPC75 was collected, dried, and loaded with Cisplatin by immersion in 10mg/mL Cisplatin (cis-dichlorodiamineplatinum II, Sigma-Aldrich, St. Louis, MO)-DMSO solution under continuous shaking (120rpm, 37^oC, 48 h), and 80mg of SCPC75-Cisplatin hybrid (SCPC75-Cis) were pressed into discs (5x3mm) at 360MPa. Control SCPC75 discs in the absence of Cisplatin were prepared in parallel [380].

The amount of Cisplatin loaded onto discs was determined by submerging SCPC75-Cis hybrids in 70% nitric acid (24-Hrs, room temperature [RT]) and then centrifugation (5000xg, 3 min, RT). The supernatant was collected and analyzed for platinum (Pt) concentration by Inductively Coupled Plasma-Optical Emission Spectrometer (ICP-OES; Optima 3000, Perkins Elmer). The remaining pellet was placed

in 70% nitric acid, and the process repeated three times, or until no more Pt was detected. Total Cis-loading to SCPC75 was calculated as cumulative Pt measured by ICP-OES.

5.2.3. Surface Chemistry

SCPC75-Cis hybrids or control SCPC75 (pre-immersed in DMSO without Cisplatin) were analyzed using FTIR in the diffuse reflectance mode. The spectra were collected after 200 scans at $2cm^{-1}$ resolution employing a Nicolet 6700, spectrophotometer equipped with a deuterium triglycine sulfate (DTGS) detector (ThermoNicolet, Madison, WI). The peak's position and area were measured for three different samples of each group using OMNIC software, and the results expressed as mean ± SD. Second derivative criterion and deconvolution of the spectra in the ranges from $800\text{-}1200cm^{-1}$ and $1300\text{-}1600\ cm^{-1}$ were used to resolve hidden peaks and a Gaussian model was used to fit the resolved peaks within these ranges.

5.2.4. Ceramic Morphology and Crystalline Structure

The morphology of the SCPC75 particles was analyzed using a scanning electron microscope (SEM; JEOL USA Inc, Waterford, VA) in the secondary electron mode. Porosity and pore size distribution of the SCPC75 particles were analyzed by mercury intrusion porosimetry using an AutoPore 9500 penetrometer (Micromeritics, Norcoss, GA). The specific surface area was determined by Brunauer, Emmett and Teller (BET) single point using a high-speed N_2 gas sorption analyzer (TriStar II 3020 V1.03, Micromiretics, GA) [411]. SCPC75-Cis hybrids and unloaded controls were also analyzed by SEM using back scattering electron detection (BSE). Energy dispersive X-ray (EDX) analysis was performed to determine the presence of Pt on SCPC75-Cis hybrids. The crystalline phases were identified by X-ray diffraction (XRD) analysis using

X'pert PRO diffractometer (PANalytical, Westborough, MA) with Copper radiation (λ=1.54059 Å) at room temperature (45KV and 40mA). The XRD patterns were taken over the 2-theta range of 15-55^{o}, with a step size of 0.02^{o} and 1-sec/step. Diffraction data was analyzed by the Rietveld refinement method using X'Pert HighScore Plus. Error indices (statistical R factors) lower than 10 were considered acceptable Rietveld criteria.

5.2.5. Cell Culture and Animal Model of HCC

Rat H4IIE cells were purchased from ATCC (Bethesda, MD) and maintained in culture as previously reported [412]. Bilateral sub-cutaneous (*s.q.*) H4IIE cell inoculations (2x10^{6} cells) were performed into the left and right flanks of animals under isofluorane anesthesia. Animals were allowed to recover, and tumor size was measured daily. This method results in a reproducible tumor mass that is readily visible to the naked eye (7-8 days post-inoculation) and grows to 10-12mm in diameter within 14-d of inoculation [413].

5.2.6. Tumor Treatment with Cisplatin

Animals were randomized to one of 5 groups; control (untreated; C), systemic Cisplatin (sCis), blank (no drug) SCPC75 disc (SCPC75), SCPC75-cisplatin hybrid placed adjacent to the tumor mass (ADJ-SCPC75-Cis), or SCPC75-cisplatin hybrid placed within the tumor mass (IT-SCPC75-Cis). Control animals (C) were injected (*i.p.*) with DMSO (0.1mls) twice daily, 7-d after H4IIE cell inoculation. Systemic Cisplatin (sCis) treated animals were injected (*i.p.*) with Cisplatin dissolved in DMSO (0.1ml total volume; 3mg/ml) twice daily beginning 7-d after H4IIE cell inoculation. For ADJ-SCPC75-Cis placement, animals were placed under surgical anesthesia and a skin incision made approximately 10-12mm from the tumor mass. Blunt dissection was

performed to separate the skin from the fascia; SCPC75 tablets were immersed briefly in PBS, and placed under the skin immediately adjacent to the tumor. Tumors were randomized to receive either SCPC75 or SCPC75-cisplatin hybrids.

For animals randomized to IT-SCPC75-Cis discs, rats were placed under surgical anesthesia and a skin incision made approximately 10-12mm from the tumor. Blunt dissection was performed up to the tumor site and a sterile scalpel blade used to make a 3-4mm incision across the surface of the tumor. SCPC75 tablets were immersed briefly in PBS, and gently pushed into the incision. Gentle pressure was applied to the site, and the skin closed using 4-0-vicryl suture.

5.2.7. Measurement of Physiological Function and Systemic Toxicity

As an indicator of health animals were monitored daily for behavior (alert, grooming, feeding) and weight change. In accordance with veterinary advice, weight loss ≥15% was considered a humane endpoint. At experimental conclusion blood was collected by cardiac puncture under surgical anesthesia and aspartate aminotransferase (AST; liver function), creatinine and blood urea nitrogen (BUN) (renal function), and base excess and bicarbonate levels (metabolic function) were measured (Diagnostic Laboratory, Carolinas Medical Center, Charlotte, NC).

5.2.8. Tumor Resection and Processing

At euthanasia tumor masses were resected, photographed, measured, and tumor volume calculated. The SCPC75 disc was removed, wiped clean of surface blood-debris, and stored in a sterile 1.5mL tube. Hepatic, renal, and tumor tissues were divided into ≈100mg pieces and placed in either neutral buffered formalin (histology), or snap-frozen in liquid nitrogen (Cisplatin-platinum content).

5.2.9. Histological Analysis

Formalin-fixed, paraffin-embedded tissue was cut into 5μm sections, dried onto glass slides, deparafinized with xylene, and hydrated through graded alcohol into water. Sections were stained with hematoxylin and eosin (H&E), necrotic area identified in 5 random fields, and necrotic area calculated as a percentage of the section surface area (ImageJ software, NIH, Bethesda, MD). To determine apoptotic cell death, a terminal deoxynucleotidyl transferase UTP nick end labeling (*TUNEL)* assay was performed and slides counterstained with 4', 6-diamidino-2-phenylindole (DAPI) for nuclear localization [414].

5.2.10. Measurement of Platinum Content

Platinum concentration was measured using ICP-OES (Optima 3000, Perkins Elmer). For each sample, ~75mg of tissue was digested in 750μl 70% nitric acid (1-Hr, RT), and centrifuged (20,000×g, 20 min, RT). The supernatant was collected, diluted 1:20 in deionized water and analyzed by ICP-OES. Platinum content on SCPC75-Cis hybrids after treatment was determined using the same methods and ICP-OES analysis as used to determine initial loading, and data were expressed as the percentage change compared to initial loading.

5.2.11. Statistical Analysis

The data were expressed as the mean ± SD. Statistical analyses were performed following the procedure indicated in section 2.2.7.

5.3. Results

5.3.1. Microstructural Analysis of SCPC75 Particles

SEM analyses of the SCPC75-Vanc-rhBMP2 hybrid particles (Figure 5.1 a) demonstrated a uniform distribution of nanopores throughout the surface of the particle (inset). The porosity and surface area of the SCPC75 particles as determined by mercury intrusion porosimetry were found to be 64.28% and 13.53 m^2/g, respectively. BET analysis, another complimentary method, indicated that the surface area was 7.21m^2/g. A bimodal pore size distribution with sharp maxima in the pore size range of 10-650 μm, and a broad band corresponding to pores in the size range of 4 nm-5 μm were observed (Figure 5.1b).

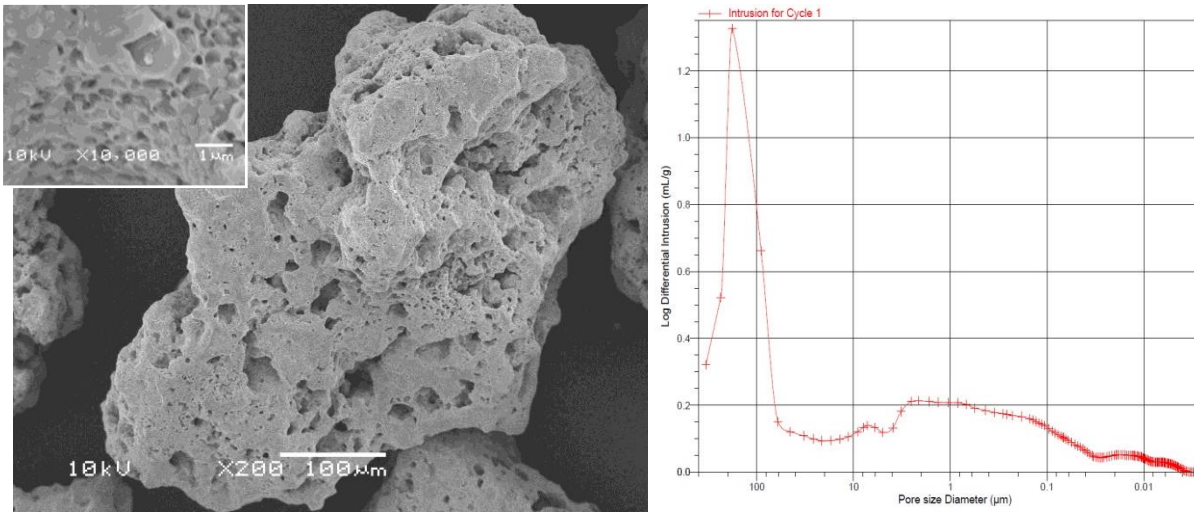

a) b)

Figure 5.1: a) SEM micrograph of SCPC75 particle taken at 200X and 10000X (Inset) showing interconnected micro and nano pores. b) Pore size distribution profile for SCPC75 showing bimodal pattern including a sharp peak centered around 100 μm and a broad peak for nanometer pores

XRD analysis demonstrated the crystal size of the SCPC75 ceramic was 10-30nm. This is in agreement with previously reported TEM data that showed the crystal size to be ≈50nm [415]. The Rietveld R-factor were: "*profile*" (Rp) = 9.95, ''*expected" (Rexp)* =

9.6, and ‘‘weighted profile” (Rwp) = 10.15.Table 5.1 reports the calculated phase composition for SCPC75 after refinement.

Table 5.1: Phase composition and structural parameters of SCPC75 obtained by the Rietveld refinement on the corresponding XRD diffraction patterns.

Sample	Crystalline Phases Content (%)	Space Group (ICSD)	Crystallite Size (Å)
SCPC75 with 78.44% of crystallinity	55.0% β Rhenanite	Pna21	251.5
	11.8% alpha-quartz	P 31 21	202
	1.1% SiP_2O_7	P121/c1	254
	27.9% $CaNa_2SiO_4$	P213	117.3
	4.2% α-Cristobalite	P12/c1	187.9

5.3.2. SCPC75-Cisplatin Loading and FTIR Analyses of Cisplatin-SCPC75 Functional Group Interaction

ICP-OES analysis demonstrated that, prior to implantation; Cisplatin was bound to the SCPC75 at 14.2 ± 0.2mg Cisplatin/g SCPC75. FTIR analysis of SCPC75 was measured prior to and after Cisplatin binding (Figure 5.2) and signal assignments on the spectra were identified (Table 5.2). Second derivative criterion and deconvolution of the spectra in the ranges 800-1200 cm^{-1} and 1300-1600 cm^{-1}, together with the Gaussian-fitted resolved hidden peaks were recorded (Fig 2a-d). The presence of Cisplatin on the surface of SCPC75 was confirmed by identification of bands at 1486 cm^{-1} and 789 cm^{-1}, corresponding to bending and rocking modes of the N-H group (Fig 2a and c). In association with drug binding to the SCPC75 ceramic four main changes in the FTIR spectra were documented including: (1) the disappearance of the bands at 517.1, 642.4, 674.8, 944.6, 1462.6 cm^{-1} corresponding to O-P-O(H) bending, OH stretching of hydroxyapatite (HA), Si-O of the six-member ring of hydroxyapatite stretching and CO_3^{-2} vibrational modes respectively (2). The appearance of Cisplatin bands centered at 788.9,

1436.7, 1486.4 and 1645.5 cm^{-1} on the SCPC75-cis loaded spectra (Figure 5.3) (3). The increase in the area under the peaks at 1153.6-1214.6, 1408 cm^{-1}, and 1084 cm^{-1} corresponding to P-O (H) bending mode. (4) The decrease in the area under the peaks at 871.2, 961.9 and 1060.4 cm^{-1} corresponding to C-O carbonate vibrational mode, Si-O stretching and Si-O-Si stretching.

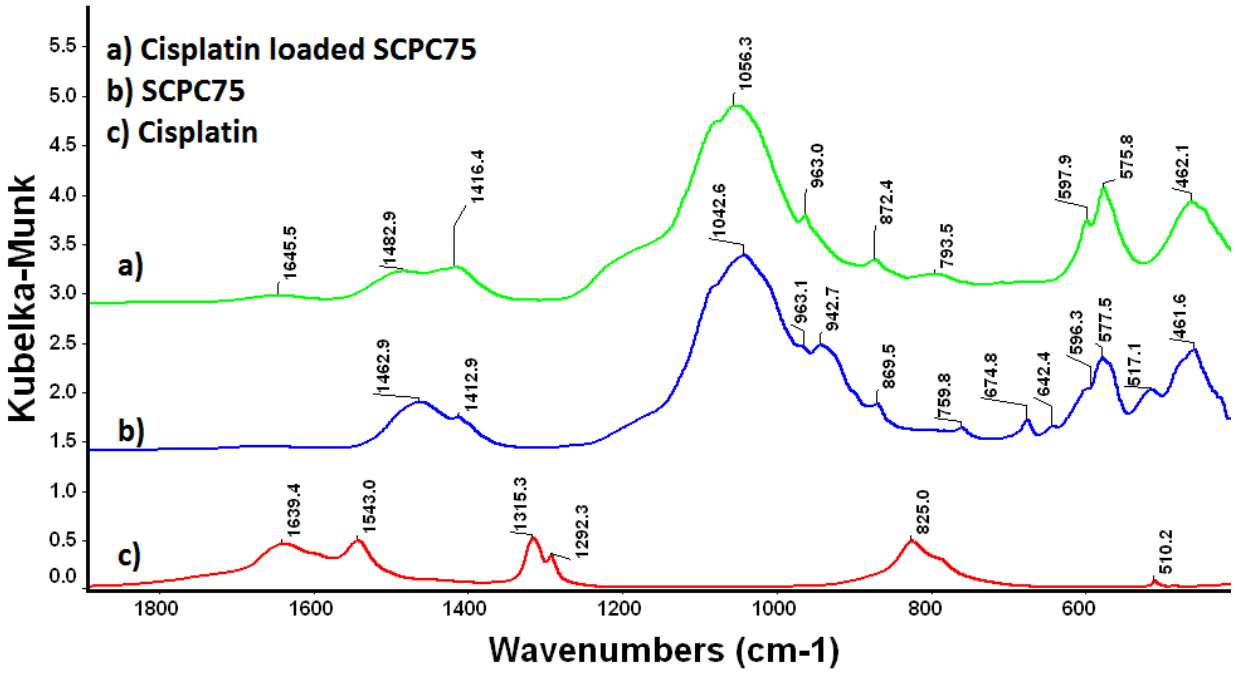

Figure 5.2: Representative FTIR spectra of SCPC75 loaded with Cisplatin (SCPC75-Cis), SCPC75 without Cisplatin (SCPC75) and Cisplatin (Cis).

Table 5.2: FTIR Peak Assignment forSCPC75 prior to and after Cisplatin loading.

Characteristic bands	Wavenumber (cm^{-1})				
	Assignment	SCPC75 control		SCPC75-cisplatin hybrid	
		Peak position	Peak Area	Peak position	Peak Area
Rocking mode Si-O-Si	460 [336]	460.7	17.4	462	17.6
O(H) bending mode	528 [341]	517.1	6.6		0
O-P-O bending mode	567, 603 [416]	577.4, 597.8	11.8, 5.2	575.6, 596.3	11.9, 6.2
OH stretching for Hydroxyapatite	631 [416]	642.4	1.1		0
Silica six-member rings	~ 700 [417]	674.8	1.4		0
P-O-P bending	~780 [340]	758.9	0.5	759.8	0.6
N-H rocking mode	~810 [418]		0	788.9	1.8
C-O carbonate vibrational mode	~860 [295]	871.4	3.1	871.2	1.4
P-O(H)stretching	891 [341]	895.6	1.4		0
Si-O-H stretching	~950 [336]	944.6	2.5		0
PO_4^{-3} stretching vibrations	980, 1040, 1100 [340]	964.9,1005.6, 1041.5, 1084.6	11.1, 23.0, 33.6, 33.7	961.9, 1008.4, 1044.8, 1081.9	7.3, 21.2, 21.0, 38.7
Si-O-Si stretching	1025, 1050 [340]	1058.6	0.6	1060.4	0.3
Asymmetric Si-O-Si stretching	1120-1162 [295]	1123.7	3.9	1122.6	0.9
P-O(H) bending mode (shoulder)	1190-1213 [341]	1152, 1193	5.4, 2.3	1153.6, 1214.6	14.2, 3.3
P=O stretching	1300-1450 (broad) [341]	1375.4	1.3	1376.6	1.4
P-O-H bending	1406 [338]	1411.7	1.2	1408	5.3
CO_3^{-2} asymmetric stretching	1413- 1470 [416]	1462.6	19.9		0
N-H vibrations	1472, 1460 and 1445 [419]		0	1436.7, 1486.4	2.6, 14.5
H2O bending	1660-1600 [340]	1642.5	1.2	1646.7	0.6
NH_3 asymmetric bending	1657 , 1627 [418]		0	1644	3.4

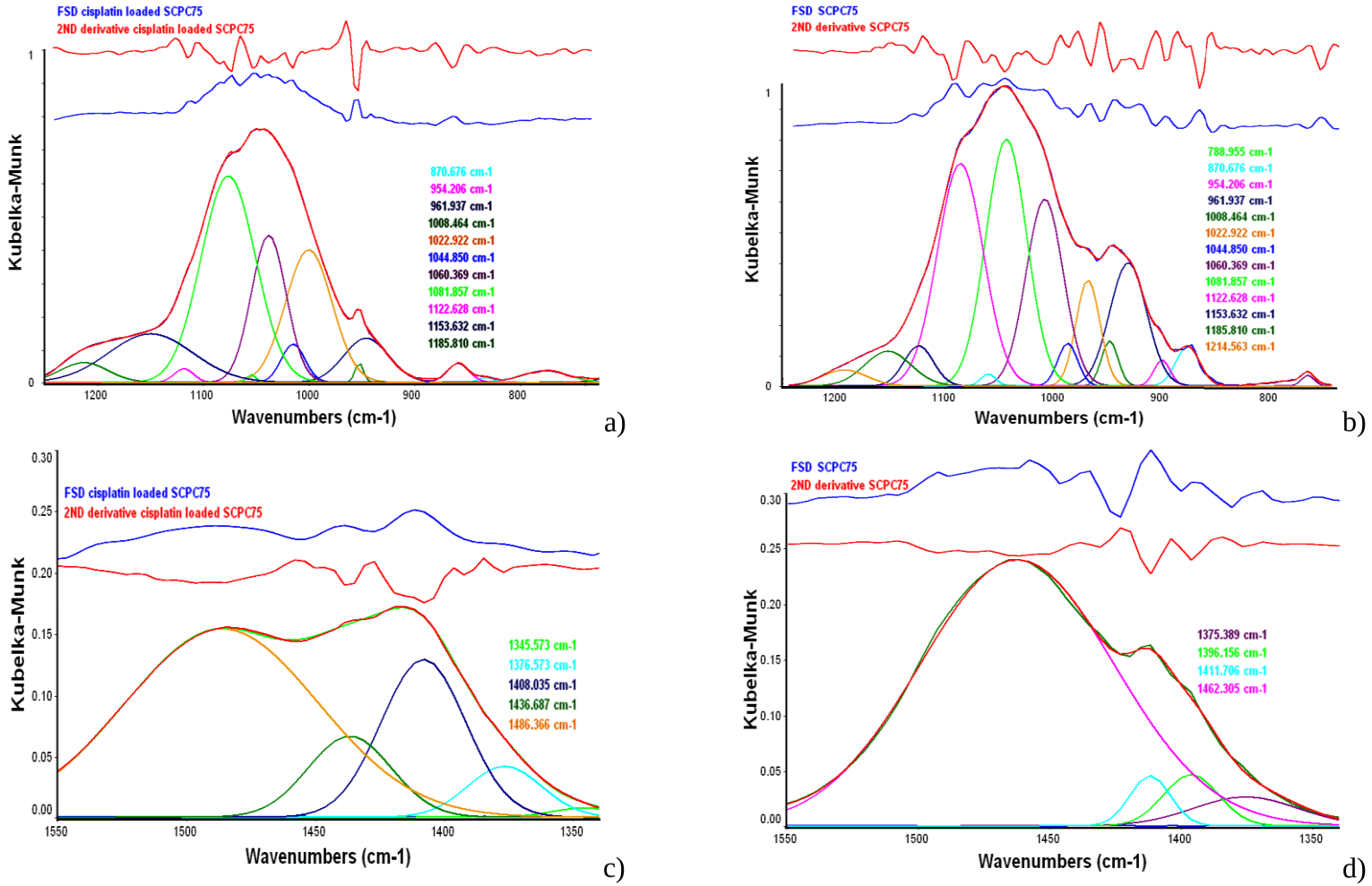

Figure 5.3: Gaussian peak fitting, normalized to the highest peak intensity, and base line corrected FTIR spectra of SCPC75 Cisplatin loaded (a and c) and SCPC75 without Cisplatin (b and d). Fourier self-deconvolution and second derivative (on the top of each spectrum) were taken as criteria for spectral band positions and bandwidth.

5.3.3. SEM-EDX Surface Analyses and Cisplatin Loading

Using SEM in SE mode the SCPC75 was analyzed prior to, and following, immersion in SBF (24-Hrs, 37^{o}C). This approach revealed an interconnected porous structure, pores being in the range of 1µm-100µm (Figure 5.4a). Noticeable changes in the SCPC75 were seen after its immersion in SBF. These changes were attributed to the precipitation of the Ca-P layer due to the bioactivity of the material and confirmed by FTIR spectra (Figure 5.4 b). Nevertheless, interconnected pore structures in the µm-nm range were maintained following SBF immersion (Figure 3 b). Analysis of SCPC75-Cis hybrids by SEM in BSE mode demonstrated approximately even drug distribution on the disc surface (Figure 5.4 c-d), the brighter spots detected representing the presence of Pt/Cisplatin, an effect confirmed by EDX analysis (Figure 5.4 e-f, Figure 5.3).

Table 5.3: EDX analysis of presence or absence of Pt on the surface of unloaded and Cisplatin-loaded SCPC75 discs

Element	Weight (%)	
	Spectrum 1	Spectrum 3
O	32.35	14.67
Na	18.47	25.09
Si	15.16	2.62
P	10.45	1.75
S	5.05	6.73
Cl	11.67	5.75
Pt	6.85	43.39
Total	100	100

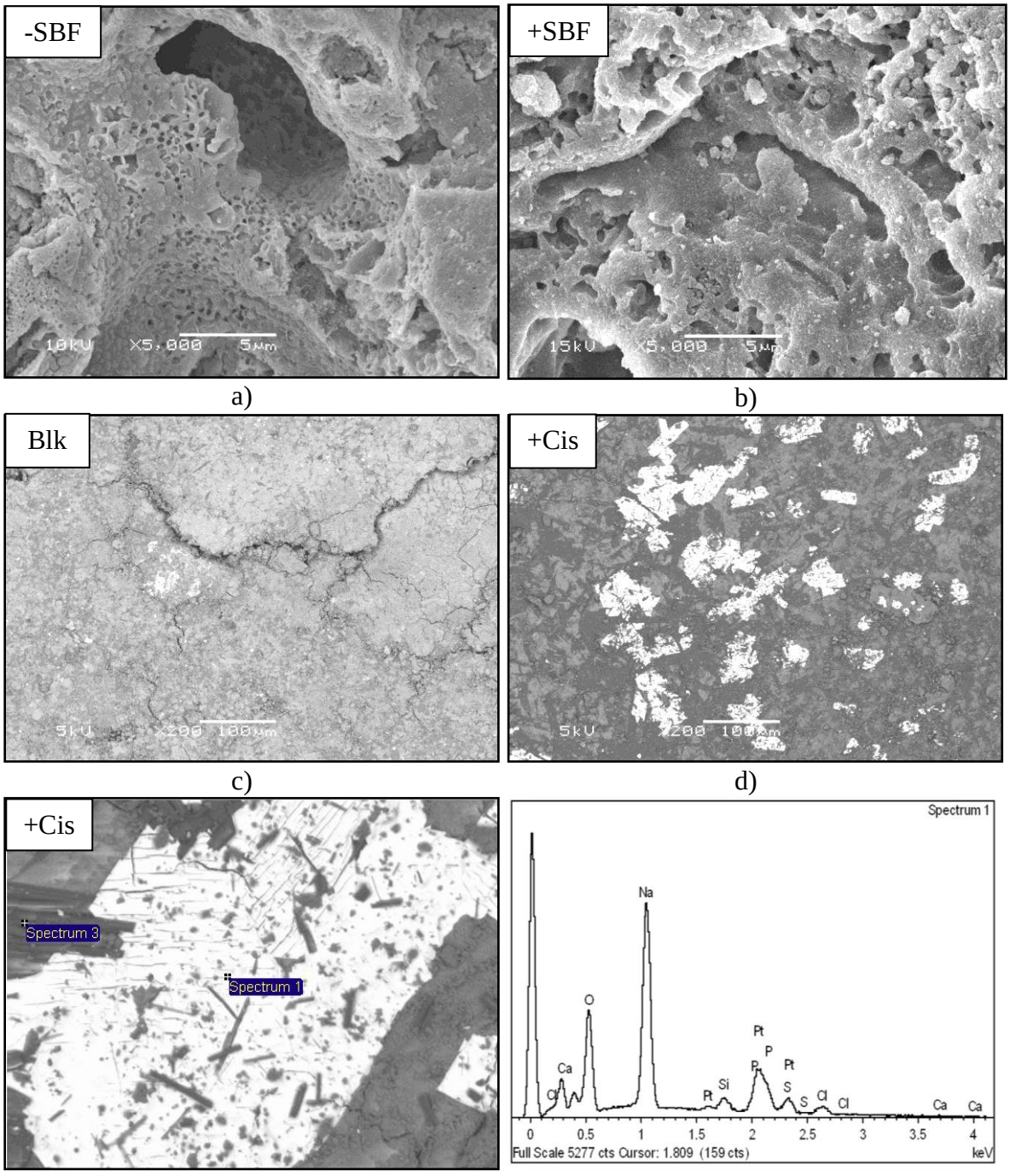

Figure 5.4: (a and b) Representative SEM images illustrating SCPC75 microstructure prior to (-SBF) and after (+SBF) immersion in simulated body fluid (SBF). (c and d) Representative SEM images in back scattering mode of unloaded, blank SCPC75 discs and Cisplatin-loaded SCPC75 discs (+Cis). (e) Representative EDS illustrating the presence of platinum on the disc surface through analysis of highlighted spectra.

5.3.4. Tumor Formation and SCPC75 Implantation

Subcutaneous inoculation of H4IIE hepatoma cells (~$2x10^6$) leads to reproducible focal tumor mass formation in ACI rats. Using a bilateral inoculation approach tumor masses grew to ≈10-12mm in diameter 14-d post-inoculation (Figure 5.5a). To determine the viability of IT- and ADJ-SCPC75-Cis placement, and tolerance to the SCPC75 disc *per se*, preliminary experiments were performed in which "*blank*" SCPC75 discs were used. Tumor masses and SCPC75 discs were readily visible by X-ray (Figure 5.5b), and upon completion of the research (14-d) tumor dissection and disc recovery was performed (Figure 5.5 d).

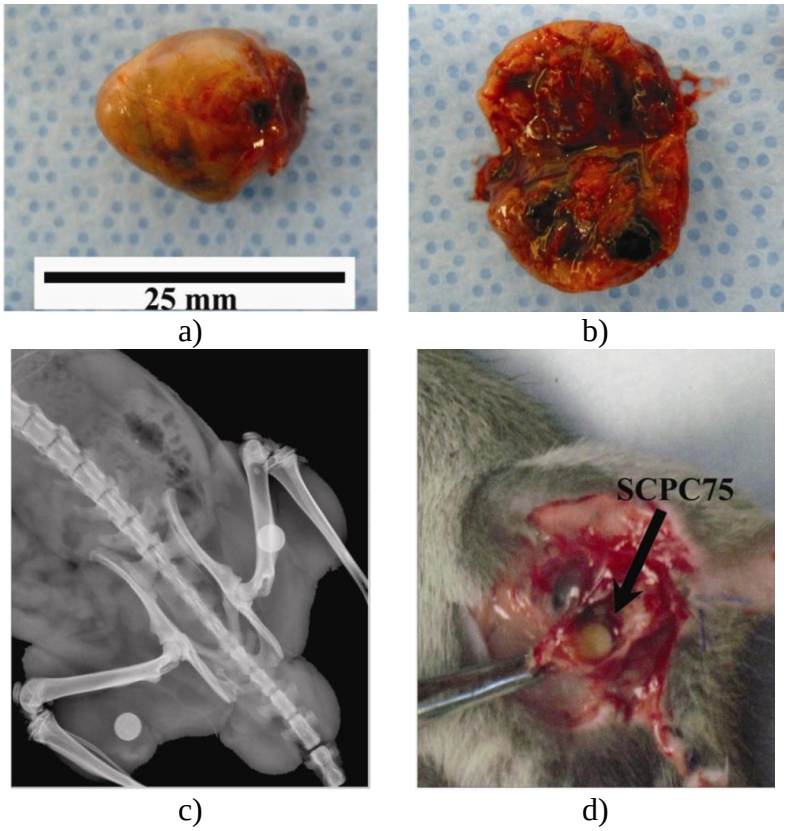

a) b)

c) d)

Figure 5.5: a) Example of a subcutaneous tumor mass forming 14-d post-subcutaneous (s.q.) inoculation of H4IIE hepatoma cells. b) Image showing a cross section of the tumor mass. c) X-ray image illustrating successful implantation of SCPC75 discs (s.q.) in rat model of tumor formation. d) Image illustrating SCPC75 disc following 7-d implantation.

5.3.5. Effect of Route of Cisplatin Administration on Tumor Progression

Animals in which H4IIE cells had been inoculated were randomized to control (untreated; C), blank SCPC75 disc (SCPC75), systemic Cisplatin (sCis), ADJ-SCPC75-Cis), or IT-SCPC75-Cis (n=5 per group). In control animals, normal tumor growth occurred over the 5-d experimental period (Figure 5.6a). Animals treated with sCis (3mg/Kg, i.p. twice daily) did not demonstrate significant differences in tumor size as compared to control counterparts (Figure 5.6 a). In contrast animals treated with SCPC75-Cis hybrid discs, placed either adjacent to or within the forming tumor mass demonstrated significantly slower tumor growth as compared to both control and sCis treated animals (Figure 5.6b, n=5 per group, *$p<0.05$ *versus* C and sCis). No significant difference in tumor size was detected between tumors treated with SCPC75-Cis hybrid discs when placed adjacent compared to within the tumor mass (Figure 5.6b, n=5 per group). Tumors treated with blank SCPC75 discs without drug were not significantly different compared to untreated tumor growth (Figure 5.6 b, n=5 per group).

Analysis of tissue necrosis demonstrated little or no detectable tissue necrosis in untreated, control tumors (C; Figure 5.7a). Small areas of necrotic cell death (≤5% of the total area) were detected in animals receiving sCis, levels that were not significantly different to those seen in tumors in which blank SCPC75 discs were placed adjacent to the tumor mass (~4-6% necrotic area, Figure 5.7a). In contrast, highly significant areas of tissue necrosis were observed in tumors receiving ADJ-SCPC75-Cis or IT-SCPC75- Cis treatment (n=5 independent fields/sample, n=5 per group, $p<0.01$ ADJ-SCPC75-Cis and IT-SCPC75-Cis *versus* all other groups). No significant difference was measured

between necrotic area in animals treated with ADJ-SCPC75-Cis and IT-SCPC75- Cis (Figure 5.7c).

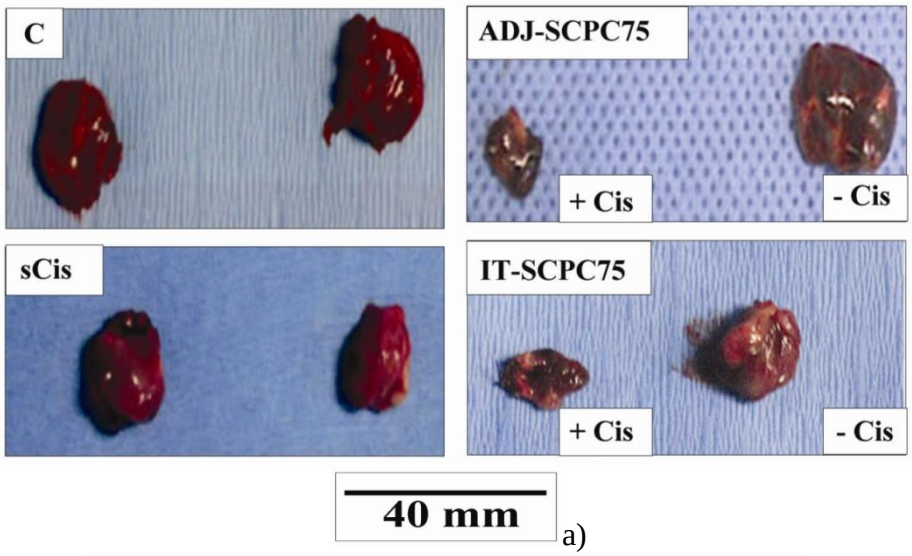

a)

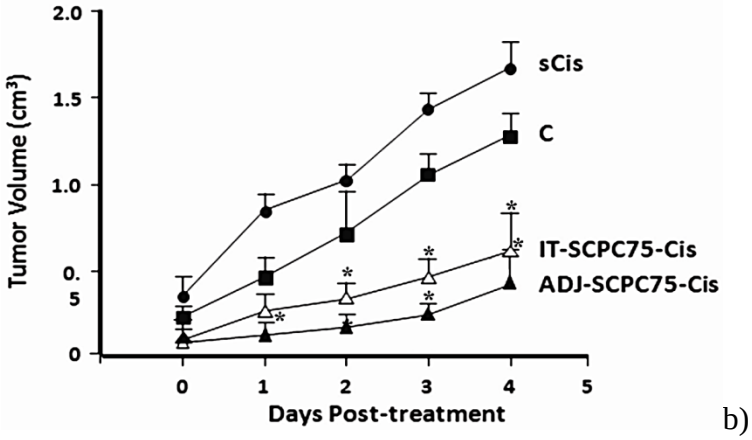

b)

Figure 5.6: a) Representative images of resected tumors from control (C; untreated) and animals treated with systemic Cisplatin (sCis), ADJ-SCPC75, or IT-SCPC75. +Cis = tumors forming in loaded SCPC75 discs. –Cis = tumors forming in unloaded SCPC75 discs placed in opposite flanks. b) Sequential measurement of tumor volume in untreated (C), sCis treated, or SCPC75-Cis treated animals. *$p<0.05$ *versus* C, n=5 per group.

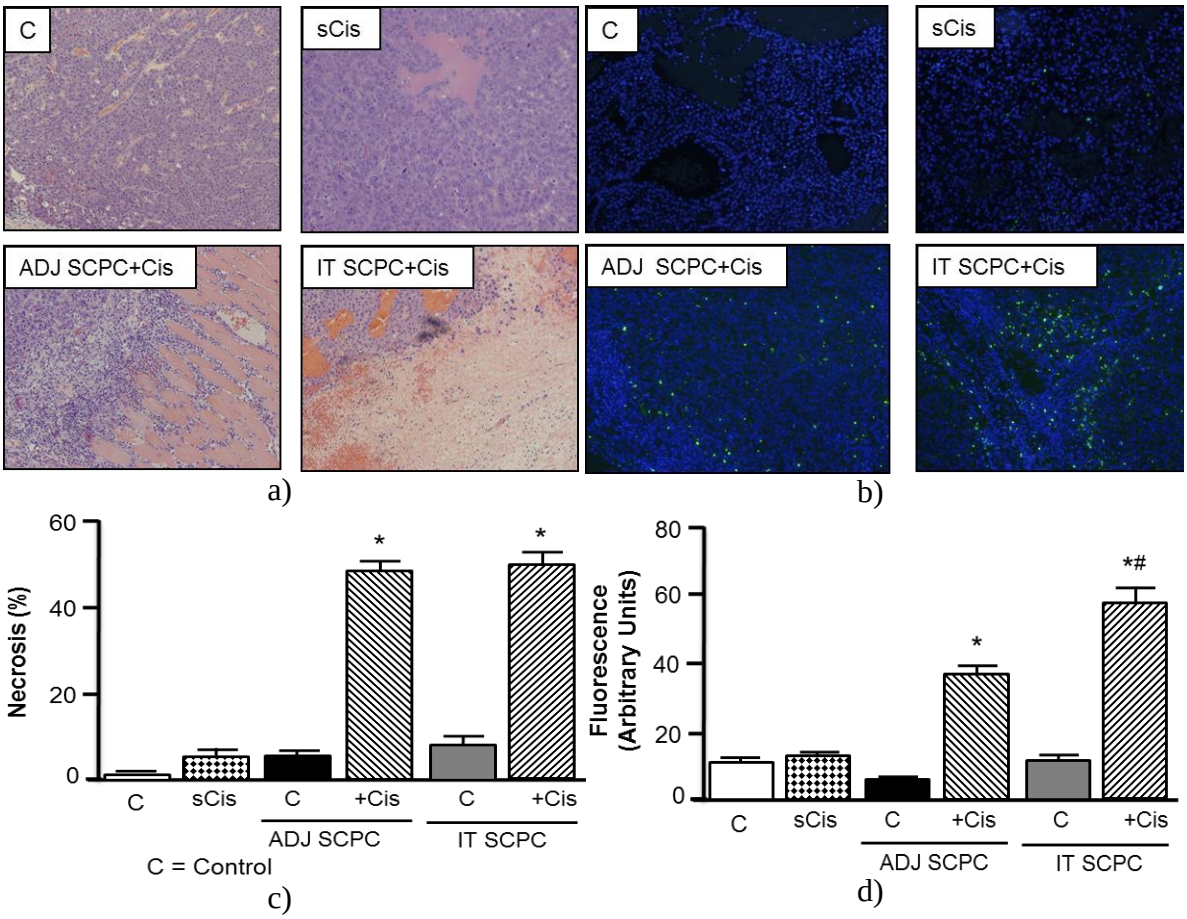

Figure 5.7: a) Representative H & E images of sectioned tumor masses from untreated control (C), systemic Cisplatin treated (sCis), or animals treated with SCPC75-Cis hybrids placed adjacent (ADJ) or within (IT) the tumor mass (upper panels). b) Percentage necrotic area/field; ADJ-SCPC75 and IT-SCPC75 are unloaded SCPC75 discs. *p<0.05 *versus* C, n=5 per group. c) Representative *TUNEL* images (apoptotic bodies appear green and cell nuclei blue) of sectioned tumor masses from C, Cis, ADJ-SCPC75-Cis or IT-SCPC75-Cis animals (upper panels). d) Cumulative analysis of apoptotic bodies/field. *p<0.05 *versus* C, #p<0.05 IT-SCPC75-Cis *versus* ADJ-SCPC75-Cis, n=5 per group.

To define apoptotic cell death, a TUNEL assay was performed. This approach demonstrated no significant difference in apoptotic bodies measured between C, sCis, ADJ-SCPC75, or IT-SCPC75 groups (Figure 5.7b). In contrast, significantly increased apoptotic bodies were measured in ADJ-SCPC75-Cis and IT-SCPC75-Cis treated animals compared to all other groups (Figure 5.7b, n=5 independent fields/sample, n=5 individual experiments, p<0.05 ADJ-SCPC75-Cis and IT-SCPC75-Cis *versus* all other

groups). Finally, significantly increased apoptotic bodies were detected in IT-SCPC75-Cis compared to ADJ-SCPC75-Cis treated animals (Figure 5.7 d, n=5 independent fields/sample, n=5 individual experiments, $p<0.05$ ADJ-SCPC75-Cis *versus* IT-SCPC75-Cis).

5.3.6. Route of Cisplatin Administration and Effect on Systemic Physiology

Sequential animal body weight measurement demonstrated no significant changes during the experimental course between untreated control animals (C) and animals receiving either blank SCPC75 discs (data not shown) and animals receiving ADJ-SCPC75-Cis or IT-SCPC75-Cis treatment (Figure 5.8a). In contrast, animals treated with systemic Cisplatin (sCis; 3mg/Kg, *i.p.* twice daily) exhibited rapid, significant decreases in body weight (Figure 5.8 a, n=5 per group, $p<0.01$ sCis *versus* all other groups).

To determine toxicity associated with Cisplatin administration we measured markers of liver (AST), kidney (creatinine and BUN), and metabolic function (base excess and bicarbonate levels). Animals treated with SCPC75-cisplatin hybrids, either ADJ-SCPC75-Cis or IT-SCPC75-Cis, exhibited AST levels not significantly different to control (C; untreated) animals (Figure 5.8 b, n=5). In contrast, animals treated with systemic Cisplatin (sCis) exhibited significantly higher AST levels compared to all other groups (Figure 5.8 b, $p<0.05$ sCis *versus* all other groups, n=5 independent experiments). Markers of renal function (creatinine and BUN) also demonstrated significantly elevated levels in sCis treated animals compared to all other groups (Figure 5.8 c-d, $p<0.05$ sCis *versus* all other groups, n=5 independent experiments). Conversely, markers of normal metabolic function (base excess and bicarbonate) demonstrated significantly decreased

levels, demonstrating diminished metabolic function, in sCis treated animals compared to all other groups (Figure 5.8 e-f, $p<0.05$ sCis *vs.* all other groups, n=5 per group).

5.3.7. Effect of Route of Cisplatin Administration on Drug Distribution

At experiment conclusion SCPC75-Cis hybrids were recovered from the site of placement. Gross observation revealed discs were approximately equal in size compared to pre-placement, and dry weight analysis demonstrated a net 18 ± 4% reduction in SCPC75-Cis weight compared to pre-placement weight. Analysis of platinum (Cisplatin) content demonstrated *in vivo* SCPC75-Cis placement led to approximately 55% of the loaded Cisplatin to be released (Figure 5.9a). Placement of the disc adjacent to or within the tumor mass did not significantly affect total Cisplatin released (Figure 5.9 a).

Serum and tissues from control animals (C), and animals treated with systemic (sCis) or SCPC75-Cis hybrids (ADJ-SCPC75-Cis or IT-SCPC75-Cis), were analyzed for platinum/Cisplatin content. These data demonstrated no differences in serum platinum concentration in animals treated with ADJ-SCPC75-Cis or IT-SCPC75-Cis hybrid discs as compared to control (Figure 5.9b, n=5 independent samples assayed in duplicate). In contrast, we detected significantly increased levels of platinum in sCis treated animals compared to all other groups (Figure 5.9b, n=5 independent samples assayed in duplicate, $p<0.05$). We next analyzed platinum content in tumor tissue. These data demonstrated, as expected, no detectable levels of platinum in serum of untreated animals. In contrast animals treated with both sCis and ADJ-SCPC75-Cis hybrid exhibited significant, detectable levels of platinum compared to control (Figure 5.9 c, n=5 independent samples assayed in duplicate, $p<0.05$). We did not detect significantly different amounts of platinum between tumors treated with either sCis *versus* ADJ-SCPC75-Cis hybrid

(Figure 5.9c). Conversely, IT-SCPC75-Cis treatment led to significantly increased intratumoral platinum of an order of magnitude greater than other treatment groups (Figure 5.9c, $p<0.05$ IT-SCPC75-Cis *versus* sCis and ADJ-SCPC75-Cis hybrid).

Analysis of hepatic and renal platinum levels demonstrated significantly higher levels of platinum in both liver and kidney tissue from animals receiving sCis compared to other treatment groups (Figure 5.9d, and Figure 5.9 e and D, $p<0.05$ sCis *versus* ADJ-SCPC75-Cis and IT-SCPC75-Cis). While not significantly different, we also noted that animals treated with IT-SCPC75-Cis trended toward higher hepatic and renal platinum levels than the ADJ-SCPC75-Cis (Figure 5.9d, and Figure 5.9e).

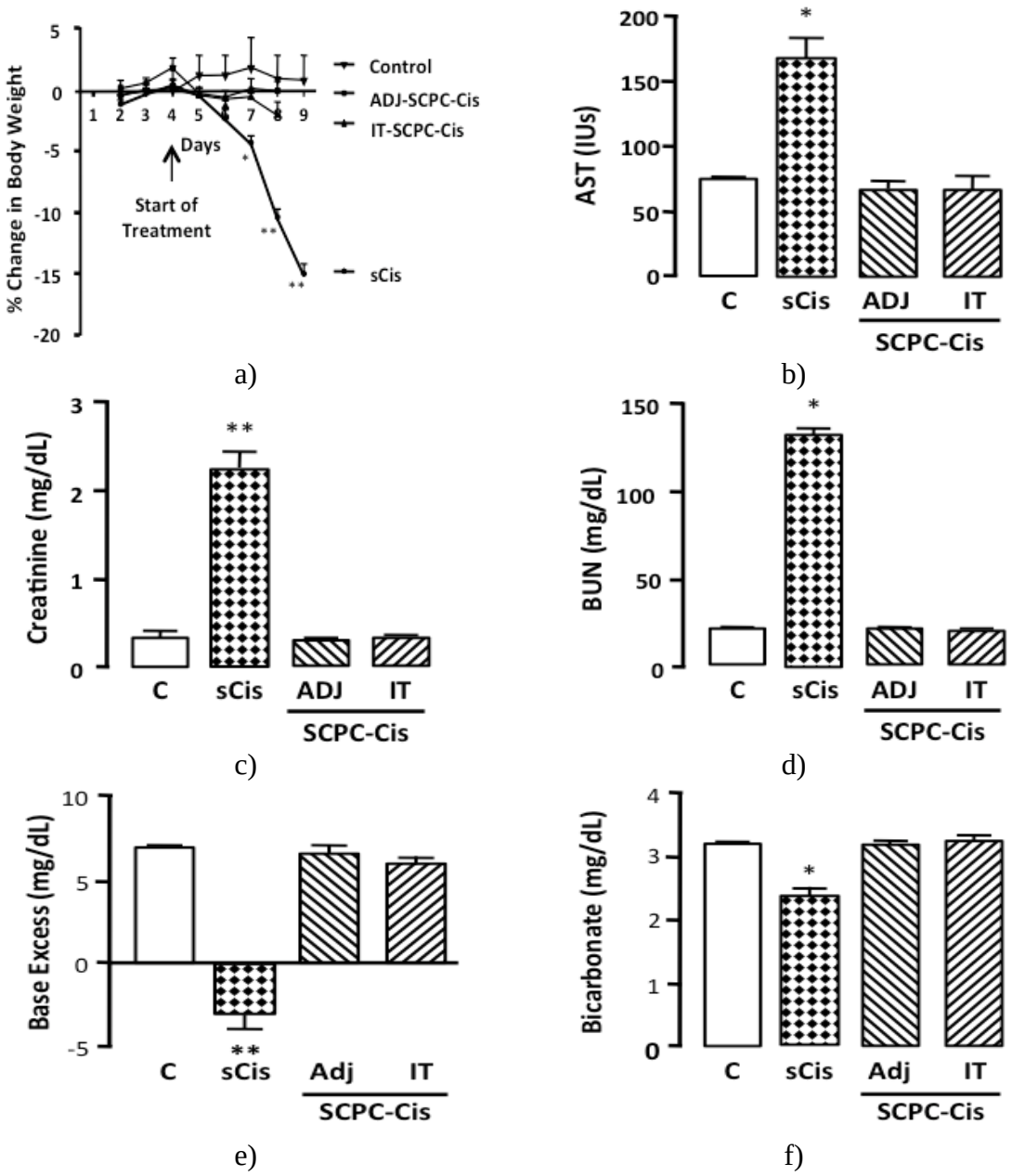

Figure 5.8: a) Change in body weight during tumor formation for untreated (C), systemic Cisplatin treated (sCis), or animals treated with SCPC75-Cis hybrids placed adjacent (ADJ) or within (IT) the tumor mass. *p<0.05 *versus* C, **p<0.001 *versus* C, n=5 per group. b) Aspartate aminotransferase (AST) levels in C and sCis, ADJ-SCPC75-Cis, and IT-SCPC75-Cis treated tumor-bearing animals. *p<0.05 *versus* C, n=5 per group. c). Creatinine and d) blood urea nitrogen (BUN) levels in C and sCis, ADJ-SCPC75-Cis, and IT-SCPC75-Cis treated tumor bearing animals. *p<0.05 *versus* C, n=5 per group. e). Base excess and bicarbonate levels in C and sCis, ADJ-SCPC75-Cis, f) and IT-SCPC75-Cis treated tumor bearing animals. *p<0.05 *versus* C, n=5 per group.

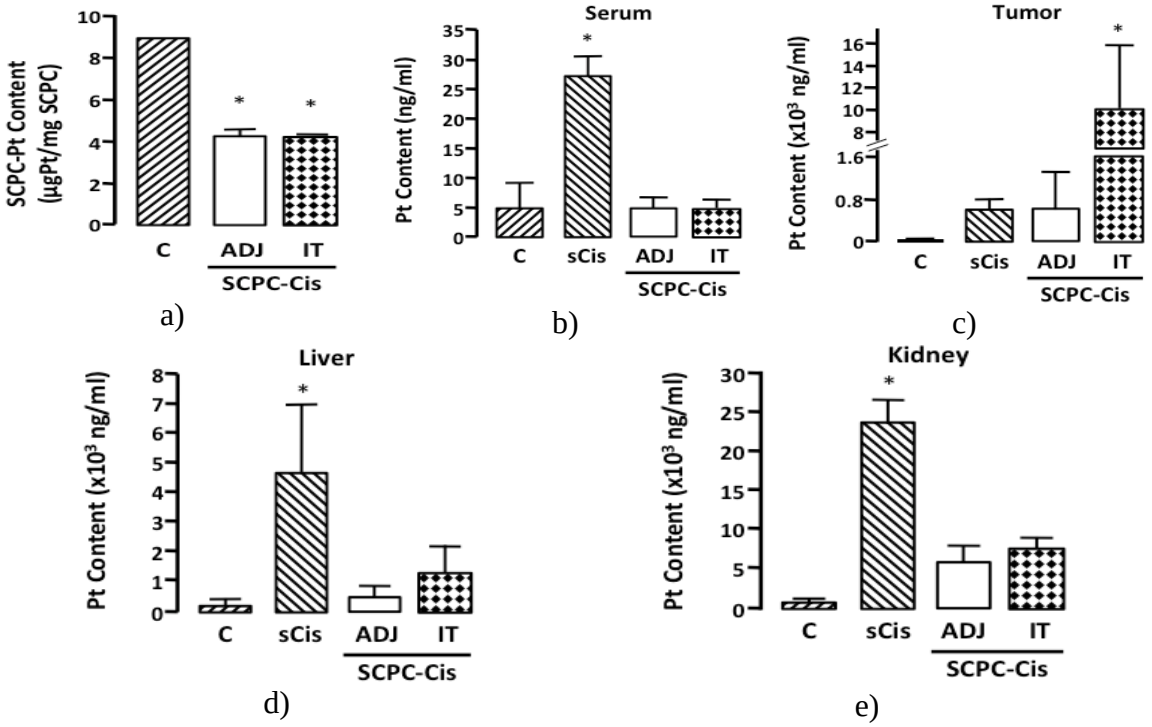

Figure 5.9: a) Percentage change inSCPC75 platinum (Pt) content prior to (C) and after implantation adjacent to (ADJ) or within (IT) a tumor mass.*p<0.05 *versus* C, n=5 per group. Relative Pt content measured in b) serum, c) resected tumor tissue, d) liver, and e) kidneys of untreated tumor-bearing animals (C), or animals treated with systemic Cisplatin (sCis), or SCPC75-Cis hybrids placed adjacent (ADJ) or within (IT) tumor masses. *p<0.05 *versus* C.

5.4. Discussion

In the present study, we have shown that engineered Si-rich SCPC75 has the potential to serve as a vehicle for the sustained release of therapeutic doses of Cisplatin. FTIR analyses demonstrated that P-O functional groups of SCPC75 chemically bind Cisplatin to the highly porous surface of the ceramic scaffold. We are conscious that compacting particles to discs at 360 MPa significantly limits the contact between the inner nanopores surface and surrounding fluids, complicating the diffusion of drug molecules entrapped inside the discs. Therefore, the hierarchic porosity and the controlled dissolution of the Si-rich SCPC (SCPC75) assisted the release kinetics, plus significantly increased drug loading capacity per unit of ceramic mass. The chemical bonding of Cisplatin to the SCPC75 surface regulated the release of ≈55% of total drug loaded drug within 5-days. Analysis of the drug-release from the scaffold 5-days post-implantation indicated that drug release occurred predominantly *via* diffusion.

FTIR analyses revealed a consistent shift in the peaks characteristic of the N-H of Cisplatin to the lower wavenumber values indicating an increase in the conjugated momentum of the bond vibration modes and suggesting chemical bonding with the functional groups on the SCPC75 ceramic surface (Figure 5.2). The chemisorption of the drug molecules was associated with the disappearance of bands corresponding to O-H functional groups of the ceramic including O-P-O(H) bending mode, OH stretching for hydroxyapatite, P-O(H) stretching and Si-O-H stretching (Figure 5.2, and Figure 5.3). The disappearance of these bands indicates that the hydrated phosphate and silicate functional groups are the SCPC75 active sites that link Cisplatin to the SCPC75 scaffold according to the following steps. Dissolving Cisplatin in DMSO results in a solvolysis

reaction [420] where Cl^- ions are replaced by DMSO molecules forming positively charged species:

$$Pt(NH_3)_2Cl_2 + DMSO \rightarrow Pt\text{-}(NH3)_2\ Cl(DMSO)^{+1} + Cl^- \qquad \text{Equation 5.1}$$

The positively charged drug species are attracted to the ionized SiO_4^{-4} and PO_4^{-3} ionic groups on the SCPC75 ceramic surface according to the following Equation 5.2 and Equation 5.3:

$$Pt\text{-}(NH_3)_2^{+2} + 2O\text{-}P\text{-}O(H) \rightarrow (O\text{-}P\text{-}O)_2\ \text{-}Pt\text{-}(NH_3)_2 \qquad \text{Equation 5.2}$$

$$Pt\text{-}(NH_3)_2^{+2} + 2O\text{-}Si\text{-}O(H) \rightarrow (O\text{-}Si\text{-}O)_2\ \text{-}Pt\text{-}(NH_3)_2 \qquad \text{Equation 5.3}$$

Wallin, *et al.*, demonstrated that the interaction of the ammonia to silanol groups is significantly weaker than that to the Pt [421]. These Cisplatin interactions with active sites on the surface of SCPC75 are illustrated in Figure 5.10.

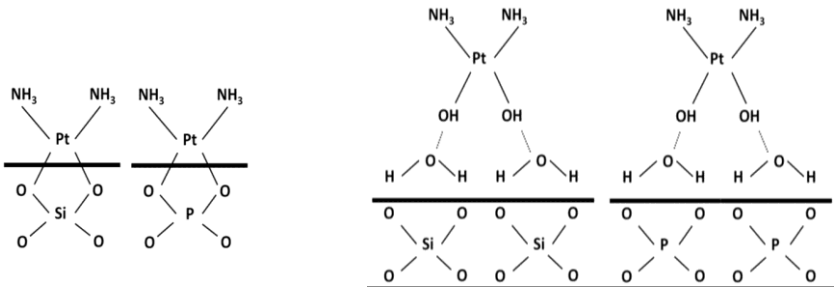

Figure 5.10: Possible linkages of Cisplatin on the surface of SCPC75, based on FTIR data.

The data presented herein demonstrate SCPC75-Cis hybrid scaffolds significantly reduced rate of tumor progression in an animal model of HCC in the absence of adverse systemic effects. Overall, treatment with SCPC75-Cis hybrids reduced tumor volume by ~65-70% compared to animals treated with systemic Cisplatin. However, animals treated with systemic Cisplatin exhibited marked signs of systemic toxicity, effects not observed in SCPC75-Cis hybrid treated groups. These data correspond to higher Cisplatin levels in the serum, kidneys, and liver of animals treated with systemic Cisplatin compared to

those treated with SCPC75-Cis. Conversely animals treated with SCPC75-Cis hybrids were characterized by significantly higher intratumoral Cisplatin than those treated with systemic Cisplatin.

In a previous work by Horcada, *et al*., the adsorption and release of ibuprofen loaded on mesoporous silicate MCM-41 (Mobile Crystalline Material) was regulated by modifying the silanol terminal groups on the carrier surface with different organic groups. As a result, the carriers in which surfaces were modified using the most polar organic groups almost doubled the drug absorbed as compared to those modified with less polar groups, due to the chemisorption of the carboxylic acid of ibuprofen *via* hydrogen bond formation. Besides, electrostatic interactions between the carboxylic acid of ibuprofen and the most polar samples contributed to reduce significantly the drug release rate [422]. Other studies also report that chemically binding of the drug to the scaffold alters the drug release kinetics in the initial stage [423]. A continuing challenge for drug-carrier scaffolds as DDS relates to the amount of drug retained on the scaffold. For example, analysis of a calcium phosphate cement matrix reports ~40% Cisplatin elution after 7 d *in vitro*, a level that increase to only 62% after 4 weeks [409]. Using the SCPC75 we reported ~60% Cisplatin release after 5-d, data that correlate well with the 55% drug elution measured 5-d post-placement *in vivo*. Of note, the low mass loss of SCPC75-cis discs (<20%) compared to amount of drug eluted, indicates drug release kinetics is mainly diffusion controlled [380].

Cisplatin eluted from SCPC75-Cis hybrids retained cytotoxic properties and induced cell death in tumor cells *in vivo*, the net effect of which was to reduce significantly the tumor progression. In comparison, animals treated with systemic

Cisplatin received significantly higher total Cisplatin treatment over the same 5 d protocol (3mg/Kg/day, twice daily equating to ~6mg total Cisplatin [~0.6mg/injection based on a 200g rat]) compared with the total amount of Cisplatin eluted from the SCPC75-Cis hybrid (0.62mg ± 0.03mg). However, while systemic Cisplatin produced severe systemic toxicity, it failed to alter significantly the tumor progression. This outcome is of relevance in the treatment of HCC due to the role of the liver in xenobiotic metabolism. Therefore, in order to increase intratumoral drug levels to an effective dose, either hepatic or systemic toxicity precludes the use of such doses. In an attempt to overcome this transarterial chemoembolization (TACE) has been developed in which chemotherapeutics are delivered directly into the tumor mass *via* the hepatic artery. To increase tumor retention TACE (usually) employs an oil-based excipient (e.g. Lipidiol), and relies on the normal pathology of HCC in which the majority of the tumor vasculature derives from the hepatic artery. Thus, while a TACE or direct intratumoral injection approach might provide a more accurate comparison for the SCPC75-Cis hybrid, this approach is not viable in the rat model of HCC employed.

Localized intratumoral Cisplatin delivery was confirmed by analysis of tumor-platinum content. Of interest, placement of the SCPC75-Cis hybrids adjacent to or within the tumor led to equivalent total Cisplatin release and inhibition of tumor growth, yet tumor-platinum content was significantly higher in the intratumoral placement model than in the adjacent placement model. One possible explanation for this may relate to differences in the environments in which the SCPC75-Cis discs are placed. Therefore, the model of HCC used leads to the formation of an encapsulated tumor. Placing the SCPC75-Cis disc within this capsule may lead to more drug retention within the necrotic

tissue than placing the disc adjacent to the tumor. Alternatively, the placement of the disc adjacent to the tumor mass may be more effective at decreasing tumor progression at the early stages of tumor growth when the tumor is relatively small, and drug concentrations are high. In this setting, we would anticipate that as the tumor progresses it is more difficult for the drug to enter the tumor from the SCPC75-Cis disc when placed adjacent and prolonged inhibition of tumor growth would be observed in only intratumorally placed discs. Conversely, in the adjacent placement model, as the tumor grows an increasing pressure exists between the tumor, the SCPC75-Cis disc, and the underlying tissue. In this instance, it is possible that more amount of the drug may be released into the underlying muscle tissue resulting in lower tumor drug concentration.

Detailed analysis of tumor pathology revealed significant levels of cellular necrosis and apoptosis in tumors treated with SCPC75-Cis hybrids. This was somewhat unexpected, as we predicted the majority of cell death would be *via* apoptosis due to Cisplatin irreversibly cross-linking DNA within the tumor cells [424]. An explanation for the degree of necrosis that we observed may relate directly to events following apoptosis *in vivo*. Under normal circumstances, a key component of the apoptotic process is the ordered removal of cell components by immune cells to prevent damage to neighboring cells [400]. However, in our model we have created a localized region of high Cisplatin content. As such, immune cells entering this environment, to remove cell debris, are equally exposed to cytotoxic levels of Cisplatin. Thus, the result of not being able to remove cell debris may be the increased necrosis we measure using the SCPC75-Cis hybrids. Similarly, this may be of further significance at a translational level in that HCC

most commonly presents in a cirrhotic liver [399]. As such elevated necrosis may directly impact already compromised hepatic function.

In addition to the ability to slow tumor progression using the SCPC75-Cis hybrids, the other striking observation we made was the lack of systemic toxicity associated with Cisplatin delivery using the SCPC75-Cis hybrids. These data, coupled with Cisplatin distribution clearly demonstrate Cisplatin is not only released within the tumor site, but remains localized within the tumor to the extent that systemic distribution or effects were not measurable. Other studies using scaffold systems for Cisplatin have been performed. For example, Tahara *et al.*, employed 10%, and 5% (*w/w*) Cisplatin-calcium phosphate cement implants to treat bone cancer. Using this approach, lower Pt concentrations were reported in kidney and liver tissue from animals treated using Cisplatin-scaffolds than that reported from the systemic Cisplatin treatment (3mg Cisplatin/kg animal) after 4 weeks [409]. Similarly, hyaluronan–Cisplatin conjugates have been employed in models of breast cancer to slow tumor progression with reduced systemic toxicity compared to systemic administration [425, 426].

5.5. Conclusion

The results presented in this study demonstrate the use of an engineered porous resorbable SCPC75 scaffold as a platform for the sustained delivery of Cisplatin. We have shown that the surface chemistry of SCPC75 dictates the binding and release of Cis. Furthermore, drug adsorption modified the bond energy of the functional groups of the ceramic and enhanced a selective ionic dissolution. Moreover, our data confirm that systemic Cisplatin administration is not an effective therapeutic approach for the treatment of HCC and is associated with severe systemic side effects. However, focal

Cisplatin delivery to the tumor mass using a SCPC75 nano scaffold drug delivery system overcome the systemic toxicity associated with daily injection, and significantly increased intratumoral drug delivery to inhibit tumor growth. These data provide encouraging evidence that SCPC75 scaffolds provide a means to re-evaluate the use of chemotherapeutic agents that are not currently used to treat HCC due to hepatic, renal, or systemic toxicity.

CHAPTER 6: SUMMARY AND RECOMMENDATIONS FOR FUTURE WORK

6.1. Summary of Findings

The microstructure of SCPC can be manipulated to tailor custom made drug delivery systems. It was demonstrated that not only the porosity but also the active surface of SCPC can significantly modify the performance of the bioceramic as carrier for DDS. Physical and chemical properties of SCPC bioceramic can significantly be altered by its chemical composition. Physical structural characteristics of Cris demonstrated to provide high density of nano pores and superior surface area enhancing material drug loading capacity. Low chemical interaction between different drug molecules and Cris was also observed which can lead to a rapid release kinetic rate. Furthermore, the sustained release observed from Cris sample showed to be controlled mainly by the tortuosity of constricted porous matrix due to the stability of the ceramic. On the other hand, Rhe demonstrated to be chemically bioactive, and to form stable bonds with drug molecules, contributing to prolonged release of therapeutics. In vitro bioactivity tests showed SCPC50 and Rhe ability to form carbonate HAp layer on the surface of the ceramics particles after immersion in SBF for 24 h at 37^{o}C. SCPC has the advantage to have both physical and chemical mechanisms for loading and release molecules. Plus solid solution of crystalline phases of SCPC enhances the bioactivity of the composite even for the α-cristobalite phase. These found were used to design a

controlled delivery system that provided a promising treatment against HCC without acute side effects.

Composition of SCPC also affected the material dissolution kinetics under physiological conditions. The high elution rate of negatively charged ions from SCPC50, most probably due to the dissolution of Si-rich amorphous phase demonstrated to significantly increase the alkalinity of the immersing physiological solutions. Increases in the alkalinity of solutions incubated with SCPC could be a limiting for its use as DDS, yet it could cause undesirable effects on the bioactivity of some medicaments or induce to cytotoxicity. This can be avoided by immersing SCPC in SBF per 24 hours. NMR analysis and in vitro biological assays confirmed that the concentration of dissolution products from SCPC is not high enough to cause significant changes in the bioactivity of the released drugs. Moreover, control SCPC without drug in both in vivo and in vitro toxicity assays demonstrated minimum cytotoxicity or inflammatory response caused by the dissolution products of the SCPC.

Analysis of the ceramic surface to detect carrier-drug interactions showed to be valuable to understand the performance of the drug delivery systems. It was demonstrated that, for the same carrier, the ability of drug binding and release also depends on the kind of drug. These observations suggest that a custom made delivery system is necessary for each drug. With respect to Cris binding was mainly by physisorption, depending on the surface area and porosity as confirmed by FTIR analysis. On the other hand, for Rhe P-O functional groups demonstrated to be the active site for drug binding. Although, Cris has three times higher surface area than Rhe, yet comparable amounts of Vanc were bond to the two materials. These results emphasize the significant role of surface chemistry and

functional groups in drug binding to bioactive materials. The nature of bonding at the interface between drug and ceramic contributed to significant variations in release kinetics.

Finally, Si-rich SCPC-Cis hybrid scaffolds demonstrated to reduce the rate of tumor progression in an animal model of HCC significantly, in the absence of adverse systemic effects. Analysis showed similarities in the release kinetics in vitro and in vivo with similar amounts of drug release (55%) within 5d. Overall, treatment with SCPC-Cis hybrids reduced tumor volume by ~65-70% compared to animals treated with systemic Cisplatin without showing signs of systemic toxicity.

6.1. Recommendations for Future Work

Microstructure of SCPC demonstrated to affect the ability of the bioceramic for drug loading and release significantly. Results presented in this study strongly demonstrate how SCPC can be easily manipulated for customized drug delivery system.

Alternatively, SCPC-Cis scaffolds showed promising and encouraging results to treat HCC with minimum side effects. Therefore, results are encouraging to do more in vivo studies that corroborate the efficacy of SCPC-Cis to treat different cancers. Insertion of ceramic discs in an environment closer to the real disease conditions is required. To do this more complex animal model might be needed, e.g., using bigger animals to treat HCC directly in the liver. Furthermore, the need of a surgery procedure to introduce the scaffold can be a drawback for SCPC-Cis discs DDS. Therefore, evaluation of injectable SCPC-Cis DDS is suggested. Organic hydrogels like Alginic acid or Gelatin, which have demonstrated high degradation rates, and excellent biocompatibility with live tissue. Therefore, they are proposed as vehicles to facilitate the

injection of the ceramic-drug particles. Moreover, injectable SCPC delivery system can be tested for other drugs due to the versatility of SCPC to load different kind of drugs including other cancer drugs, antibiotics, antiviral and the possibility to tailor custom made SCPC-drug release kinetics hybrids by controlling the crystalline structure of the material.

REFERENCES

[1] Langer R. Drug delivery and targeting. Nature 1998;392:5-10.

[2] Ratner BD, Hoffman AS, Schoen FJ, Lemons J. Biomaterials science: a multidisciplinary endeavor. Biomaterials Science: An Introduction to Materials in Medicine 2004:1-9.

[3] Hoffman AS. The origins and evolution of "controlled" drug delivery systems. Journal of Controlled Release 2008;132:153-63.

[4] Arruebo M, Fernández-Pacheco R, Ibarra MR, Santamaría J. Magnetic nanoparticles for drug delivery. Nano Today 2007;2:22-32.

[5] Athanasiou KA, Niederauer GG, Agrawal CM. Sterilization, toxicity, biocompatibility and clinical applications of polylactic acid/ polyglycolic acid copolymers. Biomaterials 1996;17:93-102.

[6] Barbé C, Bartlett J, Kong L, Finnie K, Lin HQ, Larkin M, et al. Silica Particles: A Novel Drug-Delivery System. Advanced Materials 2004;16:1959-66.

[7] Park H, Park K. Biocompatibility Issues of Implantable Drug Delivery Systems. Pharm Res 1996;13:1770-6.

[8] Trajkovski B, Petersen A, Strube P, Mehta M, Duda GN. Intra-operatively customized implant coating strategies for local and controlled drug delivery to bone. Advanced drug delivery reviews 2012;64:1142-51.

[9] Desale SS, Cohen SM, Zhao Y, Kabanov AV, Bronich TK. Biodegradable hybrid polymer micelles for combination drug therapy in ovarian cancer. Journal of Controlled Release.

[10] Kluge J, Mazzotti M. CO2-assisted high pressure homogenization: A solvent-free process for polymeric microspheres and drug–polymer composites. International Journal of Pharmaceutics 2012;436:394-402.

[11] Patel B, Gupta V, Ahsan F. PEG–PLGA based large porous particles for pulmonary delivery of a highly soluble drug, low molecular weight heparin. Journal of Controlled Release 2012;162:310-20.

[12] Rajan M, Raj V, Al-Arfaj AA, Murugan AM. Hyaluronidase enzyme core-5-fluorouracil-loaded chitosan-PEG-gelatin polymer nanocomposites as targeted and controlled drug delivery vehicles. International Journal of Pharmaceutics 2013;453:514-22.

[13] Rattanakit P, Moulton SE, Santiago KS, Liawruangrath S, Wallace GG. Extrusion printed polymer structures: A facile and versatile approach to tailored drug delivery platforms. International Journal of Pharmaceutics 2012;422:254-63.

[14] Arcos D, Vila M, López-Noriega A, Rossignol F, Champion E, Oliveira FJ, et al. Mesoporous bioactive glasses: Mechanical reinforcement by means of a biomimetic process. Acta Biomaterialia 2011;7:2952-9.

[15] Costache MC, Vaughan AD, Qu H, Ducheyne P, Devore DI. Tyrosine-derived polycarbonate-silica xerogel nanocomposites for controlled drug delivery. Acta Biomaterialia 2013;9:6544-52.

[16] Lin S, Van den Bergh W, Baker S, Jones JR. Protein interactions with nanoporous sol–gel derived bioactive glasses. Acta Biomaterialia 2011;7:3606-15.

[17] Rahaman MN, Day DE, Sonny Bal B, Fu Q, Jung SB, Bonewald LF, et al. Bioactive glass in tissue engineering. Acta Biomaterialia 2011;7:2355-73.

[18] Zhang X, Jia W, Gu Y, Xiao W, Liu X, Wang D, et al. Teicoplanin-loaded borate bioactive glass implants for treating chronic bone infection in a rabbit tibia osteomyelitis model. Biomaterials 2010;31:5865-74.

[19] Bray JM, Filiaggi MJ, Bowen CV, Beyea SD. Degradation and drug release in calcium polyphosphate bioceramics: An MRI-based characterization. Acta Biomaterialia 2012;8:3821-31.

[20] Ewald A, Hösel D, Patel S, Grover LM, Barralet JE, Gbureck U. Silver-doped calcium phosphate cements with antimicrobial activity. Acta Biomaterialia 2011;7:4064-70.

[21] Giger EV, Puigmartí-Luis J, Schlatter R, Castagner B, Dittrich PS, Leroux J-C. Gene delivery with bisphosphonate-stabilized calcium phosphate nanoparticles. Journal of Controlled Release 2011;150:87-93.

[22] El-Ghannam A, Ducheyne P. 1.109 - Bioactive Ceramics. In: Editor-in-Chief: Paul D, editor. Comprehensive Biomaterials. Oxford: Elsevier; 2011. p. 157-79.

[23] Arcos D, Vallet-Regí M. Bioceramics for drug delivery. Acta Materialia 2013;61:890-911.

[24] Son JS, Appleford M, Ong JL, Wenke JC, Kim JM, Choi SH, et al. Porous hydroxyapatite scaffold with three-dimensional localized drug delivery system using biodegradable microspheres. Journal of Controlled Release 2011;153:133-40.

[25] Zheng F, Wang S, Wen S, Shen M, Zhu M, Shi X. Characterization and antibacterial activity of amoxicillin-loaded electrospun nano-hydroxyapatite/poly(lactic-co-glycolic acid) composite nanofibers. Biomaterials 2013;34:1402-12.

[26] D'Este M, Eglin D. Hydrogels in calcium phosphate moldable and injectable bone substitutes: Sticky excipients or advanced 3-D carriers? Acta Biomaterialia 2013;9:5421-30.

[27] Hulsart-Billström G, Hu Q, Bergman K, Jonsson KB, Åberg J, Tang R, et al. Calcium phosphates compounds in conjunction with hydrogel as carrier for BMP-2: A study on ectopic bone formation in rats. Acta Biomaterialia 2011;7:3042-9.

[28] Jayalekshmi AC, Victor SP, Sharma CP. Magnetic and degradable polymer/bioactive glass composite nanoparticles for biomedical applications. Colloids and Surfaces B: Biointerfaces 2013;101:196-204.

[29] Xia W, Chang J, Lin J, Zhu J. The pH-controlled dual-drug release from mesoporous bioactive glass/polypeptide graft copolymer nanomicelle composites. European Journal of Pharmaceutics and Biopharmaceutics 2008;69:546-52.

[30] Costache MC, Qu H, Ducheyne P, Devore DI. Polymer–xerogel composites for controlled release wound dressings. Biomaterials 2010;31:6336-43.

[31] Xu Q, Chin SE, Wang C-H, Pack DW. Mechanism of drug release from double-walled PDLLA(PLGA) microspheres. Biomaterials 2013;34:3902-11.

[32] Alkhraisat MH, Rueda C, Cabrejos-Azama J, Lucas-Aparicio J, Mariño FT, Torres García-Denche J, et al. Loading and release of doxycycline hyclate from strontium-substituted calcium phosphate cement. Acta Biomaterialia 2010;6:1522-8.

[33] Butscher A, Bohner M, Hofmann S, Gauckler L, Müller R. Structural and material approaches to bone tissue engineering in powder-based three-dimensional printing. Acta Biomaterialia 2011;7:907-20.

[34] Erol MM, Mouriño V, Newby P, Chatzistavrou X, Roether JA, Hupa L, et al. Copper-releasing, boron-containing bioactive glass-based scaffolds coated with alginate for bone tissue engineering. Acta Biomaterialia 2012;8:792-801.

[35] Chertok B, David AE, Yang VC. Brain tumor targeting of magnetic nanoparticles for potential drug delivery: Effect of administration route and magnetic field topography. Journal of Controlled Release 2011;155:393-9.

[36] Deok Kong S, Sartor M, Jack Hu C-M, Zhang W, Zhang L, Jin S. Magnetic field activated lipid–polymer hybrid nanoparticles for stimuli-responsive drug release. Acta Biomaterialia 2013;9:5447-52.

[37] Oliveira H, Pérez-Andrés E, Thevenot J, Sandre O, Berra E, Lecommandoux S. Magnetic field triggered drug release from polymersomes for cancer therapeutics. Journal of Controlled Release 2013;169:165-70.

[38] Tung WL, Hu SH, Liu DM. Synthesis of nanocarriers with remote magnetic drug release control and enhanced drug delivery for intracellular targeting of cancer cells. Acta Biomaterialia 2011;7:2873-82.

[39] Yang J, Liu W, Sui M, Tang J, Shen Y. Platinum (IV)-coordinate polymers as intracellular reduction-responsive backbone-type conjugates for cancer drug delivery. Biomaterials 2011;32:9136-43.

[40] Koo AN, Min KH, Lee HJ, Lee S-U, Kim K, Chan Kwon I, et al. Tumor accumulation and antitumor efficacy of docetaxel-loaded core-shell-corona micelles with shell-specific redox-responsive cross-links. Biomaterials 2012;33:1489-99.

[41] Pan Y-J, Chen Y-Y, Wang D-R, Wei C, Guo J, Lu D-R, et al. Redox/pH dual stimuli-responsive biodegradable nanohydrogels with varying responses to dithiothreitol and glutathione for controlled drug release. Biomaterials 2012;33:6570-9.

[42] Zhao M, Biswas A, Hu B, Joo K-I, Wang P, Gu Z, et al. Redox-responsive nanocapsules for intracellular protein delivery. Biomaterials 2011;32:5223-30.

[43] Ho VHB, Slater NKH, Chen R. pH-responsive endosomolytic pseudo-peptides for drug delivery to multicellular spheroids tumour models. Biomaterials 2011;32:2953-8.

[44] Suedee R, Jantarat C, Lindner W, Viernstein H, Songkro S, Srichana T. Development of a pH-responsive drug delivery system for enantioselective-controlled delivery of racemic drugs. Journal of Controlled Release 2010;142:122-31.

[45] Zhang CY, Yang YQ, Huang TX, Zhao B, Guo XD, Wang JF, et al. Self-assembled pH-responsive MPEG-b-(PLA-co-PAE) block copolymer micelles for anticancer drug delivery. Biomaterials 2012;33:6273-83.

[46] de Smet M, Langereis S, van den Bosch S, Bitter K, Hijnen NM, Heijman E, et al. SPECT/CT imaging of temperature-sensitive liposomes for MR-image guided drug delivery with high intensity focused ultrasound. Journal of Controlled Release;169:82-90.

[47] Joshi RV, Nelson CE, Poole KM, Skala MC, Duvall CL. Dual pH- and temperature-responsive microparticles for protein delivery to ischemic tissues. Acta Biomaterialia 2013;9:6526-34.

[48] Dong L, Xia S, Wu K, Huang Z, Chen H, Chen J, et al. A pH/Enzyme-responsive tumor-specific delivery system for doxorubicin. Biomaterials 2010;31:6309-16.

[49] Wanakule P, Liu GW, Fleury AT, Roy K. Nano-inside-micro: Disease-responsive microgels with encapsulated nanoparticles for intracellular drug delivery to the deep lung. Journal of Controlled Release 2012;162:429-37.

[50] Su S, Wang H, Liu X, Wu Y, Nie G. iRGD-coupled responsive fluorescent nanogel for targeted drug delivery. Biomaterials 2013;34:3523-33.

[51] Murdan S. Electro-responsive drug delivery from hydrogels. Journal of Controlled Release 2003;92:1-17.

[52] Zhang R, Tang M, Bowyer A, Eisenthal R, Hubble J. A novel pH- and ionic-strength-sensitive carboxy methyl dextran hydrogel. Biomaterials 2005;26:4677-83.

[53] Haley B, Frenkel E. Nanoparticles for drug delivery in cancer treatment. Urologic Oncology: Seminars and original investigations: Elsevier; 2008. p. 57-64.

[54] Ganta S, Devalapally H, Shahiwala A, Amiji M. A review of stimuli-responsive nanocarriers for drug and gene delivery. Journal of Controlled Release 2008;126:187-204.

[55] Danhier F, Feron O, Préat V. To exploit the tumor microenvironment: Passive and active tumor targeting of nanocarriers for anti-cancer drug delivery. Journal of Controlled Release 2010;148:135-46.

[56] Zhang Y, Chan HF, Leong KW. Advanced materials and processing for drug delivery: The past and the future. Advanced drug delivery reviews 2012.

[57] Allen TM, Cullis PR. Drug delivery systems: entering the mainstream. Science 2004;303:1818-22.

[58] Dewan SS. Advance drug delivery systems: Technologies and global markets. 2011.

[59] Verma RK, Garg S. Drug delivery technologies and future directions. Pharmaceut Technol On-Line 2001;25:1-14.

[60] Gaucher G, Dufresne M-H, Sant VP, Kang N, Maysinger D, Leroux J-C. Block copolymer micelles: preparation, characterization and application in drug delivery. Journal of Controlled Release 2005;109:169-88.

[61] Li C, Wallace S. Polymer-drug conjugates: Recent development in clinical oncology. Advanced drug delivery reviews 2008;60:886-98.

[62] Gao X, Tao W, Lu W, Zhang Q, Zhang Y, Jiang X, et al. Lectin-conjugated PEG–PLA nanoparticles: Preparation and brain delivery after intranasal administration. Biomaterials 2006;27:3482-90.

[63] Greenwald RB. PEG drugs: an overview. Journal of Controlled Release 2001;74:159-71.

[64] Pasut G, Veronese FM. PEG conjugates in clinical development or use as anticancer agents: An overview. Advanced drug delivery reviews 2009;61:1177-88.

[65] Yoo HS, Park TG. Biodegradable polymeric micelles composed of doxorubicin conjugated PLGA–PEG block copolymer. Journal of Controlled Release 2001;70:63-70.

[66] Shiah J-G, Dvořák M, Kopečková P, Sun Y, Peterson C, Kopeček J. Biodistribution and antitumour efficacy of long-circulating N-(2-hydroxypropyl) methacrylamide

copolymer–doxorubicin conjugates in nude mice. European Journal of Cancer 2001;37:131-9.

[67] Duncan R, Kopeckova-Rejmanova P, Strohalm J, Hume I, Cable H, Pohl J, et al. Anticancer agents coupled to N-(2-hydroxypropyl) methacrylamide copolymers. I. Evaluation of daunomycin and puromycin conjugates in vitro. British journal of cancer 1987;55:165.

[68] Vasey PA, Kaye SB, Morrison R, Twelves C, Wilson P, Duncan R, et al. Phase I clinical and pharmacokinetic study of PK1 [N-(2-hydroxypropyl) methacrylamide copolymer doxorubicin]: first member of a new class of chemotherapeutic agents—drug-polymer conjugates. Clinical Cancer Research 1999;5:83-94.

[69] Agarwal A, Gupta U, Asthana A, Jain NK. Dextran conjugated dendritic nanoconstructs as potential vectors for anti-cancer agent. Biomaterials 2009;30:3588-96.

[70] Larsen C. Dextran prodrugs — structure and stability in relation to therapeutic activity. Advanced drug delivery reviews 1989;3:103-54.

[71] Takakura Y, Kitajima M, Matsumoto S, Hashida M, Sezaki H. Development of a novel polymeric prodrug of mitomycin C, mitomycin C-dextran conjugate with anionic charge. I. Physicochemical characteristics and in vivo and in vitro antitumor activities. International Journal of Pharmaceutics 1987;37:135-43.

[72] Kadlecova Z, Rajendra Y, Matasci M, Baldi L, Hacker DL, Wurm FM, et al. DNA delivery with hyperbranched polylysine: A comparative study with linear and dendritic polylysine. Journal of Controlled Release 2013;169:276-88.

[73] Kaminskas LM, Kelly BD, McLeod VM, Sberna G, Owen DJ, Boyd BJ, et al. Characterisation and tumour targeting of PEGylated polylysine dendrimers bearing doxorubicin via a pH labile linker. Journal of Controlled Release 2011;152:241-8.

[74] Parelkar SS, Chan-Seng D, Emrick T. Reconfiguring polylysine architectures for controlling polyplex binding and non-viral transfection. Biomaterials 2011;32:2432-44.

[75] Yoncheva K, Lizarraga E, Irache JM. Pegylated nanoparticles based on poly (methyl vinyl ether-co-maleic anhydride): preparation and evaluation of their bioadhesive properties. European journal of pharmaceutical sciences 2005;24:411-9.

[76] Yokoyama M, Miyauchi M, Yamada N, Okano T, Sakurai Y, Kataoka K, et al. Characterization and anticancer activity of the micelle-forming polymeric anticancer drug adriamycin-conjugated poly (ethylene glycol)-poly (aspartic acid) block copolymer. Cancer research 1990;50:1693-700.

[77] Luo Q, Wang P, Miao Y, He H, Tang X. A novel 5-fluorouracil prodrug using hydroxyethyl starch as a macromolecular carrier for sustained release. Carbohydrate Polymers 2012;87:2642-7.

[78] Cai X, Yang L, Zhang L-M, Wu Q. Synthesis and anaerobic biodegradation of indomethacin-conjugated cellulose ethers used for colon-specific drug delivery. Bioresource Technology 2009;100:4164-70.

[79] Patri AK, Kukowska-Latallo JF, Baker Jr JR. Targeted drug delivery with dendrimers: Comparison of the release kinetics of covalently conjugated drug and non-covalent drug inclusion complex. Advanced drug delivery reviews 2005;57:2203-14.

[80] Harris JM, Chess RB. Effect of pegylation on pharmaceuticals. Nature Reviews Drug Discovery 2003;2:214-21.

[81] Levy Y, Hershfield MS, Fernandez-Mejia C, Polmar SH, Scudiery D, Berger M, et al. Adenosine deaminase deficiency with late onset of recurrent infections: response to treatment with polyethylene glycol-modified adenosine deaminase. The Journal of pediatrics 1988;113:312-7.

[82] Graham ML. Pegaspargase: a review of clinical studies. Advanced drug delivery reviews 2003;55:1293-302.

[83] Bukowski R, Ernstoff MS, Gore ME, Nemunaitis JJ, Amato R, Gupta SK, et al. Pegylated interferon alfa-2b treatment for patients with solid tumors: a phase I/II study. Journal of clinical oncology 2002;20:3841-949.

[84] Shaker OG, Sadik NAH, El-Dessouki A. Single-nucleotide polymorphism in the promoter region of the osteopontin gene at nucleotide −443 as a marker predicting the efficacy of pegylated interferon/ribavirin-therapy in Egyptians patients with chronic hepatitis C. Human Immunology 2012;73:1039-45.

[85] Gozlan J, Lacombe K, Gault E, Raguin G, Girard P-M. Complete cure of HBV-HDV co-infection after 24 weeks of combination therapy with pegylated interferon and ribavirin in a patient co-infected with HBV/HCV/HDV/HIV. Journal of Hepatology 2009;50:432-4.

[86] Voigt E, Schulz C, Klausen G, Goelz J, Mauss S, Schmutz G, et al. Pegylated interferon α-2b plus ribavirin for the treatment of chronic hepatitis C in HIV-coinfected patients. Journal of Infection 2006;53:36-42.

[87] Jeon S, Lee J, Andrade J, De Gennes P. Protein—surface interactions in the presence of polyethylene oxide: I. Simplified theory. Journal of Colloid and Interface Science 1991;142:149-58.

[88] Juliano R. Factors affecting the clearance kinetics and tissue distribution of liposomes, microspheres and emulsions. Advanced drug delivery reviews 1988;2:31-54.

[89] Torchilin VP, Omelyanenko VG, Papisov MI, Bogdanov AA, Trubetskoy VS, Herron JN, et al. Poly (ethylene glycol) on the liposome surface: on the mechanism of polymer-coated liposome longevity. Biochimica et Biophysica Acta (BBA)-Biomembranes 1994;1195:11-20.

[90] Duncan R. Development of HPMA copolymer–anticancer conjugates: Clinical experience and lessons learnt. Advanced drug delivery reviews 2009;61:1131-48.

[91] Etrych T, Jelínková M, Říhová B, Ulbrich K. New HPMA copolymers containing doxorubicin bound via pH-sensitive linkage: synthesis and preliminary in vitro and in vivo biological properties. Journal of Controlled Release 2001;73:89-102.

[92] Nishiyama N, Okazaki S, Cabral H, Miyamoto M, Kato Y, Sugiyama Y, et al. Novel cisplatin-incorporated polymeric micelles can eradicate solid tumors in mice. Cancer research 2003;63:8977-83.

[93] Owen SC, Patel N, Logie J, Pan G, Persson H, Moffat J, et al. Targeting HER2 + breast cancer cells: Lysosomal accumulation of anti-HER2 antibodies is influenced by antibody binding site and conjugation to polymeric nanoparticles. Journal of Controlled Release.

[94] Wagner S, Rothweiler F, Anhorn MG, Sauer D, Riemann I, Weiss EC, et al. Enhanced drug targeting by attachment of an anti αv integrin antibody to doxorubicin loaded human serum albumin nanoparticles. Biomaterials 2010;31:2388-98.

[95] Farokhzad OC, Jon S, Khademhosseini A, Tran T-NT, LaVan DA, Langer R. Nanoparticle-aptamer bioconjugates a new approach for targeting prostate cancer cells. Cancer research 2004;64:7668-72.

[96] Pestourie C, Tavitian B, Duconge F. Aptamers against extracellular targets for in vivo applications. Biochimie 2005;87:921-30.

[97] Bagalkot V, Farokhzad OC, Langer R, Jon S. An Aptamer–Doxorubicin Physical Conjugate as a Novel Targeted Drug-Delivery Platform. Angewandte Chemie International Edition 2006;45:8149-52.

[98] Huang YF, Shangguan D, Liu H, Phillips JA, Zhang X, Chen Y, et al. Molecular assembly of an aptamer–drug conjugate for targeted drug delivery to tumor cells. ChemBioChem 2009;10:862-8.

[99] Li H, LaBean TH, Leong KW. Nucleic acid-based nanoengineering: novel structures for biomedical applications. Interface Focus 2011;1:702-24.

[100] Douglas SM, Dietz H, Liedl T, Högberg B, Graf F, Shih WM. Self-assembly of DNA into nanoscale three-dimensional shapes. Nature 2009;459:414-8.

[101] Choi K-m, Kwon IC, Ahn HJ. Self-assembled amphiphilic DNA-cholesterol/DNA-peptide hybrid duplexes with liposome-like structure for doxorubicin delivery. Biomaterials 2013;34:4183-90.

[102] Li J, Pei H, Zhu B, Liang L, Wei M, He Y, et al. Self-assembled multivalent DNA nanostructures for noninvasive intracellular delivery of immunostimulatory CpG oligonucleotides. ACS nano 2011;5:8783-9.

[103] Roh YH, Lee JB, Kiatwuthinon P, Hartman MR, Cha JJ, Um SH, et al. DNAsomes: Multifunctional DNA-Based Nanocarriers. small 2011;7:74-8.

[104] Decuzzi P, Pasqualini R, Arap W, Ferrari M. Intravascular delivery of particulate systems: does geometry really matter? Pharm Res 2009;26:235-43.

[105] Muro S, Garnacho C, Champion JA, Leferovich J, Gajewski C, Schuchman EH, et al. Control of endothelial targeting and intracellular delivery of therapeutic enzymes by modulating the size and shape of ICAM-1-targeted carriers. Molecular Therapy 2008;16:1450-8.

[106] Rösler A, Vandermeulen GWM, Klok H-A. Advanced drug delivery devices via self-assembly of amphiphilic block copolymers. Advanced drug delivery reviews 2001;53:95-108.

[107] Iijima M, Nagasaki Y, Okada T, Kato M, Kataoka K. Core-polymerized reactive micelles from heterotelechelic amphiphilic block copolymers. Macromolecules 1999;32:1140-6.

[108] Ding J, Liu G. Water-soluble hollow nanospheres as potential drug carriers. The Journal of Physical Chemistry B 1998;102:6107-13.

[109] Huo M, Zou A, Yao C, Zhang Y, Zhou J, Wang J, et al. Somatostatin receptor-mediated tumor-targeting drug delivery using octreotide-PEG-deoxycholic acid conjugate-modified N-deoxycholic acid-O, N-hydroxyethylation chitosan micelles. Biomaterials 2012;33:6393-407.

[110] Talelli M, Rijcken CJF, Oliveira S, van der Meel R, van Bergen en Henegouwen PMP, Lammers T, et al. Nanobody — Shell functionalized thermosensitive core-crosslinked polymeric micelles for active drug targeting. Journal of Controlled Release 2011;151:183-92.

[111] Ledley FD. Pharmaceutical approach to somatic gene therapy. Pharm Res 1996;13:1595-614.

[112] Jeong JH, Kim SW, Park TG. Molecular design of functional polymers for gene therapy. Progress in Polymer Science 2007;32:1239-74.

[113] Wu AM, Senter PD. Arming antibodies: prospects and challenges for immunoconjugates. Nature biotechnology 2005;23:1137-46.

[114] Dlugi A, Miller J, Knittle J. Lupron depot (leuprolide acetate for depot suspension) in the treatment of endometriosis: a randomized, placebo-controlled, double-blind study. Lupron Study Group. Fertility and sterility 1990;54:419.

[115] O'brien M, Wigler N, Inbar M, Rosso R, Grischke E, Santoro A, et al. Reduced cardiotoxicity and comparable efficacy in a phase III trial of pegylated liposomal

doxorubicin HCl (CAELYX™/Doxil®) versus conventional doxorubicin for first-line treatment of metastatic breast cancer. Annals of oncology 2004;15:440-9.

[116] Soundararajan A, Bao A, Phillips WT, Perez Iii R, Goins BA. [186Re]Liposomal doxorubicin (Doxil): in vitro stability, pharmacokinetics, imaging and biodistribution in a head and neck squamous cell carcinoma xenograft model. Nuclear Medicine and Biology 2009;36:515-24.

[117] Green M, Manikhas G, Orlov S, Afanasyev B, Makhson A, Bhar P, et al. Abraxane®, a novel Cremophor®-free, albumin-bound particle form of paclitaxel for the treatment of advanced non-small-cell lung cancer. Annals of oncology 2006;17:1263-8.

[118] Couvreur P. Nanoparticles in drug delivery: Past, present and future. Advanced drug delivery reviews 2013;65:21-3.

[119] Hong R-L, Huang C-J, Tseng Y-L, Pang VF, Chen S-T, Liu J-J, et al. Direct Comparison of Liposomal Doxorubicin with or without Polyethylene Glycol Coating in C-26 Tumor-bearing Mice Is Surface Coating with Polyethylene Glycol Beneficial? Clinical Cancer Research 1999;5:3645-52.

[120] Song LY, Ahkong QF, Rong Q, Wang Z, Ansell S, Hope MJ, et al. Characterization of the inhibitory effect of PEG-lipid conjugates on the intracellular delivery of plasmid and antisense DNA mediated by cationic lipid liposomes. Biochimica et Biophysica Acta (BBA) - Biomembranes 2002;1558:1-13.

[121] Li S-D, Huang L. Stealth nanoparticles: high density but sheddable PEG is a key for tumor targeting. Journal of controlled release: official journal of the Controlled Release Society 2010;145:178.

[122] Saltzman WM. Drug delivery: engineering principles for drug therapy: Oxford University Press; 2001.

[123] Okada H, Toguchi H. Biodegradable microspheres in drug delivery. Critical Reviews™ in Therapeutic Drug Carrier Systems 1995;12.

[124] Anderson JM, Shive MS. Biodegradation and biocompatibility of PLA and PLGA microspheres. Advanced drug delivery reviews 1997;28:5-24.

[125] Sinha VR, Trehan A. Biodegradable microspheres for protein delivery. Journal of Controlled Release 2003;90:261-80.

[126] Sachlos E, Czernuszka J. Making tissue engineering scaffolds work. Review: the application of solid freeform fabrication technology to the production of tissue engineering scaffolds. Eur Cell Mater 2003;5:39-40.

[127] Hutmacher DW. Scaffold design and fabrication technologies for engineering tissues—state of the art and future perspectives. Journal of Biomaterials Science, Polymer Edition 2001;12:107-24.

[128] Sun L-G, Xie Z-Y, Zhao Y-J, Wei H-M, Gu Z-Z. Optical monitoring the degradation of PLGA inverse opal film. Chinese Chemical Letters 2013;24:9-12.

[129] Lu L, Peter SJ, D Lyman M, Lai H-L, Leite SM, Tamada JA, et al. In vitro and in vivo degradation of porous poly (dl-lactic-< i> co</i>-glycolic acid) foams. Biomaterials 2000;21:1837-45.

[130] Jackanicz TM, Nash HA, Wise DL, Gregory JB. Polylactic acid as a biodegradable carrier for contraceptive steroids. Contraception 1973;8:227-34.

[131] Beck L, Cowsar D, Lewis D, Cosgrove Jr R, Riddle CT, Lowry S, et al. A new long-acting injectable microcapsule system for the administration of progesterone. Fertility and sterility 1979;31:545.

[132] Webber WL, Lago F, Thanos C, Mathiowitz E. Characterization of soluble, salt-loaded, degradable PLGA films and their release of tetracycline. Journal of biomedical materials research 1998;41:18-29.

[133] Ramchandani M, Robinson D. In vitro and in vivo release of ciprofloxacin from PLGA 50: 50 implants. Journal of Controlled Release 1998;54:167-75.

[134] Qian F, Stowe N, Saidel GM, Gao J. Comparison of doxorubicin concentration profiles in radiofrequency-ablated rat livers from sustained-and dual-release PLGA millirods. Pharm Res 2004;21:394-9.

[135] Singh M, Shirley B, Bajwa K, Samara E, Hora M, O'Hagan D. Controlled release of recombinant insulin-like growth factor from a novel formulation of polylactide-co-glycolide microparticles. Journal of Controlled Release 2001;70:21-8.

[136] Schmaljohann D. Thermo- and pH-responsive polymers in drug delivery. Advanced drug delivery reviews 2006;58:1655-70.

[137] Reza MS, Quadir MA, Haider SS. Comparative evaluation of plastic, hydrophobic and hydrophilic polymers as matrices for controlled-release drug delivery. J Pharm Pharm Sci 2003;6:282-91.

[138] Hasty B, Heuer D, Minckler D. Primate trabeculectomies with 5-fluorouracil collagen implants. American journal of ophthalmology 1990;109:721.

[139] Punch PI, Costa ND, Edwards ME, Wilcox GE. The release of insoluble antibiotics from collagen ocular inserts in vitro and their insertion into the conjunctival sac of cattle. Journal of Veterinary Pharmacology and Therapeutics 1987;10:37-42.

[140] Ekici S, Ilgin P, Butun S, Sahiner N. Hyaluronic acid hydrogel particles with tunable charges as potential drug delivery devices. Carbohydrate Polymers 2011;84:1306-13.

[141] Rouse JJ, Whateley TL, Thomas M, Eccleston GM. Controlled drug delivery to the lung: Influence of hyaluronic acid solution conformation on its adsorption to hydrophobic drug particles. International Journal of Pharmaceutics 2007;330:175-82.

[142] Hofmann S, Wong Po Foo CT, Rossetti F, Textor M, Vunjak-Novakovic G, Kaplan DL, et al. Silk fibroin as an organic polymer for controlled drug delivery. Journal of Controlled Release 2006;111:219-27.

[143] Wenk E, Merkle HP, Meinel L. Silk fibroin as a vehicle for drug delivery applications. Journal of Controlled Release 2011;150:128-41.

[144] Hoffman AS. Hydrogels for biomedical applications. Advanced drug delivery reviews 2012;64, Supplement:18-23.

[145] Peppas NA, Meadows DL. Macromolecular structure and solute diffusion in membranes: an overview of recent theories. Journal of Membrane Science 1983;16:361-77.

[146] Harland RS, Peppas NA. Solute diffusion in swollen membranes. Polymer Bulletin 1987;18:553-6.

[147] Jeyanthi R, Panduranga K. Collagen-poly (Hema) hydrogels for the controlled release of anticancer drugs—preparation and characterization. Journal of bioactive and compatible polymers 1990;5:194-211.

[148] Wang D, Robinson DR, Kwon GS, Samuel J. Encapsulation of plasmid DNA in biodegradable poly(d,l-lactic-co-glycolic acid) microspheres as a novel approach for immunogene delivery. Journal of Controlled Release 1999;57:9-18.

[149] Kunou N, Ogura Y, Hashizoe M, Honda Y, Hyon S-H, Ikada Y. Controlled intraocular delivery of ganciclovir with use of biodegradable scleral implant in rabbits. Journal of Controlled Release 1995;37:143-50.

[150] Martina M, Hutmacher DW. Biodegradable polymers applied in tissue engineering research: a review. Polymer International 2007;56:145-57.

[151] Babensee JE, Anderson JM, McIntire LV, Mikos AG. Host response to tissue engineered devices. Advanced drug delivery reviews 1998;33:111-39.

[152] Lewandrowski K-U, Gresser JD, Wise DL, Trantolo DJ, Hasirci V. Tissue responses to molecularly reinforced polylactide-co-glycolide implants. Journal of Biomaterials Science, Polymer Edition 2000;11:401-14.

[153] Malafaya PB, Silva GA, Reis RL. Natural–origin polymers as carriers and scaffolds for biomolecules and cell delivery in tissue engineering applications. Advanced drug delivery reviews 2007;59:207-33.

[154] van Luyn MJA, van Wachem PB, Olde Damink L, Dijkstra PJ, Feijen J, Nieuwenhuis P. Relations between in vitro cytotoxicity and crosslinked dermal sheep collagens. Journal of biomedical materials research 1992;26:1091-110.

[155] Olde Damink LHH, Dijkstra PJ, van Luyn MJA, van Wachem PB, Nieuwenhuis P, Feijen J. Cross-linking of dermal sheep collagen using a water-soluble carbodiimide. Biomaterials 1996;17:765-73.

[156] DiMaio FR. The science of bone cement: a historical review. Orthopedics 2002;25:1399.

[157] Majid SA, Lindberg LT, Gunterberg B, Siddiki MS. Gentamicin-PMMA beads in the treatment of chronic osteomyelitis. Acta Orthopaedica 1985;56:265-8.

[158] Wahlig H, Dingeldein E, Bergmann R, Reuss K. The release of gentamicin from polymethylmethacrylate beads. An experimental and pharmacokinetic study. Journal of Bone & Joint Surgery, British Volume 1978;60:270-5.

[159] Moojen DJF, Hentenaar B, Charles Vogely H, Verbout AJ, Castelein RM, Dhert WJA. In Vitro Release of Antibiotics from Commercial PMMA Beads and Articulating Hip Spacers. The Journal of Arthroplasty 2008;23:1152-6.

[160] Neut D, van de Belt H, van Horn JR, van der Mei HC, Busscher HJ. Residual gentamicin-release from antibiotic-loaded polymethylmethacrylate beads after 5 years of implantation. Biomaterials 2003;24:1829-31.

[161] Rolauffs B, Bernhardt T, von Eiff C, Hart M, Bettin D. Osteopetrosis, femoral fracture, and chronic osteomyelitis caused by Staphylococcus aureus small colony variants (SCV) treated by girdlestone resection – 6-year follow-up. Arch Orthop Trauma Surg 2002;122:547-50.

[162] Ribeiro CC, Barrias CC, Barbosa MA. Calcium phosphate-alginate microspheres as enzyme delivery matrices. Biomaterials 2004;25:4363-73.

[163] Pioletti DP, Takei H, Lin T, Van Landuyt P, Jun Ma Q, Yong Kwon S, et al. The effects of calcium phosphate cement particles on osteoblast functions. Biomaterials 2000;21:1103-14.

[164] Bose S, Tarafder S. Calcium phosphate ceramic systems in growth factor and drug delivery for bone tissue engineering: A review. Acta Biomaterialia 2012;8:1401-21.

[165] Salonen J, Kaukonen AM, Hirvonen J, Lehto V-P. Mesoporous silicon in drug delivery applications. Journal of Pharmaceutical Sciences 2008;97:632-53.

[166] Anglin EJ, Cheng L, Freeman WR, Sailor MJ. Porous silicon in drug delivery devices and materials. Advanced drug delivery reviews 2008;60:1266-77.

[167] Chen J-F, Ding H-M, Wang J-X, Shao L. Preparation and characterization of porous hollow silica nanoparticles for drug delivery application. Biomaterials 2004;25:723-7.

[168] Li Z-Z, Wen L-X, Shao L, Chen J-F. Fabrication of porous hollow silica nanoparticles and their applications in drug release control. Journal of Controlled Release 2004;98:245-54.

[169] Morgan TT, Muddana HS, Altinoglu EI, Rouse SM, Tabakovic A, Tabouillot T, et al. Encapsulation of organic molecules in calcium phosphate nanocomposite particles for intracellular imaging and drug delivery. Nano letters 2008;8:4108-15.

[170] Lai C-Y, Trewyn BG, Jeftinija DM, Jeftinija K, Xu S, Jeftinija S, et al. A mesoporous silica nanosphere-based carrier system with chemically removable CdS nanoparticle caps for stimuli-responsive controlled release of neurotransmitters and drug molecules. Journal of the American Chemical Society 2003;125:4451-9.

[171] Ginebra MP, Espanol M, Montufar EB, Perez RA, Mestres G. New processing approaches in calcium phosphate cements and their applications in regenerative medicine. Acta Biomaterialia 2010;6:2863-73.

[172] Radin S, Ducheyne P, Kamplain T, Tan B. Silica sol-gel for the controlled release of antibiotics. I. Synthesis, characterization, and in vitro release. Journal of biomedical materials research 2001;57:313-20.

[173] Domingues ZR, Cortés ME, Gomes TA, Diniz HF, Freitas CS, Gomes JB, et al. Bioactive glass as a drug delivery system of tetracycline and tetracycline associated with β-cyclodextrin. Biomaterials 2004;25:327-33.

[174] Shinto Y, Uchida A, Korkusuz F, Araki N, Ono K. Calcium hydroxyapatite ceramic used as a delivery system for antibiotics. Journal of Bone & Joint Surgery, British Volume 1992;74:600-4.

[175] Barroug A, Glimcher MJ. Hydroxyapatite crystals as a local delivery system for cisplatin: adsorption and release of cisplatin in vitro. Journal of orthopaedic research 2002;20:274-80.

[176] Shahverdi AR, Fakhimi A, Shahverdi HR, Minaian S. Synthesis and effect of silver nanoparticles on the antibacterial activity of different antibiotics against< i> Staphylococcus aureus</i> and< i> Escherichia coli</i>. Nanomedicine: Nanotechnology, Biology and Medicine 2007;3:168-71.

[177] Ueno Y, Futagawa H, Takagi Y, Ueno A, Mizushima Y. Drug-incorporating calcium carbonate nanoparticles for a new delivery system. Journal of Controlled Release 2005;103:93-8.

[178] Hanifi A, Fathi MH, Sadeghi HM, Varshosaz J. Mg2+ substituted calcium phosphate nano particles synthesis for non viral gene delivery application. J Mater Sci Mater Med 2010;21:2393-401.

[179] Dasgupta S, Banerjee SS, Bandyopadhyay A, Bose S. Zn- and Mg-doped hydroxyapatite nanoparticles for controlled release of protein. Langmuir 2010;26:4958-64.

[180] Stigter M, Bezemer J, De Groot K, Layrolle P. Incorporation of different antibiotics into carbonated hydroxyapatite coatings on titanium implants, release and antibiotic efficacy. Journal of Controlled Release 2004;99:127-37.

[181] Stigter M, de Groot K, Layrolle P. Incorporation of tobramycin into biomimetic hydroxyapatite coating on titanium. Biomaterials 2002;23:4143-53.

[182] Maia MdMD, Vasconcelos EAd, Maia PFCdMD, Maciel JdC, Cajueiro KRR, Silva MdPCd, et al. Immobilization of urease on vapour phase stain etched porous silicon. Process Biochemistry 2007;42:429-33.

[183] Wan Y, Zhao D. On the controllable soft-templating approach to mesoporous silicates. Chemical reviews 2007;107:2821-60.

[184] Buriak JM, Allen MJ. Lewis acid mediated functionalization of porous silicon with substituted alkenes and alkynes. Journal of the American Chemical Society 1998;120:1339-40.

[185] Horcajada P, Rámila A, Pérez-Pariente J, Vallet R, amp, x, et al. Influence of pore size of MCM-41 matrices on drug delivery rate. Microporous and Mesoporous Materials 2004;68:105-9.

[186] Auffan M, Rose J, Bottero J-Y, Lowry GV, Jolivet J-P, Wiesner MR. Towards a definition of inorganic nanoparticles from an environmental, health and safety perspective. Nature nanotechnology 2009;4:634-41.

[187] Zhao D, Feng J, Huo Q, Melosh N, Fredrickson GH, Chmelka BF, et al. Triblock copolymer syntheses of mesoporous silica with periodic 50 to 300 angstrom pores. Science 1998;279:548-52.

[188] Tanaka T, Mangala LS, Vivas-Mejia PE, Nieves-Alicea R, Mann AP, Mora E, et al. Sustained small interfering RNA delivery by mesoporous silicon particles. Cancer research 2010;70:3687-96.

[189] Vaccari L, Canton D, Zaffaroni N, Villa R, Tormen M, di Fabrizio E. Porous silicon as drug carrier for controlled delivery of doxorubicin anticancer agent. Microelectronic engineering 2006;83:1598-601.

[190] Li X, John JS, Coffer JL, Chen Y, Pinizzotto RF, Newey J, et al. Porosified silicon wafer structures impregnated with platinum anti-tumor compounds: Fabrication, characterization, and diffusion studies. Biomedical Microdevices 2000;2:265-72.

[191] Anglin EJ, Schwartz MP, Ng VP, Perelman LA, Sailor MJ. Engineering the chemistry and nanostructure of porous silicon Fabry-Pérot films for loading and release of a steroid. Langmuir 2004;20:11264-9.

[192] Salonen J, Laitinen L, Kaukonen A, Tuura J, Björkqvist M, Heikkilä T, et al. Mesoporous silicon microparticles for oral drug delivery: loading and release of five model drugs. Journal of Controlled Release 2005;108:362-74.

[193] Foraker AB, Walczak RJ, Cohen MH, Boiarski TA, Grove CF, Swaan PW. Microfabricated porous silicon particles enhance paracellular delivery of insulin across intestinal Caco-2 cell monolayers. Pharm Res 2003;20:110-6.

[194] Lai C-Y, Trewyn BG, Jeftinija DM, Jeftinija K, Xu S, Jeftinija S, et al. A Mesoporous Silica Nanosphere-Based Carrier System with Chemically Removable CdS Nanoparticle Caps for Stimuli-Responsive Controlled Release of Neurotransmitters and Drug Molecules. Journal of the American Chemical Society 2003;125:4451-9.

[195] Torney F, Trewyn BG, Lin VSY, Wang K. Mesoporous silica nanoparticles deliver DNA and chemicals into plants. Nat Nano 2007;2:295-300.

[196] Nel A, Xia T, Mädler L, Li N. Toxic Potential of Materials at the Nanolevel. Science 2006;311:622-7.

[197] Rothenfluh DA, Hubbell JA. Integration column: Biofunctional polymeric nanoparticles for spatio-temporal control of drug delivery and biomedical applications. Integrative Biology 2009;1:446-51.

[198] Colvin VL. The potential environmental impact of engineered nanomaterials. Nature biotechnology 2003;21:1166-70.

[199] Lacerda L, Bianco A, Prato M, Kostarelos K. Carbon nanotubes as nanomedicines: From toxicology to pharmacology. Advanced drug delivery reviews 2006;58:1460-70.

[200] He Q, Shi J. Mesoporous silica nanoparticle based nano drug delivery systems: synthesis, controlled drug release and delivery, pharmacokinetics and biocompatibility. Journal of Materials Chemistry 2011;21:5845-55.

[201] Lin Y-S, Haynes CL. Impacts of Mesoporous Silica Nanoparticle Size, Pore Ordering, and Pore Integrity on Hemolytic Activity. Journal of the American Chemical Society 2010;132:4834-42.

[202] Yu K, Grabinski C, Schrand A, Murdock R, Wang W, Gu B, et al. Toxicity of amorphous silica nanoparticles in mouse keratinocytes. Journal of Nanoparticle Research 2009;11:15-24.

[203] Ginebra M, Fernandez E, De Maeyer E, Verbeeck R, Boltong M, Ginebra J, et al. Setting reaction and hardening of an apatitic calcium phosphate cement. Journal of Dental Research 1997;76:905-12.

[204] Takagi S, Chow LC, Ishikawa K. Formation of hydroxyapatite in new calcium phosphate cements. Biomaterials 1998;19:1593-9.

[205] Ooms E, Wolke J, Van Der Waerden J, Jansen J. Trabecular bone response to injectable calcium phosphate (Ca-P) cement. Journal of biomedical materials research 2002;61:9-18.

[206] Gbureck U, Vorndran E, Barralet JE. Modeling vancomycin release kinetics from microporous calcium phosphate ceramics comparing static and dynamic immersion conditions. Acta Biomaterialia 2008;4:1480-6.

[207] Bohner M, Lemaître J, Landuyt PV, Zambelli P-Y, Merkle HP, Gander B. Gentamicin-loaded hydraulic calcium phosphate bone cement as antibiotic delivery system. Journal of Pharmaceutical Sciences 1997;86:565-72.

[208] Ethell MT, Bennett RA, Brown MP, Merritt K, Davidson JS, Tran T. In Vitro Elution of Gentamicin, Amikacin, and Ceftiofur From Polymethylmethacrylate and Hydroxyapatite Cement. Veterinary Surgery 2000;29:375-82.

[209] Tahara Y, Ishii Y. Apatite cement containing cis-diamminedichloroplatinum implanted in rabbit femur for sustained release of the anticancer drug and bone formation. Journal of Orthopaedic Science 2001;6:556-65.

[210] Joosten U, Joist A, Frebel T, Brandt B, Diederichs S, von Eiff C. Evaluation of an in situ setting injectable calcium phosphate as a new carrier material for gentamicin in the treatment of chronic osteomyelitis: Studies in vitro and in vivo. Biomaterials 2004;25:4287-95.

[211] Sasaki T, Ishibashi Y, Katano H, Nagumo A, Toh S. In Vitro Elution of Vancomycin from Calcium Phosphate Cement. The Journal of Arthroplasty 2005;20:1055-9.

[212] Ratier A, Freche M, Lacout JL, Rodriguez F. Behaviour of an injectable calcium phosphate cement with added tetracycline. International Journal of Pharmaceutics 2004;274:261-8.

[213] Jiang P-J, Patel S, Gbureck U, Caley R, Grover LM. Comparing the efficacy of three bioceramic matrices for the release of vancomycin hydrochloride. Journal of Biomedical Materials Research Part B: Applied Biomaterials 2010;93B:51-8.

[214] Urabe K, Naruse K, Hattori H, Hirano M, Uchida K, Onuma K, et al. In vitro comparison of elution characteristics of vancomycin from calcium phosphate cement and polymethylmethacrylate. Journal of Orthopaedic Science 2009;14:784-93.

[215] Böttcher H, Kallies K-H, Haufe H. Model investigations of controlled release of bioactive compounds from thin metal oxide layers. Journal of Sol-Gel Science and Technology 1997;8:651-4.

[216] Nicoll SB, Radin S, Santos EM, Tuan RS, Ducheyne P. < i> In vitro</i> release kinetics of biologically active transforming growth factor-β1 from a novel porous glass carrier. Biomaterials 1997;18:853-9.

[217] Unger K, Rupprecht H, Valentin B, Kircher W. The use of porous and surface modified silicas as drug delivery and stabilizing agents. Drug Development and Industrial Pharmacy 1983;9:69-91.

[218] Munusamy P, Seleem MN, Alqublan H, Tyler Jr R, Sriranganathan N, Pickrell G. Targeted drug delivery using silica xerogel systems to treat diseases due to intracellular pathogens. Materials Science and Engineering: C 2009;29:2313-8.

[219] Maver U, Godec A, Bele M, Planinšek O, Gaberšček M, Srčič S, et al. Novel hybrid silica xerogels for stabilization and controlled release of drug. International journal of pharmaceutics 2007;330:164-74.

[220] Qu F, Zhu G, Lin H, Zhang W, Sun J, Li S, et al. A controlled release of ibuprofen by systematically tailoring the morphology of mesoporous silica materials. Journal of Solid State Chemistry 2006;179:2027-35.

[221] Kortesuo P, Ahola M, Karlsson S, Kangasniemi I, Yli-Urpo A, Kiesvaara J. Silica xerogel as an implantable carrier for controlled drug delivery—evaluation of drug distribution and tissue effects after implantation. Biomaterials 2000;21:193-8.

[222] Kortesuo P, Ahola M, Kangas M, Yli-Urpo A, Kiesvaara J, Marvola M. In vitro release of dexmedetomidine from silica xerogel monoliths: effect of sol-gel synthesis parameters. International journal of pharmaceutics 2001;221:107-14.

[223] Radin S, Chen T, Ducheyne P. The controlled release of drugs from emulsified, sol gel processed silica microspheres. Biomaterials 2009;30:850-8.

[224] Ro JC, In JC. Structures and properties of silica gels prepared by the sol—gel method. Journal of non-crystalline solids 1991;130:8-17.

[225] Curran MD, Stiegman A. Morphology and pore structure of silica xerogels made at low pH. Journal of non-crystalline solids 1999;249:62-8.

[226] Pope EJ, Mackenzie J. Sol-gel processing of silica: II. The role of the catalyst. Journal of non-crystalline solids 1986;87:185-98.

[227] Santos EM, Radin S, Ducheyne P. Sol–gel derived carrier for the controlled release of proteins. Biomaterials 1999;20:1695-700.

[228] Xue JM, Tan CH, Lukito D. Biodegradable polymer–silica xerogel composite microspheres for controlled release of gentamicin. Journal of Biomedical Materials Research Part B: Applied Biomaterials 2006;78B:417-22.

[229] Kortesuo P, Ahola M, Karlsson S, Kangasniemi I, Kiesvaara J, Yli-Urpo A. Sol-gel-processed sintered silica xerogel as a carrier in controlled drug delivery. Journal of biomedical materials research 1999;44:162-7.

[230] Hofmann MP, Mohammed AR, Perrie Y, Gbureck U, Barralet JE. High-strength resorbable brushite bone cement with controlled drug-releasing capabilities. Acta Biomaterialia 2009;5:43-9.

[231] Lopez-Heredia MA, Bernard Kamphuis GJ, Thüne PC, Cumhur Öner F, Jansen JA, Frank Walboomers X. An injectable calcium phosphate cement for the local delivery of paclitaxel to bone. Biomaterials 2011;32:5411-6.

[232] Otsuka M, Matsuda Y, Suwa Y, Fox JL, Higuchi WI. A novel skeletal drug-delivery system using self-setting calcium phosphate cement. 3. Physicochemical properties and drug-release rate of bovine insulin and bovine albumin. Journal of Pharmaceutical Sciences 1994;83:255-8.

[233] Ginebra M, Rilliard A, Fernández E, Elvira C, San Roman J, Planell J. Mechanical and rheological improvement of a calcium phosphate cement by the addition of a polymeric drug. Journal of biomedical materials research 2001;57:113-8.

[234] Gbureck U, Barralet JE, Spatz K, Grover LM, Thull R. Ionic modification of calcium phosphate cement viscosity. Part I: hypodermic injection and strength improvement of apatite cement. Biomaterials 2004;25:2187-95.

[235] Otsuka M, Nakahigashi Y, Matsuda Y, Fox JL, Higuchi WI, Sugiyama Y. Effect of geometrical cement size on in vitro and in vivo indomethacin release from self-setting apatite cement. Journal of Controlled Release 1998;52:281-9.

[236] Kisanuki O, Yajima H, Umeda T, Takakura Y. Experimental study of calcium phosphate cement impregnated with dideoxy-kanamycin B. Journal of Orthopaedic Science 2007;12:281-8.

[237] Ratier A, Freche M, Lacout J, Rodriguez F. Behaviour of an injectable calcium phosphate cement with added tetracycline. International Journal of Pharmaceutics 2004;274:261-8.

[238] Ratier A, Gibson I, Best S, Freche M, Lacout J, Rodriguez F. Setting characteristics and mechanical behaviour of a calcium phosphate bone cement containing tetracycline. Biomaterials 2001;22:897-901.

[239] Roveri N, Morpurgo M, Palazzo B, Parma B, Vivi L. Silica xerogels as a delivery system for the controlled release of different molecular weight heparins. Analytical and bioanalytical chemistry 2005;381:601-6.

[240] Mal NK, Fujiwara M, Tanaka Y. Photocontrolled reversible release of guest molecules from coumarin-modified mesoporous silica. Nature 2003;421:350-3.

[241] Rich J, Jaakkola T, Tirri T, Närhi T, Yli-Urpo A, Seppälä J. In vitro evaluation of poly (< i> ε</i>-caprolactone-co-DL-lactide)/bioactive glass composites. Biomaterials 2002;23:2143-50.

[242] Arcos D, Peña J, Vallet-Regí M. Influence of a SiO2-CaO-P2O5 sol-gel glass on the bioactivity and controlled release of ceramic/polymer/antibiotic mixed materials. Chemistry of Materials 2003;15:4132-8.

[243] Zhang G, Suggs LJ. Matrices and scaffolds for drug delivery in vascular tissue engineering. Advanced drug delivery reviews 2007;59:360-73.

[244] Gilbert TW, Stewart-Akers AM, Simmons-Byrd A, Badylak SF. Degradation and Remodeling of Small Intestinal Submucosa in Canine Achilles Tendon Repair. The Journal of Bone & Joint Surgery 2007;89:621-30.

[245] Hench LL, Wilson J. An introduction to bioceramics: World Scientific; 1993.

[246] Suchanek W, Yoshimura M. Processing and properties of hydroxyapatite-based biomaterials for use as hard tissue replacement implants. Journal of Materials Research 1998;13:94-117.

[247] Dong J, Kojima H, Uemura T, Kikuchi M, Tateishi T, Tanaka J. In vivo evaluation of a novel porous hydroxyapatite to sustain osteogenesis of transplanted bone marrow-derived osteoblastic cells. Journal of biomedical materials research 2001;57:208-16.

[248] Damien E, Hing K, Saeed S, Revell PA. A preliminary study on the enhancement of the osteointegration of a novel synthetic hydroxyapatite scaffold in vivo. Journal of Biomedical Materials Research Part A 2003;66:241-6.

[249] Kuboki Y, Takita H, Kobayashi D, Tsuruga E, Inoue M, Murata M, et al. BMP-Induced osteogenesis on the surface of hydroxyapatite with geometrically feasible and nonfeasible structures: Topology of osteogenesis. Journal of biomedical materials research 1998;39:190-9.

[250] Woodard JR, Hilldore AJ, Lan SK, Park CJ, Morgan AW, Eurell JAC, et al. The mechanical properties and osteoconductivity of hydroxyapatite bone scaffolds with multi-scale porosity. Biomaterials 2007;28:45-54.

[251] Mastrogiacomo M, Scaglione S, Martinetti R, Dolcini L, Beltrame F, Cancedda R, et al. Role of scaffold internal structure on in vivo bone formation in macroporous calcium phosphate bioceramics. Biomaterials 2006;27:3230-7.

[252] Yang S, Leong K-F, Du Z, Chua C-K. The design of scaffolds for use in tissue engineering. Part II. Rapid prototyping techniques. Tissue Engineering 2002;8:1-11.

[253] Ramay HR, Zhang M. Preparation of porous hydroxyapatite scaffolds by combination of the gel-casting and polymer sponge methods. Biomaterials 2003;24:3293-302.

[254] Almirall A, Larrecq G, Delgado JA, Martínez S, Planell JA, Ginebra MP. Fabrication of low temperature macroporous hydroxyapatite scaffolds by foaming and hydrolysis of an α-TCP paste. Biomaterials 2004;25:3671-80.

[255] Uchida A, Shinto Y, Araki N, Ono K. Slow release of anticancer drugs from porous calcium hydroxyapatite ceramic. Journal of orthopaedic research 1992;10:440-5.

[256] Daculsi G. Biphasic calcium phosphate concept applied to artificial bone, implant coating and injectable bone substitute. Biomaterials 1998;19:1473-8.

[257] Guicheux J, Gauthier O, Aguado E, Heymann D, Pilet P, Couillaud S, et al. Growth hormone-loaded macroporous calcium phosphate ceramic: In vitro biopharmaceutical characterization and preliminary in vivo study. Journal of biomedical materials research 1998;40:560-6.

[258] Murugan R, Ramakrishna S. Production of ultra-fine bioresorbable carbonated hydroxyapatite. Acta Biomaterialia 2006;2:201-6.

[259] LeGeros RZ. Calcium phosphates in oral biology and medicine. Monogr Oral Sci 1991;15:1-201.

[260] Pan HB, Li ZY, Lam WM, Wong JC, Darvell BW, Luk KDK, et al. Solubility of strontium-substituted apatite by solid titration. Acta Biomaterialia 2009;5:1678-85.

[261] Christoffersen J, Christoffersen MR, Kolthoff N, Bärenholdt O. Effects of strontium ions on growth and dissolution of hydroxyapatite and on bone mineral detection. Bone 1997;20:47-54.

[262] Andersson Ö. Glass transition temperature of glasses in the SiO2-Na2O-CaO-P2O5-Al2O3-B2O3 system. Journal of Materials Science: Materials in Medicine 1992;3:326-8.

[263] Hench LL. Bioceramics: From Concept to Clinic. Journal of the American Ceramic Society 1991;74:1487-510.

[264] Hench LL. Biomaterials: a forecast for the future. Biomaterials 1998;19:1419-23.

[265] Sepulveda P, Jones JR, Hench LL. In vitro dissolution of melt-derived 45S5 and sol-gel derived 58S bioactive glasses. Journal of biomedical materials research 2002;61:301-11.

[266] Cerruti MG, Greenspan D, Powers K. An analytical model for the dissolution of different particle size samples of Bioglass® in TRIS-buffered solution. Biomaterials 2005;26:4903-11.

[267] Yuan H, de Bruijn JD, Zhang X, van Blitterswijk CA, de Groot K. Bone induction by porous glass ceramic made from Bioglass®(45S5). Journal of biomedical materials research 2001;58:270-6.

[268] Chen QZ, Thompson ID, Boccaccini AR. 45S5 Bioglass< sup>®</sup>-derived glass–ceramic scaffolds for bone tissue engineering. Biomaterials 2006;27:2414-25.

[269] Kaufmann E, Ducheyne P, Shapiro I. Effect of varying physical properties of porous, surface modified bioactive glass 45S5 on osteoblast proliferation and maturation. Journal of biomedical materials research 2000;52:783-96.

[270] Chen QZ, Thompson ID, Boccaccini AR. 45S5 Bioglass®-derived glass–ceramic scaffolds for bone tissue engineering. Biomaterials 2006;27:2414-25.

[271] Wu C, Luo Y, Cuniberti G, Xiao Y, Gelinsky M. Three-dimensional printing of hierarchical and tough mesoporous bioactive glass scaffolds with a controllable pore architecture, excellent mechanical strength and mineralization ability. Acta Biomaterialia 2011;7:2644-50.

[272] Nandi SK, Kundu B, Mukherjee P, Mandal TK, Datta S, De DK, et al. In vitro and in vivo release of cefuroxime axetil from bioactive glass as an implantable delivery system in experimental osteomyelitis. Ceramics International 2009;35:3207-16.

[273] Onuma K, Ito A. Cluster Growth Model for Hydroxyapatite. Chemistry of Materials 1998;10:3346-51.

[274] Ito A, Maekawa K, Tsutsumi S, Ikazaki F, Tateishi T. Solubility product of OH-carbonated hydroxyapatite. Journal of biomedical materials research 1997;36:522-8.

[275] Arcos D, Vallet-Regí M. Sol–gel silica-based biomaterials and bone tissue regeneration. Acta Biomaterialia 2010;6:2874-88.

[276] Kong L, Gao Y, Cao W, Gong Y, Zhao N, Zhang X. Preparation and characterization of nano-hydroxyapatite/chitosan composite scaffolds. Journal of Biomedical Materials Research Part A 2005;75:275-82.

[277] Wang L, Li Y, Zuo Y, Zhang L, Zou Q, Cheng L, et al. Porous bioactive scaffold of aliphatic polyurethane and hydroxyapatite for tissue regeneration. Biomedical Materials 2009;4:025003.

[278] Wei G, Ma PX. Structure and properties of nano-hydroxyapatite/polymer composite scaffolds for bone tissue engineering. Biomaterials 2004;25:4749-57.

[279] Niu X, Feng Q, Wang M, Guo X, Zheng Q. Porous nano-HA/collagen/PLLA scaffold containing chitosan microspheres for controlled delivery of synthetic peptide derived from BMP-2. Journal of Controlled Release 2009;134:111-7.

[280] Yang C-C, Lin C-C, Liao J-W, Yen S-K. Vancomycin–chitosan composite deposited on post porous hydroxyapatite coated Ti6Al4V implant for drug controlled release. Materials Science and Engineering: C 2013;33:2203-12.

[281] Boehler RM, Shin S, Fast AG, Gower RM, Shea LD. A PLG/HAp composite scaffold for lentivirus delivery. Biomaterials 2013;34:5431-8.

[282] Kim H-W, Knowles JC, Kim H-E. Hydroxyapatite/poly(ε-caprolactone) composite coatings on hydroxyapatite porous bone scaffold for drug delivery. Biomaterials 2004;25:1279-87.

[283] Brook IM, van Noort R. Drug release from acrylic polymers via channels and cracks: In vitro studies with hydrocortisone. Biomaterials 1985;6:281-5.

[284] Lee G-S, Park J-H, Shin US, Kim H-W. Direct deposited porous scaffolds of calcium phosphate cement with alginate for drug delivery and bone tissue engineering. Acta Biomaterialia 2011;7:3178-86.

[285] Li W, Nooeaid P, Roether JA, Schubert DW, Boccaccini AR. Preparation and characterization of vancomycin releasing PHBV coated 45S5 Bioglass®-based glass–ceramic scaffolds for bone tissue engineering. Journal of the European Ceramic Society.

[286] Wu C, Zhang Y, Zhu Y, Friis T, Xiao Y. Structure–property relationships of silk-modified mesoporous bioglass scaffolds. Biomaterials 2010;31:3429-38.

[287] Soriano I, Evora C. Formulation of calcium phosphates/poly (< i> d</i>,< i> l</i>-lactide) blends containing gentamicin for bone implantation. Journal of Controlled Release 2000;68:121-34.

[288] Schnieders J, Gbureck U, Thull R, Kissel T. Controlled release of gentamicin from calcium phosphate—poly (lactic acid-< i> co</i>-glycolic acid) composite bone cement. Biomaterials 2006;27:4239-49.

[289] Itoh S, Kikuchi M, Takakuda K, Koyama Y, Matsumoto HN, Ichinose S, et al. The biocompatibility and osteoconductive activity of a novel hydroxyapatite/collagen composite biomaterial, and its function as a carrier of rhBMP-2. Journal of biomedical materials research 2001;54:445-53.

[290] Habraken WJEM, de Jonge LT, Wolke JGC, Yubao L, Mikos AG, Jansen JA. Introduction of gelatin microspheres into an injectable calcium phosphate cement. Journal of Biomedical Materials Research Part A 2008;87A:643-55.

[291] Habraken W, Wolke J, Mikos A, Jansen J. Injectable PLGA microsphere/calcium phosphate cements: physical properties and degradation characteristics. Journal of Biomaterials Science, Polymer Edition 2006;17:1057-74.

[292] El-Ghannam A. Silica-Calcium Phosphate Bioactive Composite For Improved Synthetic Graft Resorbability and Tissue Regeneration US2007.

[293] El-Ghannam AR. Advanced bioceramic composite for bone tissue engineering: design principles and structure-bioactivity relationship. J Biomed Mater Res A 2004;69:490-501.

[294] Gupta G, El-Ghannam A, Kirakodu S, Khraisheh M, Zbib H. Enhancement of osteoblast gene expression by mechanically compatible porous Si-rich nanocomposite. Journal of Biomedical Materials Research Part B: Applied Biomaterials 2007;81:387-96.

[295] Ning C, Greish Y, El-Ghannam A. Crystallization behavior of silica-calcium phosphate biocomposites: XRD and FTIR studies. Journal of Materials Science: Materials in Medicine 2004;15:1227-35.

[296] El-Ghannam A, Ning CQ, Mehta J. Cyclosilicate nanocomposite: a novel resorbable bioactive tissue engineering scaffold for BMP and bone-marrow cell delivery. J Biomed Mater Res A 2004;71:377-90.

[297] El-Ghannam A, Ning C. Effect of bioactive ceramic dissolution on the mechanism of bone mineralization and guided tissue growth in vitro. Journal of Biomedical Materials Research Part A 2006;76:386-97.

[298] El-Ghannam A, Ahmed K, Omran M. Nanoporous delivery system to treat osteomyelitis and regenerate bone: gentamicin release kinetics and bactericidal effect. J Biomed Mater Res B Appl Biomater 2005;73:277-84.

[299] El-Ghannam A, Jahed K, Govindaswami M. Resorbable bioactive ceramic for treatment of bone infection. Journal of Biomedical Materials Research Part A 2010;94:308-16.

[300] El-Ghannam A, Ricci K, Malkawi A, Jahed K, Vedantham K, Wyan H, et al. A ceramic-based anticancer drug delivery system to treat breast cancer. J Mater Sci Mater Med 2010;21:2701-10.

[301] Vedantham K, Swet JH, McKillop IH, El-Ghannam A. Evaluation of a bioresorbable drug delivery system for the treatment of hepatocellular carcinoma. Journal of Biomedical Materials Research Part A 2012;100:432-40.

[302] Schnieders J, Gbureck U, Vorndran E, Schossig M, Kissel T. The effect of porosity on drug release kinetics from vancomycin microsphere/calcium phosphate cement composites. Journal of Biomedical Materials Research Part B: Applied Biomaterials 2011;99:391-8.

[303] Wu C, Miron R, Sculean A, Kaskel S, Doert T, Schulze R, et al. Proliferation, differentiation and gene expression of osteoblasts in boron-containing associated with dexamethasone deliver from mesoporous bioactive glass scaffolds. Biomaterials 2011;32:7068-78.

[304] Netz D, Sepulveda P, Pandolfelli V, Spadaro A, Alencastre J, Bentley M, et al. Potential use of gelcasting hydroxyapatite porous ceramic as an implantable drug delivery system. International Journal of Pharmaceutics 2001;213:117-25.

[305] Soundrapandian C, Datta S, Kundu B, Basu D, Sa B. Porous bioactive glass scaffolds for local drug delivery in osteomyelitis: development and in vitro characterization. AAPS PharmSciTech 2010;11:1675-83.

[306] Gbureck U, Vorndran E, Müller FA, Barralet JE. Low temperature direct 3D printed bioceramics and biocomposites as drug release matrices. Journal of Controlled Release 2007;122:173-80.

[307] Konishi M, Tabata Y, Kariya M, Hosseinkhani H, Suzuki A, Fukuhara K, et al. In vivo anti-tumor effect of dual release of cisplatin and adriamycin from biodegradable gelatin hydrogel. Journal of Controlled Release 2005;103:7-19.

[308] Moojen DJF, Hentenaar B, Charles Vogely H, Verbout AJ, Castelein RM, Dhert WJ. In vitro release of antibiotics from commercial PMMA beads and articulating hip spacers. The Journal of Arthroplasty 2008;23:1152-6.

[309] Wu C, Fan W, Gelinsky M, Xiao Y, Simon P, Schulze R, et al. Bioactive SrO–SiO< sub> 2</sub> glass with well-ordered mesopores: Characterization, physiochemistry and biological properties. Acta Biomaterialia 2011;7:1797-806.

[310] Wu C, Fan W, Zhu Y, Gelinsky M, Chang J, Cuniberti G, et al. Multifunctional magnetic mesoporous bioactive glass scaffolds with a hierarchical pore structure. Acta Biomaterialia 2011;7:3563-72.

[311] Zhu Y, Kaskel S. Comparison of the< i> in vitro</i> bioactivity and drug release property of mesoporous bioactive glasses (MBGs) and bioactive glasses (BGs) scaffolds. Microporous and Mesoporous Materials 2009;118:176-82.

[312] Gautier H, Daculsi G, Merle C. Association of vancomycin and calcium phosphate by dynamic compaction: in vitro characterization and microbiological activity. Biomaterials 2001;22:2481-7.

[313] Kundu B, Lemos A, Soundrapandian C, Sen P, Datta S, Ferreira J, et al. Development of porous HAp and β-TCP scaffolds by starch consolidation with foaming method and drug-chitosan bilayered scaffold based drug delivery system. Journal of Materials Science: Materials in Medicine 2010;21:2955-69.

[314] Xia W, Chang J. Well-ordered mesoporous bioactive glasses (MBG): a promising bioactive drug delivery system. Journal of Controlled Release 2006;110:522-30.

[315] Zhang Y, Zhang M. Calcium phosphate/chitosan composite scaffolds for controlled in vitro antibiotic drug release. Journal of biomedical materials research 2002;62:378-86.

[316] Shi X, Wang Y, Ren L, Zhao N, Gong Y, Wang D-A. Novel mesoporous silica-based antibiotic releasing scaffold for bone repair. Acta Biomaterialia 2009;5:1697-707.

[317] Berrada M, Yang Z, Lehnert S. Tumor treatment by sustained intratumoral release of 5-fluorouracil: effects of drug alone and in combined treatments. International Journal of Radiation Oncology* Biology* Physics 2002;54:1550-7.

[318] El-Ghannam A, Jahed K, Govindaswami M. Resorbable bioactive ceramic for treatment of bone infection. J Biomed Mater Res A 2010;94:308-16.

[319] Vedantham K, Swet JH, McKillop IH, El-Ghannam A. Evaluation of a bioresorbable drug delivery system for the treatment of hepatocellular carcinoma. J Biomed Mater Res A 2011.

[320] El-Ghannam A, Ning C. Effect of bioactive ceramic dissolution on the mechanism of bone mineralization and guided tissue growth in vitro. Journal of Biomedical Materials Research Part A 2006;76:386-97.

[321] Kangasniemi I, de Groot K, Becht J, Yli-Urpo A. Preparation of dense hydroxylapatite or rhenanite containing bioactive glass composites. Journal of biomedical materials research 1992;26:663-74.

[322] Ramselaar M, Driessens F, Kalk W, De Wijn J, Van Mullem P. Biodegradation of four calcium phosphate ceramics; in vivo rates and tissue interactions. Journal of Materials Science: Materials in Medicine 1991;2:63-70.

[323] Ramselaar M, Van Mullem P, Kalk W, Driessens F, De Wijn J, Stols A. In vivo reactions to particulate rhenanite and particulate hydroxylapatite after implantation in tooth sockets. Journal of Materials Science: Materials in Medicine 1993;4:311-7.

[324] Knabe C, Berger G, Gildenhaar R, Howlett CR, Markovic B, Zreiqat H. The functional expression of human bone-derived cells grown on rapidly resorbable calcium phosphate ceramics. Biomaterials 2004;25:335-44.

[325] Knabe C, Gildenhaar R, Berger G, Ostapowicz W, Fitzner R, Radlanski RJ, et al. Morphological evaluation of osteoblasts cultured on different calcium phosphate ceramics. Biomaterials 1997;18:1339-47.

[326] Li P, Ohtsuki C, Kokubo T, Nakanishi K, Soga N, Nakamura T, et al. Process of formation of bone-like apatite layer on silica gel. Journal of Materials Science: Materials in Medicine 1993;4:127-31.

[327] Miyaji F, Iwai M, Kokubo T, Nakamura T. Chemical surface treatment of silicone for inducing its bioactivity. Journal of Materials Science: Materials in Medicine 1998;9:61-5.

[328] Coh S, Vanderbilt D. Structural stability and lattice dynamics of SiO_ {2} cristobalite. Physical Review B 2008;78:054117.

[329] Meseguer-Olmo L, Bernabeu-Escaplez A, Vallet-Regí M, Aznar-Cervantes S, Vicente-Ortega V, Alcaraz-Baños M, et al. Bone tissue engineering. Design and development of biologically active vitroceramic-based hybrid materials to be used as bone substitutes. Revista española de cirugía ortopédica y traumatología (English edition) 2010;54:59-68.

[330] Mirsaneh M, Reaney IM, Hatton PV, Bhakta S, James PF. Effect of P< sub> 2</sub> O< sub> 5</sub> on the early stage crystallization of K-fluorrichterite glass–ceramics. Journal of Non-Crystalline Solids 2008;354:3362-8.

[331] da Silva AC, Aparecida A, Braga F. Dispersed hydroxyapatite bioglass 45S5 composites: comparative evaluation of the use of bovine bone and synthetic hydroxyapatite. Materials Science Forum: Trans Tech Publ; 2012. p. 1147-52.

[332] Knotts R, Jalota S, Bhaduri S, Tas A. Synthesis of Rhenanite (β-NaCaPO4)-Apatitic Calcium Phosphate Biphasics for Skeletal Repair. Advances in Bioceramics and Porous Ceramics: Ceramic Engineering and Science Proceedings, Volume 29, Issue 7 2009:151-64.

[333] McCusker L, Von Dreele R, Cox D, Louer D, Scardi P. Rietveld refinement guidelines. Journal of Applied Crystallography 1999;32:36-50.

[334] Kokubo T. Bioactive glass ceramics: properties and applications. Biomaterials 1991;12:155-63.

[335] Kokubo T, Takadama H. How useful is SBF in predicting in vivo bone bioactivity? Biomaterials 2006;27:2907-15.

[336] Fidalgo A, Ilharco LM. The defect structure of sol–gel-derived silica/polytetrahydrofuran hybrid films by FTIR. Journal of Non-Crystalline Solids 2001;283:144-54.

[337] ElBatal H, Azooz M, Khalil E, Soltan Monem A, Hamdy Y. Characterization of some bioglass–ceramics. Materials chemistry and physics 2003;80:599-609.

[338] Djošić M, Mišković-Stanković V, Kačarević-Popović Z, Jokić B, Bibić N, Mitrić M, et al. Electrochemical synthesis of nanosized monetite powder and its electrophoretic deposition on titanium. Colloids and Surfaces A: Physicochemical and Engineering Aspects 2009;341:110-7.

[339] Graetsch H, Gies H, Topalović I. NMR, XRD and IR study on microcrystalline opals. Physics and Chemistry of Minerals 1994;21:166-75.

[340] Dayanand C, Bhikshamaiah G, Tyagaraju VJ, Salagram M, Murthy AK. Structural investigations of phosphate glasses: a detailed infrared study of the x (PbO)-(1− x) P2O5 vitreous system. Journal of materials science 1996;31:1945-67.

[341] Tortet L, Gavarri J, Nihoul G, Dianoux A. Study of Protonic Mobility in CaHPO< sub> 4</sub>· 2H< sub> 2</sub> O (Brushite) and CaHPO< sub> 4</sub>(Monetite) by Infrared Spectroscopy and Neutron Scattering. Journal of Solid State Chemistry 1997;132:6-16.

[342] Kupser P, Pagel K, Oomens J, Polfer N, Koksch B, Meijer G, et al. Amide-I and-II vibrations of the cyclic β-sheet model peptide gramicidin S in the gas phase. Journal of the American Chemical Society 2010;132:2085-93.

[343] Smith BC. Infrared spectral interpretation: a systematic approach: CRC press; 1999.

[344] Sefcik J, Goddard W. Thermochemistry of silicic acid deprotonation: Comparison of gas-phase and solvated DFT calculations to experiment. Geochimica et cosmochimica acta 2001;65:4435-43.

[345] Li B, Brown KV, Wenke JC, Guelcher SA. Sustained release of vancomycin from polyurethane scaffolds inhibits infection of bone wounds in a rat femoral segmental defect model. J Control Release 2010;145:221-30.

[346] Liechty WB, Kryscio DR, Slaughter BV, Peppas NA. Polymers for Drug Delivery Systems. Annual Review of Chemical and Biomolecular Engineering 2010;1:149-73.

[347] Lan Levengood SK, Polak SJ, Poellmann MJ, Hoelzle DJ, Maki AJ, Clark SG, et al. The effect of BMP-2 on micro- and macroscale osteointegration of biphasic calcium phosphate scaffolds with multiscale porosity. Acta Biomaterialia 2010;6:3283-91.

[348] Kundu B, Lemos A, Soundrapandian C, Sen PS, Datta S, Ferreira JMF, et al. Development of porous HAp and β-TCP scaffolds by starch consolidation with foaming method and drug-chitosan bilayered scaffold based drug delivery system. Journal of Materials Science: Materials in Medicine 2010;21:2955-69.

[349] He Q, Shi J, Chen F, Zhu M, Zhang L. An anticancer drug delivery system based on surfactant-templated mesoporous silica nanoparticles. Biomaterials 2010;31:3335-46.

[350] Ren F, Xin R, Ge X, Leng Y. Characterization and structural analysis of zinc-substituted hydroxyapatites. Acta Biomaterialia 2009;5:3141-9.

[351] Siepmann J, Faisant N, Akiki J, Richard J, Benoit JP. Effect of the size of biodegradable microparticles on drug release: experiment and theory. Journal of Controlled Release 2004;96:123-34.

[352] Wassmer S, Rafat M, Fong WG, Baker AN, Tsilfidis C. Chitosan microparticles for delivery of proteins to the retina. Acta Biomaterialia.

[353] Sousa A, Souza KC, Sousa EMB. Mesoporous silica/apatite nanocomposite: Special synthesis route to control local drug delivery. Acta Biomaterialia 2008;4:671-9.

[354] Gong C, Shi S, Wu L, Gou M, Yin Q, Guo Q, et al. Biodegradable in situ gel-forming controlled drug delivery system based on thermosensitive PCL–PEG–PCL hydrogel. Part 2: Sol–gel–sol transition and drug delivery behavior. Acta Biomaterialia 2009;5:3358-70.

[355] Brandl F, Kastner F, Gschwind RM, Blunk T, Teßmar J, Göpferich A. Hydrogel-based drug delivery systems: Comparison of drug diffusivity and release kinetics. Journal of Controlled Release 2010;142:221-8.

[356] Krishnaiah YSR, Karthikeyan RS, Gouri Sankar V, Satyanarayana V. Three-layer guar gum matrix tablet formulations for oral controlled delivery of highly soluble trimetazidine dihydrochloride. Journal of Controlled Release 2002;81:45-56.

[357] Cosijns A, Vervaet C, Luyten J, Mullens S, Siepmann F, Van Hoorebeke L, et al. Porous hydroxyapatite tablets as carriers for low-dosed drugs. European journal of pharmaceutics and biopharmaceutics : official journal of Arbeitsgemeinschaft fur Pharmazeutische Verfahrenstechnik eV 2007;67:498-506.

[358] Venkataraman S, Hedrick JL, Ong ZY, Yang C, Ee PLR, Hammond PT, et al. The effects of polymeric nanostructure shape on drug delivery. Advanced Drug Delivery Reviews 2011;63:1228-46.

[359] Bhaskar S, Pollock KM, Yoshida M, Lahann J. Towards Designer Microparticles: Simultaneous Control of Anisotropy, Shape, and Size. Small 2010;6:404-11.

[360] Muro S, Garnacho C, Champion JA, Leferovich J, Gajewski C, Schuchman EH, et al. Control of Endothelial Targeting and Intracellular Delivery of Therapeutic Enzymes by Modulating the Size and Shape of ICAM-1-targeted Carriers. Mol Ther 2008;16:1450-8.

[361] Waterman KC, Sutton SC. A computational model for particle size influence on drug absorption during controlled-release colonic delivery. Journal of Controlled Release 2003;86:293-304.

[362] Ishihara S, Matsumoto T, Onoki T, Uddin MH, Sohmura T, Nakahira A. Regulation of the protein-loading capacity of hydroxyapatite by mercaptosuccinic acid modification. Acta Biomaterialia 2010;6:830-5.

[363] Sharma M, Waterhouse GIN, Loader SWC, Garg S, Svirskis D. High surface area polypyrrole scaffolds for tunable drug delivery. International Journal of Pharmaceutics 2013;443:163-8.

[364] El-Ghannam A, Jahed K, Govindaswami M. Resorbable bioactive ceramic for treatment of bone infection. Journal of Biomedical Materials Research Part A 2010;94:308-16.

[365] Lorian V. Antibiotics in laboratory medicine: Lippincott Williams & Wilkins; 2005.

[366] Barna J, Williams D. The structure and mode of action of glycopeptide antibiotics of the vancomycin group. Annual Reviews in Microbiology 1984;38:339-57.

[367] Pearce CM, Williams DH. Complete assignment of the 13C NMR spectrum of vancomycin. Journal of the Chemical Society, Perkin Transactions 2 1995:153-7.

[368] Reynolds JE. Martindale: the extra pharmacopoeia: London, UK; The Pharmaceutical Press; 1982.

[369] Joosten U, Joist A, Gosheger G, Liljenqvist U, Brandt B, von Eiff C. Effectiveness of hydroxyapatite-vancomycin bone cement in the treatment of< i> Staphylococcus aureus</i> induced chronic osteomyelitis. Biomaterials 2005;26:5251-8.

[370] Gautier H, Caillon J, Le Ray A, Daculsi G, Merle C. Influence of isostatic compression on the stability of vancomycin loaded with a calcium phosphate–implantable drug delivery device. Journal of biomedical materials research 2000;52:308-14.

[371] Burger A, Double J, Newell D. Inhibition of telomerase activity by cisplatin in human testicular cancer cells. European Journal of Cancer 1997;33:638-44.

[372] Martin LP, Hamilton TC, Schilder RJ. Platinum resistance: the role of DNA repair pathways. Clinical Cancer Research 2008;14:1291-5.

[373] Takahara PM, Rosenzweig AC, Frederick CA, Lippard SJ. Crystal structure of double-stranded DNA containing the major adduct of the anticancer drug cisplatin. 1995.

[374] Reedijk J. New clues for platinum antitumor chemistry: kinetically controlled metal binding to DNA. Proceedings of the National Academy of Sciences 2003;100:3611-6.

[375] Ekborn A, Laurell G, Johnström P, Wallin I, Eksborg S, Ehrsson H. D-Methionine and cisplatin ototoxicity in the guinea pig: D-methionine influences cisplatin pharmacokinetics. Hearing research 2002;165:53-61.

[376] Decatris M, Sundar S, O'byrne K. Platinum-based chemotherapy in metastatic breast cancer: current status. Cancer treatment reviews 2004;30:53-81.

[377] Dhar S, Gu FX, Langer R, Farokhzad OC, Lippard SJ. Targeted delivery of cisplatin to prostate cancer cells by aptamer functionalized Pt (IV) prodrug-PLGA–PEG nanoparticles. Proceedings of the National Academy of Sciences 2008;105:17356-61.

[378] Nishiyama N, Kato Y, Sugiyama Y, Kataoka K. Cisplatin-loaded polymer-metal complex micelle with time-modulated decaying property as a novel drug delivery system. Pharm Res 2001;18:1035-41.

[379] El-Ghannam A, Ricci K, Malkawi A, Jahed K, Vedantham K, Wyan H, et al. A ceramic-based anticancer drug delivery system to treat breast cancer. Journal of Materials Science: Materials in Medicine 2010;21:2701-10.

[380] Vedantham K, Swet JH, McKillop IH, El-Ghannam A. Evaluation of a bioresorbable drug delivery system for the treatment of hepatocellular carcinoma. J Biomed Mater Res A 2012;100A:432-40.

[381] Dieterich C, Puey A, Lyn S, Swezey R, Furimsky A, Fairchild D, et al. Gene Expression Analysis Reveals New Possible Mechanisms of Vancomycin-Induced Nephrotoxicity and Identifies Gene Markers Candidates. Toxicological Sciences 2009;107:258-69.

[382] Miller FA, Wilkins CH. Infrared spectra and characteristic frequencies of inorganic ions. Analytical Chemistry 1952;24:1253-94.

[383] Ning CQ, Mehta J, El-Ghannam A. Effects of silica on the bioactivity of calcium phosphate composites in vitro. J Mater Sci-Mater M 2005;16:355-60.

[384] Shivanand P, L. Sprockel O. A controlled porosity drug delivery system. International Journal of Pharmaceutics 1998;167:83-96.

[385] Sant S, Nadeau V, Hildgen P. Effect of porosity on the release kinetics of propafenone-loaded PEG-g-PLA nanoparticles. Journal of Controlled Release 2005;107:203-14.

[386] Jalota S, Bhaduri SB, Tas AC. A new rhenanite (β-NaCaPO4) and hydroxyapatite biphasic biomaterial for skeletal repair. Journal of Biomedical Materials Research Part B: Applied Biomaterials 2007;80B:304-16.

[387] Swainson I, Dove M. On the thermal expansion of β-cristobalite. Physics and Chemistry of Minerals 1995;22:61-5.

[388] Vedantham K, Swet JH, McKillop IH, El-Ghannam A. Evaluation of a bioresorbable drug delivery system for the treatment of hepatocellular carcinoma. J Biomed Mater Res A 2011 2012;100A:432-40.

[389] Das G, Nicastri A, Coluccio ML, Gentile F, Candeloro P, Cojoc G, et al. FT-IR, Raman, RRS measurements and DFT calculation for doxorubicin. Microscopy research and technique 2010;73:991-5.

[390] Sturgeon RJ, Schulman SG. Electronic absorption spectra and protolytic equilibria of doxorubicin: direct spectrophotometric determination of microconstants. J Pharm Sci 1977;66:958-61.

[391] Hu F, Neoh K, Kang E. Synthesis and in vitro anti-cancer evaluation of tamoxifen-loaded magnetite/PLLA composite nanoparticles. Biomaterials 2006;27:5725-33.

[392] Cameron KS, Fielding L. NMR diffusion spectroscopy as a measure of host-guest complex association constants and as a probe of complex size. The Journal of organic chemistry 2001;66:6891-5.

[393] Fielding L. NMR methods for the determination of protein-ligand dissociation constants. Current topics in medicinal chemistry 2003;3:39-53.

[394] Barthwal R, Mujeeb A, Srivastava N, Sharma U. A proton nuclear magnetic resonance investigation of the conformation of daunomycin. Chemico-biological interactions 1996;100:125-39.

[395] Barthwal R, Srivastava N, Sharma U, Govil G. A 500 MHz proton NMR study of the conformation of adriamycin. Journal of Molecular Structure 1994;327:201-20.

[396] Wei X, Ming L-J. Comprehensive 2D 1H NMR studies of paramagnetic lanthanide (III) complexes of anthracycline antitumor antibiotics. Inorganic Chemistry 1998;37:2255-62.

[397] Rose B, Simpson I, Loewenstein WR. Calcium ion produces graded changes in permeability of membrane channels in cell junction. 1977.

[398] Yang JD, Roberts LR. Hepatocellular carcinoma: A global view. Nature reviews Gastroenterology & hepatology 2010;7:448-58.

[399] de Lope CR, Tremosini S, Forner A, Reig M, Bruix J. Management of HCC. J Hepatol 2012;56 Suppl 1:S75-87.

[400] Wong R, Frenette C, Gish R. Hepatocellular carcinoma: locoregional and targeted therapies. Gastroenterology clinics of North America 2011;40:599-610.

[401] Kumari A, Yadav SK, Yadav SC. Biodegradable polymeric nanoparticles based drug delivery systems. Colloids and Surfaces B: Biointerfaces 2010;75:1-18.

[402] Roy I, Ohulchanskyy TY, Pudavar HE, Bergey EJ, Oseroff AR, Morgan J, et al. Ceramic-Based Nanoparticles Entrapping Water-Insoluble Photosensitizing Anticancer Drugs: A Novel Drug−Carrier System for Photodynamic Therapy. Journal of the American Chemical Society 2003;125:7860-5.

[403] Paciotti GF, Kingston DGI, Tamarkin L. Colloidal gold nanoparticles: a novel nanoparticle platform for developing multifunctional tumor-targeted drug delivery vectors. Drug Development Research 2006;67:47-54.

[404] O'Neal DP, Hirsch LR, Halas NJ, Payne JD, West JL. Photo-thermal tumor ablation in mice using near infrared-absorbing nanoparticles. Cancer letters 2004;209:171-6.

[405] Wolinsky JB, Colson YL, Grinstaff MW. Local drug delivery strategies for cancer treatment: Gels, nanoparticles, polymeric films, rods, and wafers. Journal of Controlled Release 2012;159:14-26.

[406] Lynch I, Dawson KA, Linse S. Detecting cryptic epitopes created by nanoparticles. Science's STKE: Signal Transduction Knowledge Environment 2006;2006:pe14-pe.

[407] Hussain SM, Hess KL, Gearhart JM, Geiss KT, Schlager JJ. In vitro toxicity of nanoparticles in BRL 3A rat liver cells. Toxicology in Vitro 2005;19:975-83.

[408] Lin W, Huang Y-w, Zhou X-D, Ma Y. In vitro toxicity of silica nanoparticles in human lung cancer cells. Toxicology and applied pharmacology 2006;217:252-9.

[409] Tahara Y, Ishii Y. Apatite cement containing cis -diamminedi chloro platinum implanted in rabbit femur for sustained release of the anticancer drug and bone formation Journal of Orthopaedic Science 2001;6:556-65.

[410] Monasterolo C, Ballestri M, Sotgiu G, Guerrini A, Dambruoso P, Sparnacci K, et al. Sulfonates-PMMA nanoparticles conjugates: A versatile system for multimodal application. Bioorganic & medicinal chemistry 2012.

[411] Gupta G KS, El-Ghannam A. Dissolution kinetics of a Si-rich nanocomposite and its effect on osteoblast gene expression. J Biomed Mater Res A 2007;80:486-96.

[412] Moran DM, Mattocks MA, Cahill PA, Koniaris LG, McKillop IH. Interleukin-6 mediates G(0)/G(1) growth arrest in hepatocellular carcinoma through a STAT 3-dependent pathway. The Journal of surgical research 2008;147:23-33.

[413] Moran DM, Koniaris LG, Jablonski EM, Cahill PA, Halberstadt CR, McKillop IH. Microencapsulation of engineered cells to deliver sustained high circulating levels of interleukin-6 to study hepatocellular carcinoma progression. Cell transplantation 2006;15:785-98.

[414] Brandon-Warner E, Walling TL, Schrum LW, McKillop IH. Chronic ethanol feeding accelerates hepatocellular carcinoma progression in a sex-dependent manner in a mouse model of hepatocarcinogenesis. Alcoholism, clinical and experimental research 2012;36:641-53.

[415] El-Ghannam A, Ning C, Mehta J. Cyclosilicate nanocomposite: A novel resorbable bioactive tissue engineering scaffold for BMP and bone-marrow cell delivery. Journal of Biomedical Materials Research Part A 2004;71:377-90.

[416] Yan X, Gemeinhart RA. Cisplatin delivery from poly (acrylic acid-< i> co</i>-methyl methacrylate) microparticles. Journal of controlled release 2005;106:198-208.

[417] Sitarz M, Handke M, Mozgawa W. Identification of silicooxygen rings in SiO< sub> 2</sub> based on IR spectra. Spectrochimica Acta Part A: Molecular and Biomolecular Spectroscopy 2000;56:1819-23.

[418] Wysokiński R, Hernik K, Szostak R, Michalska D. Electronic structure and vibrational spectra of< i> cis</i>-diammine (orotato) platinum (II), a potential cisplatin analogue: DFT and experimental study. Chemical physics 2007;333:37-48.

[419] Salter CJ, Mitchell RC, Drake AF. Infrared spectroscopic studies of vancomycin and its interactions with N-acetyl-D-Ala-D-Ala and N, N′-diacetyl-L-Lys-D-Ala-D-Ala. J Chem Soc, Perkin Trans 2 1995:2203-11.

[420] Fanizzi FP, Intini FP, Maresca L, Natile G, Uccello-Barretta G. Solvolysis of platinum complexes with substituted ethylenediamines in dimethyl sulfoxide. Inorganic Chemistry 1990;29:29-33.

[421] Wallin M, Grönbeck H, Lloyd Spetz A, Skoglundh M. Vibrational study of ammonia adsorption on Pt/SiO2. Applied Surface Science 2004;235:487-500.

[422] Horcajada P, Rámila A, Férey G, Vallet-Regí M. Influence of superficial organic modification of MCM-41 matrices on drug delivery rate. Solid State Sciences 2006;8:1243-9.

[423] Hans ML, Lowman AM. Biodegradable nanoparticles for drug delivery and targeting. Current Opinion in Solid State and Materials Science 2002;6:319-27.

[424] Weigert A, Jennewein C, Brüne B. The liaison between apoptotic cells and macrophages–the end programs the beginning. Biological chemistry 2009;390:379-90.

[425] Cai S, Xie Y, Bagby TR, Cohen MS, Forrest ML. Intralymphatic Chemotherapy Using a Hyaluronan–Cisplatin Conjugate. Journal of Surgical Research 2008;147:247-52.

[426] Cohen MS, Cai S, Xie Y, Forrest ML. A novel intralymphatic nanocarrier delivery system for cisplatin therapy in breast cancer with improved tumor efficacy and lower systemic toxicity in vivo. The American Journal of Surgery 2009;198:781-6.